

# Valence QCD: Connecting QCD to the Quark Model

K.F. Liu<sup>a</sup>, S.J. Dong<sup>a</sup>, T. Draper<sup>a</sup>, D. Leinweber<sup>b</sup>, J. Sloan<sup>a</sup>, W. Wilcox<sup>c</sup>,  
and R. M. Woloshyn<sup>d</sup>

<sup>a</sup> *Dept. of Physics and Astronomy, Univ. of Kentucky, Lexington, KY 40506*

<sup>b</sup> *Special Research Centre for the Subatomic Structure of Matter and Department of Physics and Mathematical Physics, University of Adelaide, Australia 5005*

<sup>c</sup> *Dept. of Physics, Baylor Univ., Waco, TX 76798*

<sup>d</sup> *TRIUMF, 4004 Wesbrook Mall, Vancouver, B. C., Canada V6T 2A3*

## Abstract

A valence QCD theory is developed to study the valence quark properties of hadrons. To keep only the valence degrees of freedom, the pair creation through the Z graphs is deleted in the connected insertions; whereas, the sea quarks are eliminated in the disconnected insertions. This is achieved with a new “valence QCD” lagrangian where the action in the time direction is modified so that the particle and antiparticle decouple. It is shown in this valence version of QCD that the ratios of isovector to isoscalar matrix elements (e.g.  $F_A/D_A$  and  $F_S/D_S$  ratios) in the nucleon reproduce the  $SU(6)$  quark model predictions in a lattice QCD calculation. We also consider how the hadron masses are affected on the lattice and discover new insights into the origin of dynamical mass generation. It is found that, within statistical errors, the nucleon and the  $\Delta$  become degenerate for the quark masses we have studied (ranging from one to four times the strange mass). The  $\pi$  and  $\rho$  become nearly degenerate in this range. It is shown that valence QCD has the C, P, T symmetries. The lattice version is reflection positive. It also has the vector and axial symmetries, the latter leads to a modified partially conserved axial Ward identity. As a result, the theory has a  $U(2N_F)$  symmetry in the particle-antiparticle space. Through lattice simulation, it appears that this is dynamically broken down to  $U_q(N_F) \times U_{\bar{q}}(N_F)$ . Furthermore, the lattice simulation reveals spin degeneracy in the hadron masses and various matrix elements. This leads to an approximate  $U_q(2N_F) \times U_{\bar{q}}(2N_F)$  symmetry which is the basis for the valence quark model. In addition, we find that the masses of N,  $\Delta$ ,  $\rho$ ,  $\pi$ ,  $a_1$ , and  $a_0$  all drop precipitously compared to their counterparts in the quenched QCD calculation. This is interpreted as due to the disappearance of the ‘constituent’ quark mass

which is dynamically generated through tadpole diagrams. The origin of the hyper-fine splitting in the baryon is largely attributed to the Goldstone boson exchanges between the quarks. Both of these are the consequences of lacking chiral symmetry in valence QCD. We discuss its implication on the models of hadrons.

PACS numbers: 12.38.Gc, 11.15.Ha, 12.40.Aa, 11.30.Rd

# 1 Introduction

In addition to its classification scheme, the quark model is, by and large, quite successful in delineating the spectrum, structure, and decays of mesons and baryons. One often wonders what the nature of the approximation is, especially in view of the advent of quantum chromodynamics (QCD) which is believed to be, after all, the fundamental theory of the quarks and gluons. In order to address this question, we need to understand first where the quark model is successful and where it fails.

To begin with, we need to define what we mean by the quark model. We consider the simplest approach which includes the following ingredients:

- The Fock space is restricted to the valence quarks only, i.e. 3 quarks for the baryon and a quark-antiquark pair for the meson. Although there are variations by including quark self-energy and so on which go beyond the instantaneous interaction and will invoke higher Fock space (e.g.  $q^4\bar{q}$  for the baryon and  $q^2\bar{q}^2$  for the meson), we will not consider them here.
- These valence quarks, be they the dressed constituent quarks or the bare quarks, are confined in a potential or a bag. To this zeroth order, the hadron wave functions involving  $u, d,$  and  $s$  quarks and anti-quarks are classified by the flavor-spin and spatial coordinates according to the  $SU_q(6) \times SU_{\bar{q}}(6) \times O(3)$  group (for brevity, we shall refer it as  $SU(6)$ ). The wave functions are totally antisymmetric in the color space for the baryons and symmetric in the color-anticolor combinations for the meson. For example, the S- and D-wave baryons are described by the 56-plets and the P-wave baryons by the 70-plets. Similarly, the S- and P-wave mesons are described by the 36-plets [1].
- The  $SU(6)$  symmetry is broken down to  $SU(3) \times SU(2)$  by the residual interaction between the quarks which is weak compared to the confining potential. The degeneracies within the multiplets are lifted by these residual interactions. Of course, additional breakings of flavor  $SU(3)$  due to the quark masses are responsible for the detailed splitting within the octet/decuplet baryon multiplets and the meson nonets.

There are many different versions of the quark model which share these attributes. They have been called naive quark model, non-relativistic quark model, constituent quark model, bag model, etc. in the literature. Here we shall refer them generically as the **Valence Quark Model** with the defining features of the lowest Fock space (or valence Fock space) and the  $SU(6)$  flavor-spin symmetry, albeit approximate, as their common denominator. In this work, we shall concentrate our discussion on the light quark systems where the valence quark picture is less well understood. For mesons with heavy quarks, such as the charmoniums and upsilons, the valence picture

based on the non-relativistic potential model which fits experiments reasonably well is confirmed by the non-relativistic lattice QCD calculations [2, 3, 4, 5]. We shall not address them in this study.

Given the definition of the valence quark model, it is easier to understand where it succeeds as well as where it fails. For example, with the one-gluon like exchange potential [6] as the residual interaction between the non-relativistically confined quarks to describe the hyper-fine and fine splittings of the hadron masses, the valence quark model is very successful in fitting meson and baryon masses [7, 8, 9, 10] and baryon magnetic moments [6, 11, 12]. It is also successful in delineating the pattern of electro-magnetic [1, 13, 14], semileptonic and nonleptonic weak decays [15], and the Okubo-Zweig-Iizuka (OZI) rule [16], etc. Similarly it is true for the MIT bag model where the relativistic quarks and anti-quarks are confined in a bag with one-gluon exchange interaction [17, 18].

It is worthwhile noting that all these are based on the valence quark picture aided with  $SU(6) \times O(3)$  group for its flavor-spin and space group. On the other hand, there are notable failures. For example, it fails to account for the  $U(1)$  anomaly (the  $\eta'$  mass), the proton spin crisis and the  $\pi N\sigma$  term. All these problems are associated with large contributions from disconnected insertions involving sea-quarks [19, 20, 21]. These are places where the OZI rule fails badly. Consequently, it is natural not to expect the valence quark model to work in these cases.

There are also other places where the valence quark model does not work well. They include hadron scatterings, couplings, and form factors which are well described by models utilizing the chiral symmetry inherent in QCD. Examples of successful approaches based on chiral symmetry include  $\pi\pi$  scattering [22, 23], vector dominance [24], KSRF relation [25], low-energy  $\pi N$  scatterings [22, 26],  $\pi N$  scattering up to about 1 GeV with the skyrmion [28], nucleon static properties [27], electro-magnetic [27] form factors,  $\pi NN$  form factor [29], NN interaction, and Goldberger-Treiman relation [30]. All these have been worked out quite successfully by the parallel developments which explore the chiral symmetry of QCD. These include the  $\sigma$  model, current algebra, PCAC, chiral perturbation theory, and the more recent developments incorporating large  $N_c$  QCD [31, 32], such as the skyrmion [27, 33] and the contracted current algebra [34].

The common theme of these models is chiral symmetry which involves meson cloud in the baryon and thus, the higher Fock space beyond the valence. This cloud degree of freedom is essential in the case of vector dominance of EM form factors, the pion cloud for the Goldberger-Treiman relation, and the non-vanishing neutron electric form factor. Therefore, it is a challenge to understand why the valence quark model ‘works’ without spontaneously broken chiral symmetry, and where the hyper-fine splitting in hadron spectroscopy and the constituent quark mass come from.

From the above discussion, it is clear that the Fock space beyond the valence is

important and we mentioned two degrees of freedom, namely cloud and sea. How to relate these degrees of freedom back to QCD unambiguously, how to find out their roles in physical quantities, and, more importantly, how to relate them to chiral symmetry are the main subjects of this paper. It turns out that chiral symmetry plays essential roles in light hadron spectroscopy as well as hadron structure. We find that both the ‘constituent’ quark mass and the hyper-fine splitting in light baryons are more of a consequence of spontaneous chiral symmetry breaking than that of gluons and sea quarks.

In Sec. 2, we will define these dynamical degrees of freedom in the Euclidean path integral formalism for the hadronic tensor in deep inelastic scattering. In Sec. 3, we will demonstrate the effects of these degrees of freedom in hadron structure. In Sec. 4, we introduce a valence QCD theory which modifies QCD to suppress quark-antiquark pair production. We will also explore the discrete and continuous symmetries of valence QCD in Sec. 4. In Sec. 5, we adopt a lattice action for valence QCD and prove its reflection positivity and hermiticity. The pion mass, the pion decay constant, and the current quark mass from the axial Ward identity are used to define the zero quark mass limit on the lattice. In Sec. 6, we calculate various ratios of matrix elements to check the  $SU(6)$  relations. The nucleon form factors are calculated and presented in Sec. 7. We then study hadron spectroscopy in comparison with that of QCD to explore the origin of the hyper-fine splitting and the ‘constituent’ quark mass in Sec. 8. Perhaps the most exciting aspect of valence QCD is a new understanding of the origin of dynamical mass generation, something missing in the valence quark model and put in by hand via a constituent quark mass. In Sec. 9, we compare the symmetry breaking patterns in valence QCD and QCD. Finally, in Sec. 10, we summarize the lessons learned from the valence QCD and draw an analogy between the valence quark model and the nuclear shell model. We will also discuss the implication on model building for hadrons.

## 2 Quark Dynamical Degrees of Freedom

We have so far alluded to the meson clouds and sea quarks in addition to the valence quarks. They appear in various QCD-inspired hadronic models and effective theories. How does one define the valence, the cloud, and the sea quarks unambiguously and in a model independent way in QCD? It turns out that the best way of revealing these dynamical degrees of freedom is in deep inelastic scattering where the quarks show up as the parton densities.

The deep inelastic scattering of a muon on a nucleon involves the hadronic tensor which, being an inclusive reaction, involves all intermediate states

$$W_{\mu\nu}(q^2, \nu) = \frac{1}{2M_N} \sum_n (2\pi)^3 \delta^4(p_n - p - q) \langle N | J_\mu(0) | n \rangle \langle n | J_\nu(0) | N \rangle_{spin\ ave.} \quad (1)$$

Since deep inelastic scattering measures the absorptive part of the Compton scattering, it is the imaginary part of the forward amplitude and can be expressed as the current-current correlation function in the nucleon, i.e.

$$W_{\mu\nu}(q^2, \nu) = \frac{1}{\pi} \text{Im} T_{\mu\nu}(q^2, \nu) = \frac{1}{2M_N} \langle N | \int \frac{d^4x}{2\pi} e^{iq \cdot x} J_\mu(x) J_\nu(0) | N \rangle_{spin\ ave.} \quad (2)$$

It has been shown [35] that the hadronic tensor  $W_{\mu\nu}(q^2, \nu)$  can be obtained from the Euclidean path-integral formalism where the various quark dynamical degrees of freedom are readily and explicitly revealed. In this case, one considers the ratio of the four-point function  $\langle O_N(t) J_\nu(\vec{x}, t_2) J_\mu(0, t_1) O_N(0) \rangle$  and the two-point function  $\langle O_N(t - (t_2 - t_1)) O_N(0) \rangle$ , where  $O_N(t)$  is an interpolation field for the nucleon with momentum  $p$  at Euclidean time  $t$ . For example,  $O_N(t)$  can be taken to be the 3 quark fields with nucleon quantum numbers,

$$O_N = \int d^3x e^{i\vec{p} \cdot \vec{x}} \varepsilon^{abc} \Psi^{(u)a}(x) ((\Psi^{(u)b}(x))^T C \gamma_5 \Psi^{(d)c}(x)), \quad (3)$$

for the proton.

As both  $t - t_2 \gg 1/\Delta M_N$  and  $t_1 \gg 1/\Delta M_N$ , where  $\Delta M_N$  is the mass gap between the nucleon and the next excitation (i.e. the threshold of a nucleon and a pion in the  $p$ -wave), the intermediate state contributions will be dominated by the nucleon with the Euclidean propagator  $e^{-M_N(t - (t_2 - t_1))}$ . Hence,

$$\begin{aligned} \widetilde{W}_{\mu\nu}(\vec{q}^2, \tau) &= \frac{\frac{1}{2M_N} \langle O(t) \int \frac{d^3x}{2\pi} e^{-i\vec{q} \cdot \vec{x}} J_\mu(\vec{x}, t_2) J_\nu(0, t_1) O(0) \rangle}{\langle O(t - \tau) O(0) \rangle} \Bigg|_{\substack{t - t_2 \gg 1/\Delta M_N \\ t_1 \gg 1/\Delta M_N}} \\ &= \frac{\frac{f^2}{2M_N} e^{-M_N(t - t_2)} \langle N | \int \frac{d^3x}{2\pi} e^{-i\vec{q} \cdot \vec{x}} J_\mu(\vec{x}, t_2) J_\nu(0, t_1) | N \rangle e^{-M_N t_1}}{f^2 e^{-M_N(t - \tau)}} \\ &= \frac{1}{2M_N V} \langle N | \int \frac{d^3x}{2\pi} e^{-i\vec{q} \cdot \vec{x}} J_\mu(\vec{x}, t_2) J_\nu(0, t_1) | N \rangle, \end{aligned} \quad (4)$$

where  $\tau = t_2 - t_1$ ,  $f$  is the transition matrix element  $\langle 0 | O_N | N \rangle$ , and  $V$  is the 3-volume. Inserting intermediate states,  $\widetilde{W}_{\mu\nu}(\vec{q}^2, \tau)$  becomes

$$\widetilde{W}_{\mu\nu}(\vec{q}^2, \tau) = \frac{1}{2M_N V} \sum_n (2\pi)^2 \delta^3(p_n - p + q) \langle N | J_\mu(0) | n \rangle \langle n | J_\nu(0) | N \rangle_{spin\ ave.} e^{-(E_n - E_N)\tau}. \quad (5)$$

We see from Eq. (5) that the time dependence is in the exponential factor  $e^{-(E_n - E_N)\tau}$ . To go back to the delta function  $\delta(E_n - E_N + \nu)$  in Eq. (1), one needs to carry out the inverse Laplace transform [36, 35]

$$W_{\mu\nu}(q^2, \nu) = \frac{V}{i} \int_{c-i\infty}^{c+i\infty} d\tau e^{\nu\tau} \widetilde{W}_{\mu\nu}(\vec{q}^2, \tau). \quad (6)$$

This is basically doing the anti-Wick rotation back to the Minkowski space.

In the Euclidean path-integral formulation of  $\widetilde{W}_{\mu\nu}(\vec{q}^2, \tau)$ , contributions to the four-point function can be classified according to different topologies of the quark paths between the source and the sink of the proton. They represent different ways the fields in the currents  $J_\mu$  and  $J_\nu$  contract with those in the nucleon interpolation operator  $O_N$ . This is so because the quark action and the electromagnetic currents are both bilinear in quark fields, i.e. of the form  $\bar{\Psi}M\Psi$ , so that the quark number is conserved and as a result the quark line does not branch the way a gluon line does. Fig. 1(a) and 1(b) represent connected insertions (C.I.) of the currents. Here the quark fields from the interpolators  $O_N$  contract with the currents such that the quark lines flow continuously from  $t = 0$  to  $t = t$ . Fig. 1(c), on the other hand, represents a disconnected insertion (D.I.) where the quark fields from  $J_\mu$  and  $J_\nu$  self-contract and are hence disconnected from the quark paths between the proton source and sink. Here, “disconnected” refers only to the quark lines. Of course, quarks surf in the background of the gauge field and all quark paths are ultimately connected through the gluon lines.

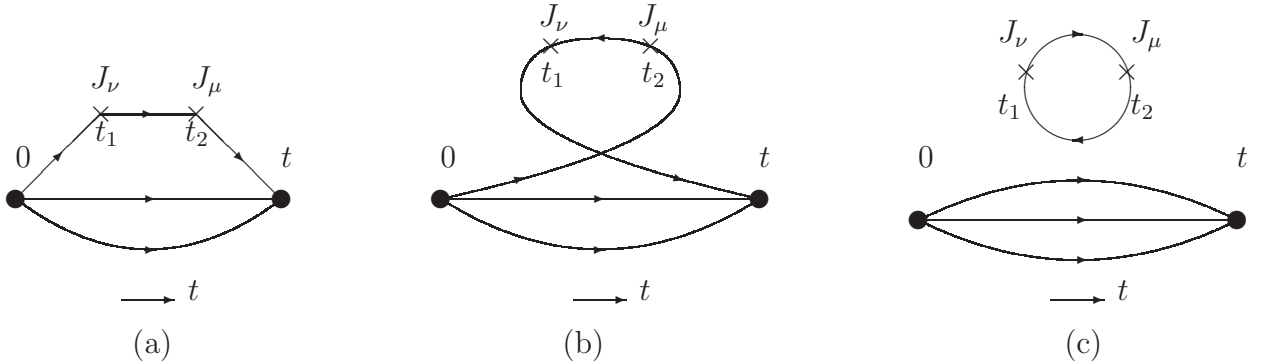


Figure 1: Quark skeleton diagrams in Euclidean path integral formalism for evaluating  $W_{\mu\nu}$  from the four-point function defined in Eq. (4). These represent the lowest twist contributions to  $W_{\mu\nu}$ . (a) and (b) are the connected insertions and (c) is the disconnected insertion.

The infinitely many possible gluon lines and additional quark loops are implicitly there in Fig. 1 but are not explicitly drawn. Fig. 1 represents the contributions of the class of “handbag” diagrams where the two currents are hooked on the same quark line. These are leading twist contributions in deep inelastic scattering.

The other contractions involving the two currents hooking onto different quark lines are represented in Fig. 2. Given a renormalization scale, these are higher twist contributions in the Bjorken limit. Although details of the operator product expansion will be given elsewhere [37], it is easy to see why these contributions in Fig. 2 are suppressed in deep inelastic scattering. Since the hadronic tensor  $W_{\mu\nu}(q^2, \nu)$  in Eq. (2) is the current-current correlation for the forward matrix element, the large momentum that is injected through the current at  $t_1$  must be carried out by the current at  $t_2$  to avoid flowing to the nucleon sink at  $t$ . In the case of Fig. 1, the momentum will simply be conducted through the quark propagators between the currents. However, in Fig. 2, no connected quark propagators exist between the current. Thus, the momentum has to be exchanged through the gluon propagator, leading to the  $O(1/Q^2)$  and  $O(\alpha_s)$  suppression. This is the reason the parton density interpretation is valid for DIS which involves diagonal quark propagators, since the cross terms from the quark Fock space wave functions are suppressed. From now on, we will neglect these “cat’s ears” diagrams in Fig. 2.

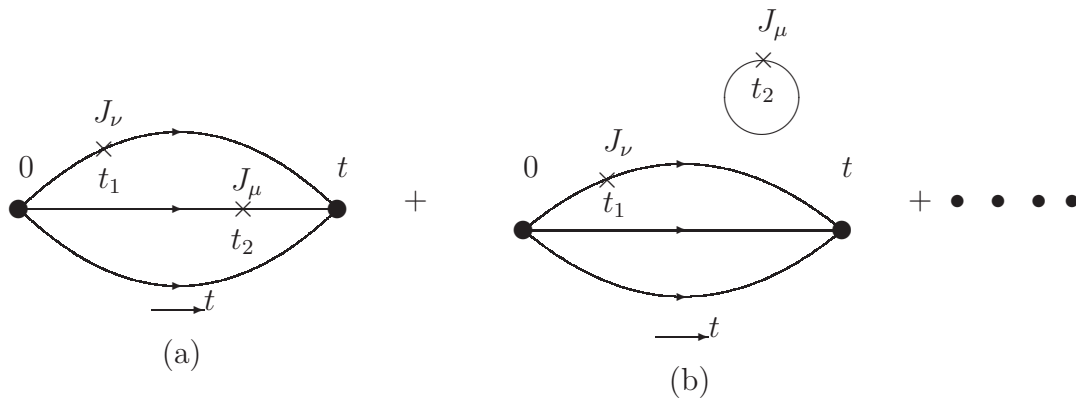


Figure 2: Quark skeleton diagrams similar to those in Fig. 1, except that the two current insertions are on different quark lines. These correspond to higher twist contributions to  $W_{\mu\nu}$  and are suppressed by  $1/Q^2$ .

In the deep inelastic limit where  $x^2 \leq O(1/Q^2)$  (we are using the Minkowski notation here), the leading light-cone singularity of the current product (or commutator)



gives rise to a free quark propagator between the currents. In the time-ordered diagrams in Fig.1, Fig. 1(a)/1(b) involves only a quark/antiquark propagator between the currents; whereas, Fig. 1(c) has both quark and antiquark propagators. Hence, there are two distinct classes of diagrams where the antiquarks contribute. One comes from the D.I. ; the other comes from the C.I.. It is frequently assumed that connected insertions involve only “valence” quarks which are responsible for the baryon number. This is not true. To define the quark distribution functions more precisely, we shall call the antiquark distribution from the D.I. (which are connected to the “valence” quark propagators and other quark loops through gluons) the “sea” quark. We shall refer to the antiquark in the backward time going quark propagator between  $t_1$  and  $t_2$  in Fig. 1(b) as the “cloud” antiquark. On the other hand, the quark in the time forward propagator between  $t_2$  and  $t_1$  in Fig. 1(a) includes both the valence and the cloud quarks. This is because a quark propagator from  $t = 0$  to  $t = t(t > 0)$  involves both the time forward and backward zigzag motions so that one cannot tell if the quark propagator between  $t_2$  and  $t_1$  is due to the valence or the cloud. All one knows is that it is a quark propagator. In other words, one needs to consider cloud quarks in addition to the valence to account for the production of cloud quark-antiquark pairs in a connected fashion (Fig. 1(a)); whereas, the pair production in a disconnected fashion is in Fig. 1(c).

One important point to raise at this stage is that this separation into valence, anti-cloud and sea is gauge invariant (i.e. in the path-integral formalism of Eq. (5), no gauge fixing is required) and topologically distinct as far as the quark skeleton diagrams in Fig. 1 are concerned. However, the separation depends on the frame of the nucleon. It is expected that the parton model acquires its natural interpretation in the large momentum frame of the nucleon, i.e.  $p \geq q$ . Consequently, in the large momentum frame, the parton density for the  $u$  and  $d$  antiquarks come from two sources.

$$\bar{q}(x) = \bar{q}_c(x) + \bar{q}_s(x), \quad (7)$$

where  $\bar{q}_c(x)$  is the cloud antiparton distribution from the C. I. in Fig. 1(b) and  $\bar{q}_s(x)$  denotes the sea antiparton distribution from the D. I. in Fig. 1(c). The strange and charm quarks would only contribute in the D. I. in Fig. 1(c). Similarly, the  $u$  and  $d$  quarks have 2 sources, i.e.

$$q(x) = q_{V+c}(x) + q_s(x), \quad (8)$$

where  $q_{V+c}(x)$  denoting the valence and cloud quarks and  $q_s(x)$  denoting the sea quark are from Fig. 1(a) and Fig. 1(c) respectively. Upon defining  $q_c(x) = \bar{q}_c(x)$  (note the subscript “c” denotes the cloud not charm), the valence parton distribution is obtained by

$$q_V(x) = q_{V+c}(x) - \bar{q}_c(x), \quad (9)$$

and is responsible for the baryon number, i.e.  $\int u_V(x)dx = \int [u(x) - \bar{u}(x)]dx = 2$  and  $\int d_V(x)dx = \int [d(x) - \bar{d}(x)] = 1$  for the proton.

It has been shown [35] that the sea partons in Fig. 1(c) cannot give rise to a large Gottfried sum rule violation, i.e.  $\bar{u}_s(x) = \bar{d}_s(x)$ . Whereas, the origin of  $\bar{u}(x) \neq \bar{d}(x)$  can come primarily from the cloud antipartons in Fig. 1(b).

After the dynamical degrees of freedom are established in deep inelastic scattering, we need to address their relevance to the quark model. The quark model is designed to delineate hadron properties in the rest frame or at low energies, such as hadron masses, decay constants, form factors, electroweak transitions, etc. Unlike the hadronic tensor which entails the calculation of 4-point functions as illustrated in Eq. (5), these quantities involve 2-point and 3-point functions. The question is where do the dynamical degrees of freedom reside in the 3-point functions which describe the matrix elements of hadrons? To track the degrees of freedom, we can consider the operator product expansion as an illustration.

Since the momentum transfer  $|\vec{q}|$  and energy transfer  $\nu$  are large in DIS, the product of currents in the forward Compton amplitude  $T_{\mu\nu}(q^2, \nu)$  can be expanded as a series of local operators. The matrix elements of these local quark bilinear operators are then related to the moments of the parton distribution. This is relatively easy to carry out in the path integral formalism since it treats the fermions as Grassmann numbers instead of operators. While the details are not important here and will be given elsewhere [37], all we need to know is that the effect of expanding in terms of  $1/Q^2$  pinches the separation of the two currents (i.e.  $t_1$  and  $t_2$  in Fig. 1) into one space-time point. Thus the topologically distinct contributions to the four-point functions extracted from Fig. 1(a), 1(b), and 1(c) are related to the matrix elements obtainable from the three-point functions in Fig. 3(a), 3(b), and 3(c) respectively. The latter represents matrix elements of the series of the local operators. Notice that for any single matrix element related to the quark bilinear operator  $\bar{\Psi}\Gamma\Psi$ , i.e.  $\langle N|\Gamma|N\rangle$ , Fig. 3(c) which inherits the sea degree of freedom from Fig. 1(c) is still distinct from Fig. 1(a) and 1(b) and continues to be a D. I.. On the other hand, Fig. 1(a) and 1(b) are no longer topologically distinct. In fact, they represent the *same* C. I. for the local operator. Therefore, the valence and cloud degrees of freedom from Figs. 1(a) and 1(b) are lumped together in the C. I. of 3-point functions. They cannot be separated in a single matrix element in contrast to the case for four-point functions.

What we have shown in this section is that for a flavor-singlet current  $\bar{\Psi}\Gamma\Psi$ , the matrix element  $\langle N|\Gamma|N'\rangle$  has both the C. I. (Figs. 3(a) and 3(b) represent the same C. I. in this case) and the D. I. (Fig. 3(c)). While one can study the sea effect directly and separately from the D. I., one cannot separately study the valence and the cloud in the Z-graphs since both are included in the C. I. and Fig. 3(a) and 3(b) are topologically indistinguishable. Similarly one can trace the quark degrees of freedom in decay constants and hadron masses which are obtainable from the two-point functions. The flavor non-singlet hadrons are obtainable from the C. I. depicted in Fig. 4(a).

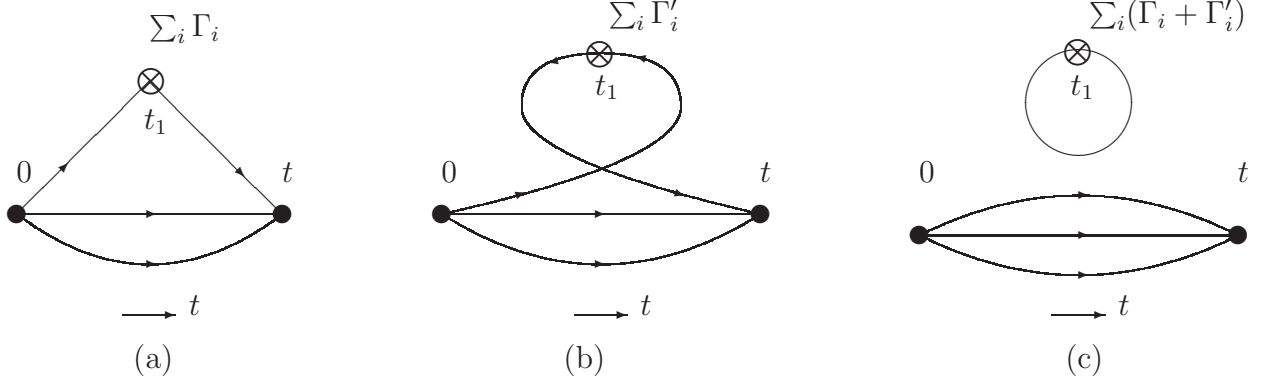


Figure 3: Quark skeleton diagrams in the Euclidean path integral formalism considered in the evaluation of matrix elements for the sum of local operators from the operator product expansion of  $J_\mu(x)J_\nu(0)$ . (a), (b) and (c) corresponds to the operator product expansion from Fig. 1(a), 1(b) and 1(c) respectively.

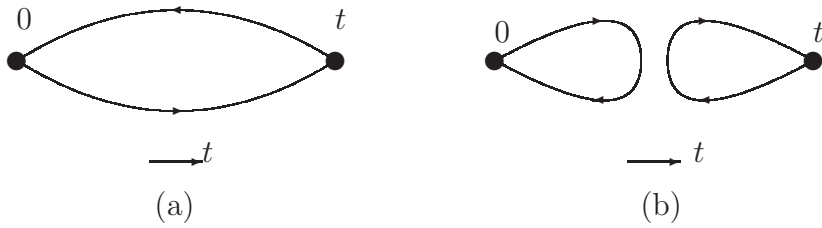


Figure 4: (a) The connected insertion for a meson propagator. (b) The disconnected insertion part for the flavor-singlet meson propagator which involves the annihilation channel.

The flavor-singlet meson, e. g.  $\eta'$ , also involves the D. I. in 4(b). The quark propagators in the two-point functions in Fig. 4(a) and 4(b) include the valence and cloud (Z-graphs) only; they do not involve the sea contribution. The sea effects come only through the fermion determinant in this case.

### 3 Sea and Cloud Quarks in Hadron Structure

Now that we have identified the whereabouts of the quark degrees of freedom, we shall first study the sea effects in hadron structure in order to examine why the valence quark model succeeds and fails in the places we alluded to in the introduction. Since the valence and cloud are tangled together in the C. I., we can only infer the effects of the cloud indirectly.

#### 3.1 Matrix Elements and $SU(6)$ Breaking

##### 3.1.1 Flavor-singlet $g_A^0$ and $F_A$ and $D_A$

Polarized DIS experiments at CERN [38, 40] and SLAC [39] have extracted the flavor-singlet axial coupling constant  $g_A^0$  from the  $g_1$  sum rule, based on the fact that the latter is related to the forward matrix element of the axial current via the operator product expansion [41]. Since the axial current is the canonical spin operator,  $g_A^0$  is thus the quark spin content of the nucleon; i.e.  $g_A^0 = \Delta u + \Delta d + \Delta s$ , where the spin content  $\Delta q$  ( $q = u, d, s$ ) is defined in the forward matrix element of the axial current,  $\langle ps | \bar{q} i \gamma_\mu \gamma_5 q | ps \rangle = 2M_N s_\mu \Delta q$ .

The surprising result the experiments found is a small  $g_A^0$  (0.27(10) [39] and 0.28(16) [40]), much smaller than the expected value of unity from the non-relativistic quark model or 0.75 from the  $SU(6)$  relation (i.e.  $3/5$  of the isovector coupling  $g_A^3 = 1.2574$ ). This has attracted a lot of theoretical attention [42] and the ensuing confusion was dubbed the “proton spin crisis”.

Direct lattice calculations of  $g_A^0$  from the forward matrix element of the flavor-singlet axial current has been carried out [20, 50]. The details of these calculations have been given elsewhere [20, 50]. We shall concentrate on the results here. One word of caution though is that the present calculations are still in the framework of the quenched approximation and the systematic errors due to finite volume and finite lattice size have not been properly assessed. Nevertheless, the smallness of  $g_A^0$  is understood from these calculations [20, 50]. As explained in the preceding section,  $g_A^0$  is composed of two components, i.e.  $g_A^0 = g_A^0(C.I.) + g_A^0(D.I.)$  where  $g_A^0(C.I.)$  is obtained from the connected insertion in Fig. 5(a) and  $g_A^0(D.I.)$  is obtained from the disconnected insertion with the axial current in Fig. 5(b).

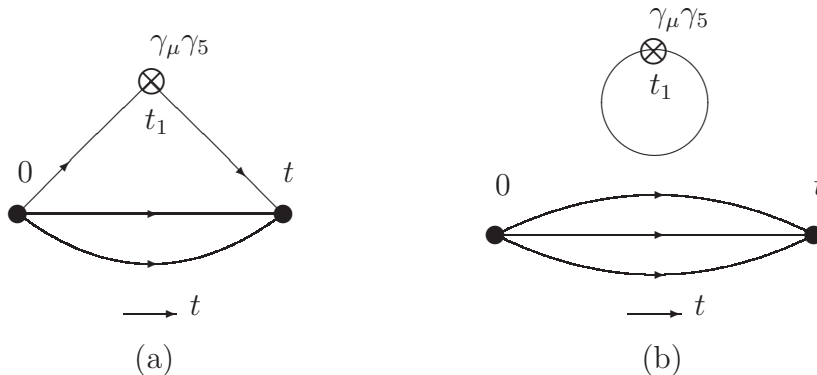


Figure 5: Quark line diagrams of the three-point function in the Euclidean path integral formalism for evaluating  $g_A^0$  from the flavor-singlet axial-vector current. (a) is the connected insertion which contains the valence and cloud degrees of freedom and (b) is the disconnected insertion which contains the quark sea.

Lattice calculation [20] indicates that each of the  $u, d$ , and  $s$  flavors contributes  $-0.12 \pm 0.01$  to the D.I. (Fig. 5(b)). This vacuum polarization from the sea quarks is largely responsible for bringing the value of  $g_A^0$  from  $g_A^0(C.I.) = 0.62(9)$  to  $0.25 \pm 0.12$ , in agreement with the experimental value. This is an example where the sea contributes substantially and leads to a large breaking in the  $SU(6)$  relation. Thus, it is understandable that it should come as a surprise to the valence quark model — the latter does not have the sea degree of freedom and has simply ignored it by assuming the OZI rule. It is interesting to note that although the sea effect is large,  $\Delta u_s, \Delta d_s$ , and  $\Delta s$  from the D. I. are almost identical in the lattice calculation. As a result, the sea effects cancel among different flavors and are not reflected in  $F_A = (\Delta u - \Delta s)/2$ ,  $D_A = (\Delta u - 2\Delta d + \Delta s)/2$ , and the  $F_A/D_A$  ratio. This can be seen from Table 1 where results from the lattice calculations are tabulated and compared with the experiments and the quark model predictions. Since  $\Delta u_s = \Delta d_s = \Delta s$ , the  $F_A$ ,  $D_A$ , and the  $F_A/D_A$  ratio are identical with or without the sea quarks of the D. I.. Partly for this reason, the relativistic quark model prediction based on the input of  $g_A^3 = 1.257$  and the  $SU(6)$ , indicated in the last column of Table 1, are quite reasonable for  $F_A$ ,  $D_A$ , and the  $F_A/D_A$  ratio. It was not until experiments revealed a large negative  $\Delta s$  which leads to a very small  $g_A^0$  that the true shortcomings of the quark model were disclosed.

Table 1: Axial coupling constants and quark spin contents of proton in comparison with experiments, the non-relativistic quark model (NRQM), and the relativistic quark model (RQM).

	C. I.	C. I. + D. I.	Experiments	NRQM	RQM
$g_A^0 = \Delta u + \Delta d + \Delta s$	0.62(9)	0.25(12)	0.28(16) [40], 0.27(10)[39]	1	0.754
$g_A^3 = \Delta u - \Delta d$	1.20(10) [44]	1.20(10)	1.2573(28)	5/3	1.257
$g_A^8 = \Delta u + \Delta d - 2\Delta s$	0.62(9)	0.61(13)	0.579(25) [45]	1	0.754
$\Delta u$	0.91(10)	0.79(11)	0.82(5)[40], 0.82(6)[39]	4/3	1.01
$\Delta d$	-0.29(10)	-0.42(11)	-0.44(5)[40], -0.44(6)[39]	-1/3	-0.251
$\Delta s$		-0.12(1)	-0.10(5)[40], -0.10(4)[39]	0	0
$F_A = (\Delta u - \Delta s)/2$	0.45(6)	0.45(6)	0.459(8) [45]	2/3	0.503
$D_A = (\Delta u - 2\Delta d + \Delta s)/2$	0.75(11)	0.75(11)	0.798(8) [45]	1	0.754
$F_A/D_A$	0.60(2)	0.60(2)	0.575(16) [45]	2/3	2/3

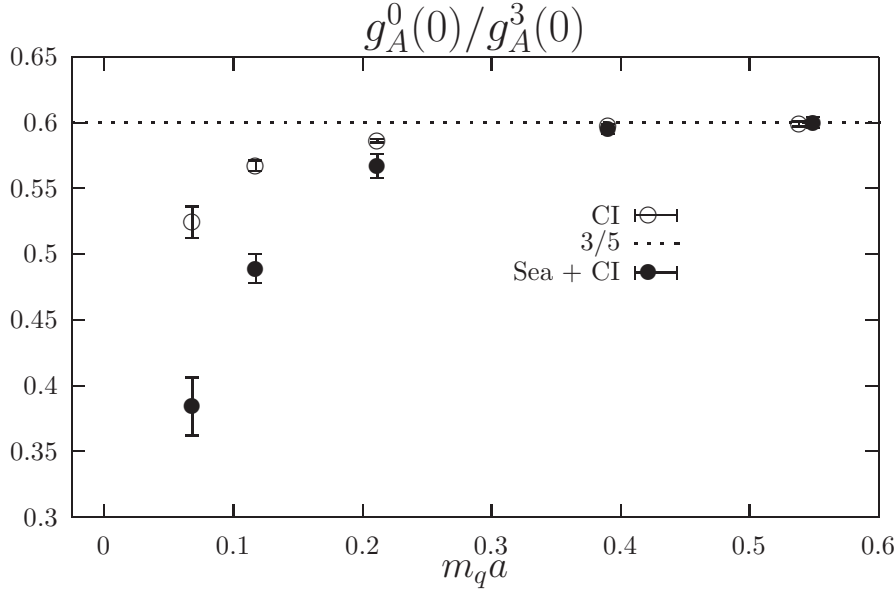


Figure 6: The ratio  $R_A$  in Eq. (10) is plotted against the quark mass. The  $\bullet$  shows the full result with both the C. I. and the D. I. The  $\circ$  indicates the C. I. result only. The solid line is valence quark model prediction of  $3/5$ .

The role of the sea is clear. How about the role of the cloud then? Since its contribution to the C. I. of three-point functions is entangled with the valence, we can not separate it out as is done for the sea. To see its effect indirectly, we consider the ratio

$$R_A = \frac{g_A^0}{g_A^3} = \frac{\Delta u + \Delta d + \Delta s}{\Delta u - \Delta d} = \frac{(\Delta u + \Delta d)(C.I.) + (\Delta u + \Delta d + \Delta s)(D.I.)}{\Delta u - \Delta d} \quad (10)$$

as a function of the quark mass. Our results based on quenched  $16^3 \times 24$  lattices with  $\beta = 6$  for the Wilson  $\kappa$  ranging between 0.154 to 0.105 which correspond to strange and twice the charm masses are plotted in Fig. 6 as a function of the quark mass  $ma = \ln(4\kappa_c/\kappa - 3)$ . The dotted line is the valence quark model prediction of  $3/5$  for both the non-relativistic and relativistic cases. For heavy quarks (i.e.  $\kappa \geq 0.133$  or  $ma \geq 0.4$  in Fig. 6), we see that the ratio  $R_A$  is  $3/5$  irrespective of whether the D. I. is included (shown as  $\bullet$  in Fig. 6) or not (C. I. alone is indicated as  $\circ$ ). This is to be expected because the cloud/sea quarks which are pair produced via the Z-graphs/loops are suppressed for non-relativistic quarks by  $O(p/m_q)$  or  $O(v/c)$ . As for light quarks, the full result (C. I. + D. I.) is much smaller than  $3/5$  largely due to the negatively polarized sea contribution in the D. I. (Table 1 lists the results at the chiral limit). Even for the C. I. alone,  $R_A$  still dips under  $3/5$ . As we shall see later this is caused by the cloud quarks. As we remove these cloud quarks in the Z-graphs by an approximation,  $R_A$  will become much closer to  $3/5$ , the  $SU(6)$  limit.

As a cross check, we note that  $g_A^8$  from the hyperon semi-leptonic decay analysis [45] is 0.579(25) which is many sigmas smaller than the relativistic quark model prediction of 0.754. Since the D. I. of  $g_A^8$  is independent of the sea flavors  $u, d$ , and  $s$ , its sea contribution cancels out. Thus

$$g_A^8 = \Delta u + \Delta d - 2\Delta s = (\Delta u + \Delta d)(C.I.) + (\Delta u + \Delta d - 2\Delta s)(D.I.) \sim g_A^0(C.I.) \quad (11)$$

Indeed, the lattice result shows  $g_A^0(C.I.) = 0.62(9)$  which is consistent with  $g_A^8$ . Therefore, one concludes that the smallness of  $g_A^8$  is related to the cloud quark effect to be unraveled later.

### 3.1.2 $\pi N\sigma$ Term, $\bar{s}s$ in Nucleon and $F_S$ and $D_S$

Another place where the sea plays an even larger role is the  $\pi N\sigma$  term. Like the pion mass in the meson sector, the  $\pi N\sigma$  term is a measure of the explicit chiral symmetry breaking in the baryon sector. There is a long-standing and well-known puzzle surrounding the  $\pi N\sigma$  term

$$\sigma_{\pi N} = \hat{m} \langle N | \bar{u}u + \bar{d}d | N \rangle, \quad (12)$$

where  $\hat{m} = (m_u + m_d)/2$ . The isospin even  $\pi N$  scattering amplitude at the Cheng-Dashen point [46] which equals to  $\sigma_{\pi N}(q^2 = 2m_\pi^2)$  to  $O(m_\pi^4/m_N^4)$  is determined to be

around 60 MeV. On the other hand, if one assumes that  $\langle N|\bar{s}s|N\rangle = 0$ , a reasonable assumption from the OZI rule, the  $\sigma_{\pi N}^{(0)}$  obtained from the octet baryon masses gives only 32 MeV [47], almost a factor two smaller than  $\sigma_{\pi N}(q^2 = 2m_\pi^2)$  extracted from the  $\pi N$  scattering. It has been suggested that the resolution would involve a soft scalar form factor [48] and a large  $\bar{s}s$  content in the nucleon [47, 49] with  $y = 2\langle N|\bar{s}s|N\rangle/\langle N|\bar{u}u + \bar{d}d|N\rangle \sim 0.2 - 0.3$ . Both aspects of the resolution are checked quantitatively in the lattice calculations [21, 50]. It is found that the scalar form factor is indeed very soft in the D. I. [21] which is consistent with a two  $\pi$  intermediate state in the dispersion approach of the chiral perturbation theory [48]. A large  $\bar{s}s$  content in the nucleon is also found [21, 50] so that the conjecture of large ratio  $y$  to resolve the  $\pi N\sigma$  term discrepancy is verified.

A large  $\bar{s}s$  content in the nucleon implies an even larger D. I. for the  $\langle p|\bar{u}u + \bar{d}d|p\rangle$ . We see from Table 2 that the D. I. of  $\langle p|\bar{u}u + \bar{d}d|p\rangle$  is in fact  $\sim 2$  times larger than the C. I. counterpart. Thus, 2/3 of the  $\pi N\sigma$  term comes from the sea (Table 2). This is the largest sea contribution to any physical quantity that we are aware of. As for the quark model,  $\langle p|\bar{u}u + \bar{d}d|p\rangle$  is predicted to be  $\leq 3$ . The reason is the following: the scalar current expanded in the plane-wave basis,

$$\int d^3x \bar{\Psi}\Psi(x) = \int d^3k \frac{m}{E} \sum_s [b^\dagger(\vec{k}, s)b(\vec{k}, s) + d^\dagger(\vec{k}, s)d(\vec{k}, s)], \quad (13)$$

is the sum of the quark and antiquark numbers weighted by the factor  $m/E$ . Since the valence quark model does not contain antiquarks and  $m < E$ , except for the zero modes, the scalar matrix element will be less than the valence quark number. Thus, we see that the quark model underpredicts the  $\pi N\sigma$  term by a factor of 3 or more.

Unlike the case of the axial current matrix element, different flavor contributes differently to the D. I. of the scalar matrix element –  $s$  contributes less than  $u$  and  $d$ . As a result, the  $SU(3)$  antisymmetric and symmetric parameters,

$$\begin{aligned} F_S &= (\langle p|\bar{u}u|p\rangle - \langle N|\bar{s}s|N\rangle)/2 = (\langle p|\bar{u}u|p\rangle)(C.I.) + \langle p|\bar{u}u|p\rangle(D.I.) - \langle N|\bar{s}s|N\rangle/2 \\ D_S &= (\langle p|\bar{u}u|p\rangle)(C.I.) - 2\langle p|\bar{d}d|p\rangle(C.I.)/2 + (\langle N|\bar{s}s|N\rangle - \langle p|\bar{d}d|p\rangle(D.I.))/2 \end{aligned} \quad (14)$$

are strongly affected by the large D. I. part. We see from Table 2 that both  $D_S$  and  $F_S$  compare favorably with the phenomenological values obtained from the  $SU(3)$  breaking pattern of the octet baryon masses with either linear [51, 52] or quadratic mass relations [53]. This agreement is significantly improved from the valence quark model which predicts  $F_S < 1$  and  $D_S = 0$  and also those of the C. I. alone [51, 52]. The latter yields  $F_S = 0.91(13)$  and  $D_S = -0.28(10)$  which are only half of the phenomenological values [51, 52, 53]. This again underscores the importance of the sea-quark contributions.

Next, we address the effect of the cloud quarks in the C. I.. Similar to the ratio



Table 2: Scalar contents,  $\sigma_{\pi N}$ ,  $F_S$ , and  $D_S$  in comparison with phenomenology and quark model (QM). The 17.7 MeV in the last column is determined with the quark mass from the lattice calculation.

	C. I.	C. I + D. I.	Phenomenology	QM
$\langle p \bar{u}u + \bar{d}d p\rangle$	3.02(9)	8.43(24)		$\leq 3$
$\langle p \bar{u}u - \bar{d}d p\rangle$	0.63(9)			$\leq 1$
$\langle N \bar{s}s N\rangle$	1.53(7)			0
$F_S$	0.91(13)	1.51(12)	1.52 [51, 52] — 1.81[53]	$\leq 1$
$D_S$	-0.28(10)	-0.88(28)	-0.52[51, 52] — -0.57[53]	0
$\sigma_{\pi N}$	17.8(5) MeV	49.7(2.6) MeV	45 MeV [48]	$\leq 17.7$ MeV

$R_A$  in the axial-vector case, we plot the ratio

$$R_S = \frac{g_S^{I=0}}{g_S^{I=1}} = \frac{\langle p|\bar{u}u + \bar{d}d|p\rangle}{\langle p|\bar{u}u - \bar{d}d|p\rangle} = \frac{(\langle p|\bar{u}u + \bar{d}d|p\rangle)(C.I.) + (\langle p|\bar{u}u + \bar{d}d|p\rangle)(D.I.)}{\langle p|\bar{u}u - \bar{d}d|p\rangle} \quad (15)$$

as a function of the quark mass in Fig. 7.

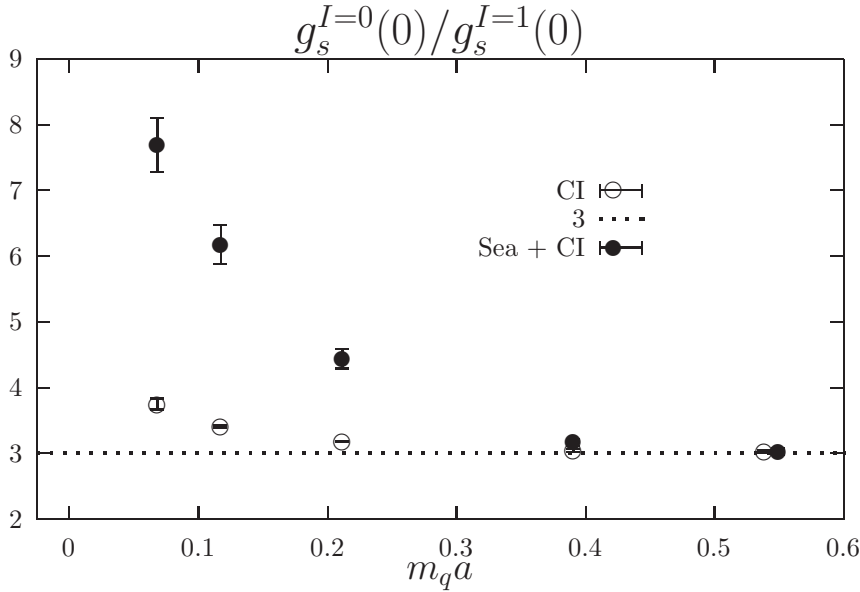


Figure 7: The ratio  $R_S$  in Eq. (15) is plotted against the quark mass. The  $\bullet$  shows the full result with both the C. I. and the D. I. The  $\circ$  indicates the C. I. result only. The solid line is non-relativistic quark model prediction of 3.

The dotted line is the valence quark model prediction of 3 for both the non-relativistic and relativistic cases. Again for heavy quarks (i.e.  $\kappa \geq 0.133$  or  $ma \geq 0.4$  in Fig. 7), we see that the ratio  $R_S$  is 3 irrespective whether the D. I. is included (shown as  $\bullet$  in Fig. 7) or not (C. I. alone is indicated as  $\circ$ ). As for light quarks, the full result (C. I. + D. I.) is much larger than 3 largely due to the large sea contribution in the D. I. (Table 2 lists the results at the chiral limit). Even for the C. I. alone,  $R_S$  still overshoots 3. As we shall see later, this is caused by the cloud quarks. As we remove these cloud quarks in the Z-graphs in an approximation,  $R_S$  will become much closer to 3, the  $SU(6)$  limit.

### 3.1.3 Magnetic Moments of the Nucleon

After having established the importance of the sea and cloud effects in the axial and scalar matrix elements, one should naturally ask what happens to vector current matrix elements, especially the neutron to proton magnetic moment ratio  $\mu_n/\mu_p$ . How much will the sea and cloud affect the ratio and in what way? After all, the  $\mu_n/\mu_p$  ratio was well predicted by the valence picture – a celebrated defining success of the  $SU(6)$  symmetry.

It has been known for some time that a nontrivial sea-quark contribution to baryon magnetic moments is essential to reproducing the experimental moments [54, 55, 56]. It turns out that the individual sea contribution of each flavor is not small [56, 57]. A direct lattice calculation of the strangeness magnetic form factor is  $G_M^s(0) = -0.36 \pm 0.20$  [57] \*. Although the central value of our lattice result differs in sign from that of the SAMPLE experiment which has  $G_M^s(Q^2 = 0.1\text{GeV}^2) = +0.23 \pm 0.37 \pm 0.15 \pm 0.19$  from the elastic parity-violating electron scattering [58], they are consistent within errors. The  $u$  and  $d$  contributions are  $\sim 80\%$  larger,  $G_M^{u,d}(0)(D.I.) = -0.65 \pm 0.30$ . However, their net contribution to the proton and neutron magnetic moment

$$\mu(D.I.) = (2/3G_M^u(0)(D.I.) - 1/3G_M^d(0)(D.I.) - 1/3G_M^s(0))\mu_N = -0.097 \pm 0.037\mu_N \quad (16)$$

becomes smaller due the cancellation of the quark charges of  $u, d$ , and  $s$ . This small  $SU(6)$ -breaking sea quark effect is further nullified by the cloud effect.

This is illustrated in Fig. 8, where the neutron to proton magnetic moment ratio is plotted against the quark mass. We see in Fig. 8 that for heavy quarks in the charm region ( $m_q a$  at 0.55 corresponds to  $m_q \sim 1$  GeV), the ratio from the C. I. is close to the  $SU(6)$  prediction of  $-2/3$ . This is quite reasonable, as this is in the non-relativistic regime where one expects  $SU(6)$  to work well as in the case of  $g_A$  and  $g_S$  in the preceding sections. When the quark mass comes down to the strange region (i.e.  $m_q a = 0.07$ ), the ratio becomes less negative. Extrapolated to the chiral limit, the ratio is  $-0.616 \pm 0.022$  which deviates from the  $SU(6)$  prediction by  $\sim 8\%$ .

---

\*Note this is defined via the vector current  $\bar{s}\gamma_\mu s$  without the electric charge

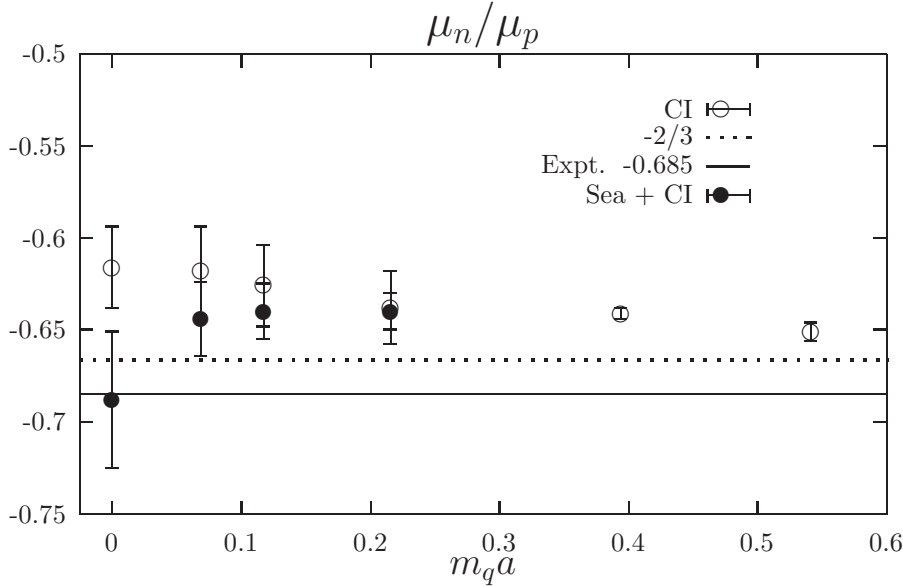


Figure 8: The ratio of the neutron to proton magnetic moment ratio  $\mu_n/\mu_p$  is plotted against the quark mass. The  $\circ$  indicates the C. I. result only and the  $\bullet$  shows the full result with both the C. I. and the D. I. The solid line is valence quark model prediction of  $-2/3$  and the dashed line is the experimental result of  $-0.685$ .

We understand this deviation as mainly due to the cloud quark effect in the Z-graphs; this will be verified later. Now as the sea quark contribution  $\mu(D.I.)$  in Eq. (16) is added to the C. I., we find that it tends to counter the cloud effect and bring the ratio back closer to the  $SU(6)$  prediction. At the chiral limit, the  $\mu_n/\mu_p$  ratio then comes down to  $-0.68 \pm 0.04$  which is quite consistent with the experimental value of  $0.685$ . We should point out that the  $\mu_n/\mu_p$  ratio for the full result ( $\bullet$ ) is more negative at the chiral limit compared with those at other  $m_q a$  has to do with the fact that different extrapolations are used for the C. I. and the D. I.. The C. I. employs the linear quark mass extrapolation, as do other observables for the C. I. [20, 21, 44]; whereas, the D. I. uses the  $\sqrt{m_q}$  dependence for the chiral extrapolation [57] as in the scalar case to reflect the non-analytic behavior in chiral loops [59, 21]. From this analysis, we see that although the individual  $G_M^u(0)(D.I.)$ ,  $G_M^d(0)(D.I.)$ , and  $G_M^s(0)$  are large, their net contribution  $\mu(D.I.)$  in Eq. (16) is much smaller because of the partial cancellation due to the quark charges of u, d, and s. The net sea contribution is further cancelled by the cloud effect to bring the  $\mu_n/\mu_p$  ratio close to the experimental value. Barring any known symmetry principle yet to surface, this cancellation is probably accidental and in stark contrast with the  $\pi N \sigma$  term and flavor-singlet  $g_A^0$  where the cloud and sea effects add up to enhance the  $SU(6)$  breaking [20, 21] as detailed in the preceding sections.

So it seems that the success of the  $SU(6)$  prediction of the neutron to proton

magnetic moment ratio is fortuitous due to these two cancellations and as a result it has not revealed, and may even has helped conceal, the importance of the cloud and sea quark effects over the years.

### 3.2 Form Factors and Meson Dominance

In all the above ratios we considered, i.e.  $R_A, R_S$ , and  $\mu_n/\mu_p$ , the  $SU(6)$  breaking due to the cloud in the Z-graphs is at the level of 10 – 20% which is relatively small compared with, say, the sea quark effect in  $R_S$ . However, its effect is large in the nucleon form factors and has been a subject of wide interest.

It is well known from the  $e^+e^- \rightarrow \pi\pi$  experiment that the process is dominated by the  $\rho$  meson pole. Extending this  $\rho$  meson dominance of the photon coupling to the space-like part of the pion electric form factor  $F_\pi(q^2 < 0)$ , it accounts for 95% of the pion charge radius and is the basis of the ‘vector dominance’ [24]. This is supported by the lattice studies of the pion electric form factor [60, 61, 62]. It is found that the calculated form factor for different quark masses can be well fitted with a monopole form  $1/(1 + q^2/m_\rho^2)$ , with  $m_\rho$  being the lattice  $\rho$  mass for the corresponding quark mass. Similarly, the dipole form of the nucleon electromagnetic and axial form factors is interpreted as the product of two monopoles. For example, the isovector part of the nucleon Dirac form factor can be written as [63]

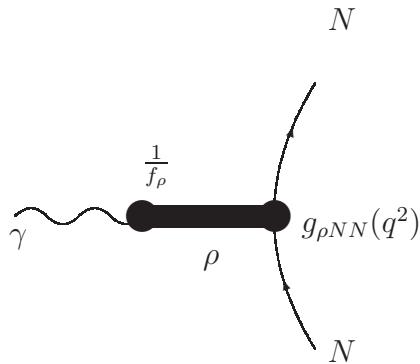


Figure 9: The schematic diagram which depicts the photon coupling to the nucleon goes through the  $\rho$  meson in a vector dominance picture.

$$F_1^V(q^2) = \frac{1}{2}(F_1^p(q^2) - F_1^n(q^2)) = \frac{1}{2} \frac{1}{1 - q^2/m_\rho^2} \frac{g_{\rho NN}(q^2)}{f_\rho} \quad (17)$$

to reflect that the dominating process is the photon coupling to the  $\rho$  meson which in turn couples to the nucleon as shown in Fig. 9.

One monopole in  $F_1^V(q^2)$  is the  $\rho$  meson propagator, and the other one is  $g_{\rho NN}(q^2) = f_\rho \frac{\Lambda^2 - m_\rho^2}{\Lambda^2 - q^2}$  to parametrize the  $\rho NN$  vertex (see Fig. 9). By the same token, the isovector axial form factor with axial meson dominance takes the form

$$g_A^3(q^2) = \frac{g_A^3(0)}{1 - q^2/m_{a_1}^2} g_{a_1 NN}(q^2) \quad (18)$$

where  $g_{a_1 NN}(q^2)$  is the  $a_1 NN$  vertex and can be parametrized with a monopole form. The isovector pseudoscalar form factor should reflect the pion pole for small  $q^2$  and has the form

$$g_P^3(q^2) = \frac{g_P^3(0)}{1 - q^2/m_\pi^2} \frac{g_{\pi NN}(q^2)}{g_{\pi NN}(0)} \quad (19)$$

where  $g_{\pi NN}(q^2)$  is the  $\pi NN$  form factor.

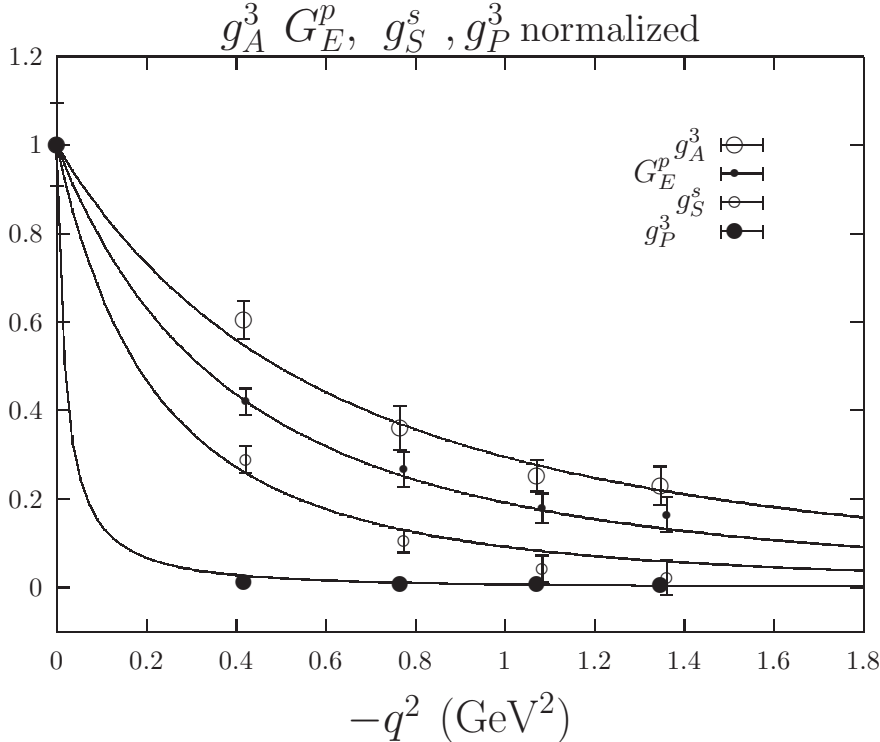


Figure 10: The isovector axial form factor  $g_A^3(q^2)$ , the proton electric form factor  $G_E^p(q^2)$ , the strangeness scalar form factor  $g_S^s(q^2)$ , and the isovector pseudoscalar form factor  $g_P^3(q^2)$  are plotted as a function of  $-q^2$ .

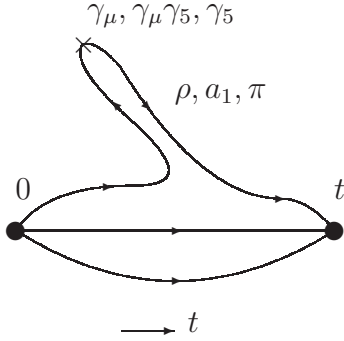


Figure 11: The quark line diagram for the C. I. which illustrates the meson dominance picture with different intermediate meson state corresponding to the respective probing current.

Thus one of the major differences of the various form factors of the nucleon is reflected in the mass of the meson which dominates the matrix element in the t-channel for the specific current. We plot in the following the isovector axial form factor  $g_A^3(q^2)$ , the proton electric form factor  $G_E^p(q^2)$ , the strangeness scalar form factor  $g_S^3(q^2)$  [21], and the isovector pseudoscalar form factor  $g_P^3(q^2)$  [20] in Fig. 10.

We see that, since  $g_A^3(q^2)$  and  $g_P^3(q^2)$  involve only the C. I. and  $G_E^p(q^2)$  is dominated by the C. I. [57], their different behaviors in  $q^2$  reflect the  $\rho, a_1$  and  $\pi$  propagators in the cloud which serve as the intermediate states in the meson dominance picture as depicted in Fig. 11.

Given that experimentally  $m_{a_1} = 1230\text{MeV} > m_\rho = 769\text{MeV} > m_\pi = 140\text{MeV}$  and if one assumes that  $g_{\rho NN}(q^2)$ ,  $g_{a_1 NN}(q^2)$  and  $g_{\pi NN}(q^2)$  have a similar form in  $q^2$ , the fact that  $g_P^3(q^2)$  falls off faster than  $G_E^p(q^2)$  which in turn falls off faster than  $g_A^3(q^2)$  is then to be expected. We should mention in passing that both  $G_E^p(q^2)$  and  $g_A^3(q^2)$  shown in Fig. 10 from the lattice calculation [44, 57] agree with the experiments within  $\sim 6\%$ . This is a clear manifestation of the cloud quark effect through the meson cloud. We can attempt to define the meson-nucleon vertex by dividing the form factors in Eqs. (17), (18), and (19) by their respective meson propagators. These are plotted in Fig. 12. We see that the resulting  $g_{\rho NN}(q^2)$ ,  $g_{a_1 NN}(q^2)$  and  $g_{\pi NN}(q^2)$  extracted this way are much closer to each other than those in Fig. 10. We should mention that the monopole fit of  $g_{\pi NN}(q^2)$  gives  $g_{\pi NN}(0) = 12.2 \pm 2.3$  which checks out the Goldberger-Treiman relation [65].

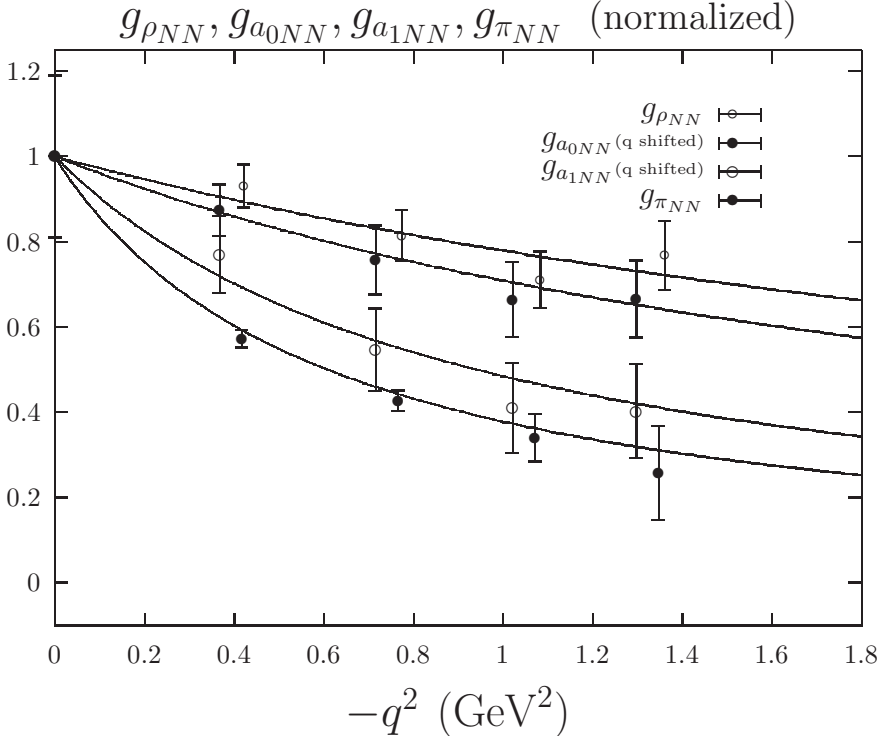


Figure 12: The meson-nucleon-nucleon vertices  $g_{\rho NN}(q^2)$ ,  $g_{a_1 NN}(q^2)$ ,  $g_{\pi NN}(q^2)$ , and  $g_{a_0 NN}(q^2)$  deduced from the EM form factors,  $g_A^3(q^2)$ ,  $g_P^3(q^2)$ , and the isovector scalar form factor  $g_S^3(q^2)$  are plotted as a function of  $-q^2$ .

Also plotted in Fig. 10 is the strangeness scalar form factor  $g_S^s(q^2)$  which is from the D. I. (Fig. 3(c)). It is very soft and has been interpreted as due to the  $K\bar{K}$  intermediate state as depicted in Fig. 13(a) [21]. The D. I. with u or d quarks are even softer [21] and are consistent with the dispersion analysis of  $\pi\pi$  intermediate state in chiral perturbation theory ( $\chi$  PT) [48]. This appears to be the source of the pion and kaon loops in  $\chi$  PT [49] which are responsible for the non-analytic contribution of  $m_q^{3/2}$  or  $m_\pi^3$  and  $m_K^3$  in hadron masses (see Fig. 13(b)).

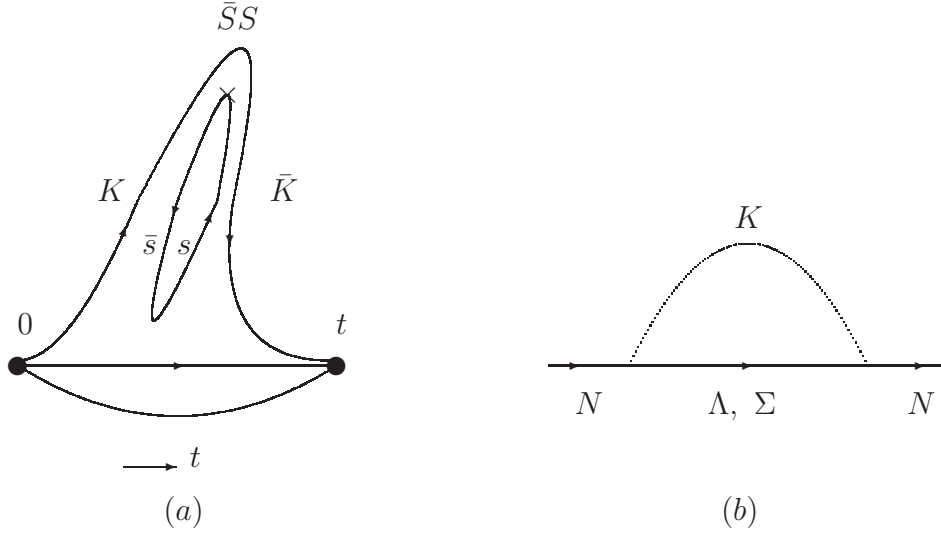


Figure 13: (a) The quark line diagram which illustrates the  $K\bar{K}$  intermediate state which dominates the form factor  $g_S^s(q^2)$ . (b) The kaon loop diagram in chiral perturbation theory.

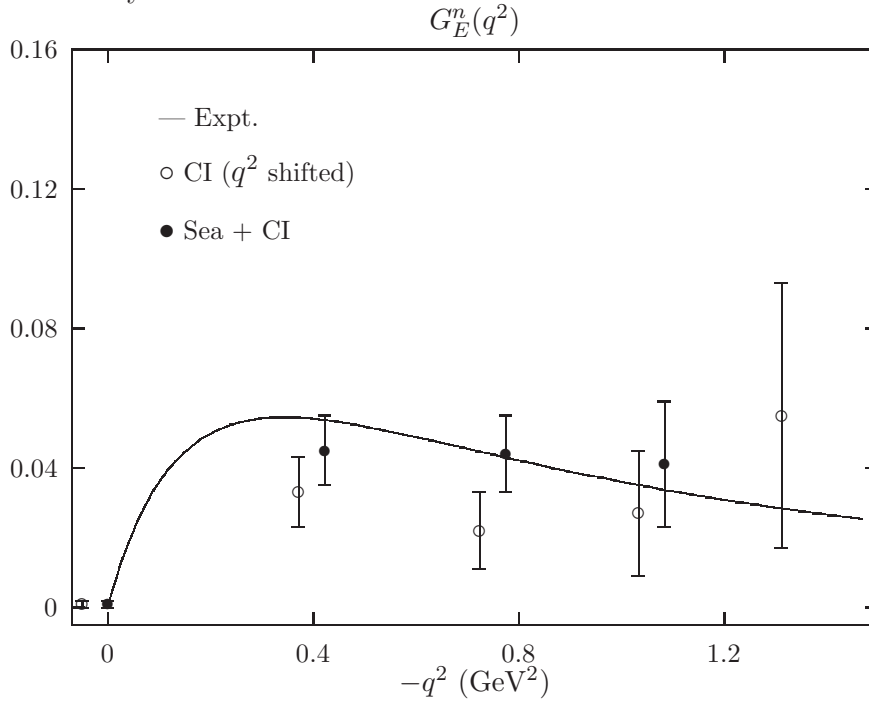


Figure 14: The neutron electric form factor  $G_E^n(q^2)$  together with the fit to the experimental result (solid line). The  $\circ$  indicates the C. I. contribution and the  $\bullet$  shows the full result with both the C. I. and the D. I.



This nonlinear dependence on the quark masses or  $m_\pi^2$  has been observed prominently in hadron masses with dynamical fermions in lattice simulations [80]. This illustrates the sea quark effect in hadron masses and form factors. The neutron charge form factor in the strict  $SU(6)$  quark model would be identically zero, since the positively charged  $u$  quark and the negatively charged  $d$  quarks have the same spatial wave function. Thus, the small positive  $G_E^n(q^2)$  signals the effects of the cloud and the sea without the contamination of the valence part like in other quantities. We present the lattice calculation of  $G_E^n(q^2)$  [57] in Fig. 14 together with the experimental result. It is seen that both the cloud from the C. I. and the sea from the D. I. are positive and their contributions are similar in size.

### 3.2.1 Density and Size of Nucleon

Now, we can look at the time averaged radial density distribution of the nucleon due to different current probes. Define the time averaged density distribution as

$$\rho(r) = N \frac{1}{(2\pi)^2} \int dt d^4q e^{i(\vec{q}\cdot\vec{r} - q_0 t)} F(q^2) = N \frac{1}{(2\pi)^{3/2}} \int d^4q \delta(q_0) e^{i\vec{q}\cdot\vec{r}} F(q^2) \quad (20)$$

where  $N$  is the normalization factor so that  $\int d^3r \rho(r) = 1$ . We plot the pseudoscalar density  $\rho_P(r)$ , the scalar strangeness density  $\rho_S^s(r)$ , the electric charge density  $\rho_c(r)$ , and the axial current density  $\rho_A(r)$  so obtained from  $g_P^3(q^2)$ ,  $g_S^s(q^2)$ ,  $G_E^p(q^2)$ , and  $g_A^3(q^2)$  in Fig. 15.

We see that  $\rho_P(r)$  has the longest range. This is presumable due to the pion cloud which dominates the pseudoscalar channel and has the longest Compton wavelength of all hadrons. The next longest is the scalar strangeness density  $\rho_{S^s}(r)$  which seems to reflect the  $K\bar{K}$  meson intermediate state in Fig. 13(a) which would correspond to the kaon loop in chiral perturbation theory as shown in Fig. 13(b). Then comes the electric charge density in the proton  $\rho_c(r)$  which is well known and has been frequently used to extract the size of the nucleon. Finally, the one with the smallest size is the axial current density  $\rho_A(r)$  which reflects the small Compton wavelength of the  $a_1$  meson.

Now what is the size of the nucleon? As seen from Fig. 15, it is in the eyes of the beholder. In other words, it depends on what probe is used to measure it. It ranges from 3.56(3) fm for the pseudoscalar density, 1.06(9) fm for the strangeness density, 0.797(29) fm for the proton charge density, to 0.627(29) fm for the axial current density, indeed a large variation.

We see that even though the clouds in the C. I. do not break the  $SU(6)$  symmetry as much as the seas in the D. I. for the scalar and axial currents, they afford a large variation in hadron form factors and sizes. Short of these meson clouds, the valence quark model simply is not capable of delineating the richness of the various form factors. A model like the skyrmion, on the other hand, is capable of detailing the

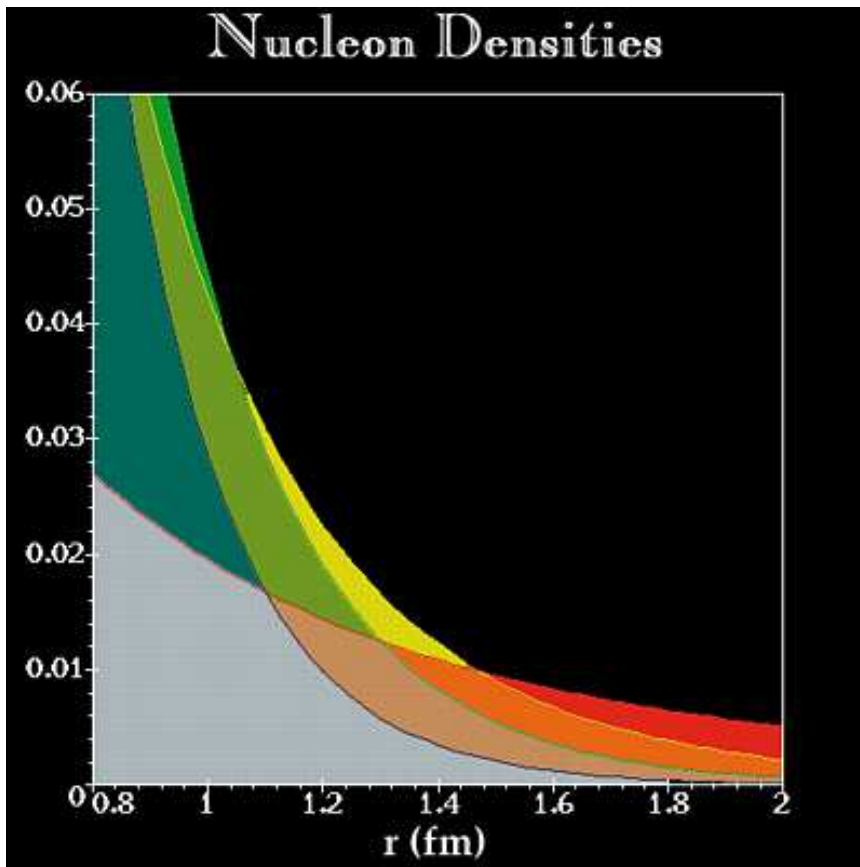


Figure 15: The normalized pseudoscalar density  $\rho_P(r)$  (in red), the scalar strangeness density  $\rho_S^s(r)$  (in yellow), the electric charge density  $\rho_c(r)$  (in green), and the axial current density  $\rho_A(r)$  (in blue) are plotted as a function of the radial distance from the center.

G-T relation [27], the meson dominance of the nucleon form factors [67, 68], negative square charge radius of the neutron [27], etc. All these are achieved via the ingredient of the meson clouds.

## 4 Valence QCD

After having examined the roles of the dynamical quark degree of freedom, we come back to the original question of what approximation to QCD the valence quark model represents. As illustrated in Fig. 5, the sea is only involved in the D. I. part of the three-point function and thus can be isolated as far as its contribution is concerned. On the other hand, we have stressed in Sec. 2 that the cloud and valence contributions are lumped in the C. I. in Fig. 5 and cannot be separated a posteriori. Thus to

single out the valence effects and compare to the valence quark model requires an approximation to QCD. This can be achieved by forcefully eliminating pair creation and annihilation by decoupling the quark from the antiquark. In other words, we want to eliminate all the Z-graphs such as a typical one illustrated in Fig. 16.

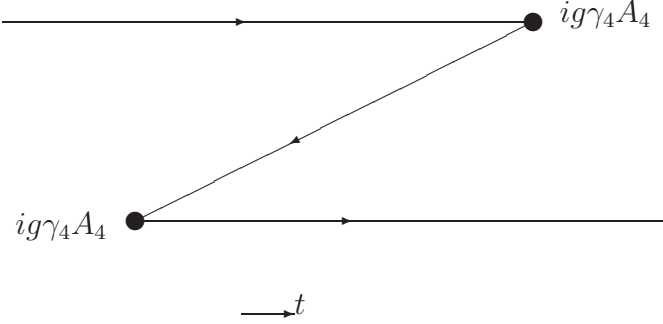


Figure 16: A typical Z-graph as a diagram in the time-ordered perturbation.

We introduce valence QCD (VQCD), a theory which is designed to achieve this goal.

First of all, we shall introduce the particle field  $u$  and the antiparticle field  $v$  in lieu of the Dirac field  $\Psi$  in the valence QCD lagrangian

$$\mathcal{L}_{VQCD} = -\frac{1}{4}F_{\mu\nu}F_{\mu\nu} - \bar{u}\left[\frac{\gamma_4 + 1}{2}D_4 + \vec{\gamma} \cdot \vec{D} + m\right]u - \bar{v}\left[\frac{\gamma_4 - 1}{2}D_4 + \vec{\gamma} \cdot \vec{D} + m\right]v. \quad (21)$$

Comparing with the QCD lagrangian, the valence version has changed the  $\gamma_4$  into  $\frac{\gamma_4 + 1}{2}$  for the particle field  $u$  and  $\frac{\gamma_4 - 1}{2}$  for the antiparticle field  $v$ . We note that the  $u$  and  $v$  fields do not couple. Now we want to prove that the propagator of the  $u$  field only propagates forward in time and does not zig-zag in the time direction to generate particle-antiparticle pairs. The propagator  $S_u(x, y; A)$  satisfies the equation

$$-\left(\frac{\gamma_4 + 1}{2}D_4 + \vec{\gamma} \cdot \vec{D} + m\right)S_u(x, y; A) = \delta(x - y). \quad (22)$$

This can be cast in the integral representation with the static propagator  $S_u^0(x, y; A_4)$  as the bare part of the solution [69]. The static propagator  $S_u^0(x, y; A_4)$  satisfies the following equation where there is no propagation in the spatial direction

$$-\left(\frac{\gamma_4 + 1}{2}D_4 + m\right)S_u^4(x, y; A_4) = \delta(x - y). \quad (23)$$

It is easy to write down the formal solution for  $S_u^0(x, y; A_4)$

$$S_u^0(x, y; A_4) = -\theta(x_4 - y_4)e^{-m(x_4 - y_4)}\frac{1 + \gamma_4}{2}P\left[\begin{array}{c} x \\ y \end{array}\right]\delta(\vec{x} - \vec{y}) - \frac{\delta(x_4 - y_4)}{m}e^{-m(y_4 - x_4)}\frac{1 - \gamma_4}{2}P\left[\begin{array}{c} x \\ y \end{array}\right]\delta(\vec{x} - \vec{y}) \quad (24)$$

where  $P\left[\begin{array}{c} x \\ y \end{array}\right] \equiv Pe^{ig\int_{y_4}^{x_4} dz_4 A_4}$  is the path-ordered parallel transport factor in the time direction. We see that the usual antiparticle propagation in QCD which involves the  $\theta(y_4 - x_4)$  is now replaced with  $\delta(x_4 - y_4)$  in the second term. Thus,  $S_u^0(x, y; A_4)$  is the static particle propagator which moves forward in time only. Now the full propagator  $S_u(x, y; A)$  can be represented in an integral equation in terms of  $S_u^0(x, y; A_4)$

$$S_u(x, y; A) = S_u^0(x, y; A_4) + \int d^4z S_u^0(x, z; A_4)\vec{\gamma} \cdot \vec{D}S_u(z, y; A). \quad (25)$$

The kernel  $\vec{\gamma} \cdot \vec{D}$  is responsible for hopping in the spatial direction. The full solution can be obtained by substituting  $S_u$  with  $S_u^0$  iteratively leading to a hopping expansion series

$$S_u(x, y; A) = S_u^0(x, y; A_4) + \int_{y_4}^{x_4} dz_4 \int d^3z S_u^0(x, z; A_4)\vec{\gamma} \cdot \vec{D}S_u^0(z, y; A_4) + \int_{z_4}^{x_4} dz'_4 \int_{y_4}^{z'_4} dz_4 \int d^3z' d^3z S_u^0(x, z'; A_4)\vec{\gamma} \cdot \vec{D}S_u^0(z', z; A_4)\vec{\gamma} \cdot \vec{D}S_u^0(z, y; A_4) + \dots \quad (26)$$

It is clear from this expansion that the time integration variables  $z'_4, z_4, \dots$  are sequenced between  $x_4$  and  $y_4$  due to  $\theta$  and  $\delta$  functions in Eq. (24). A typical term in the series is shown graphically in Fig. 17.

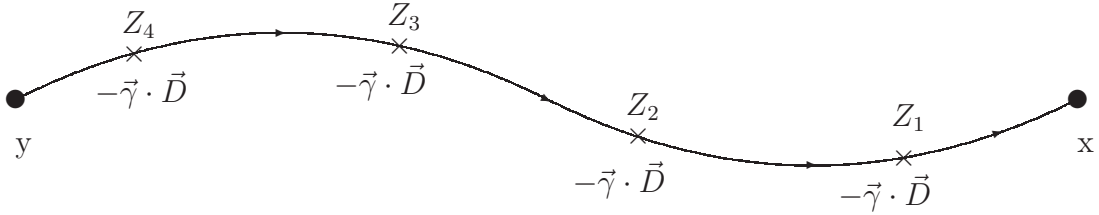


Figure 17: A term in the hopping expansion series in Eq. (26) is graphically presented.

From this we see that there is no time backward propagation in  $S_u(x, y; A)$ . Therefore, there is no pair creation or annihilation in the particle propagator, albeit it still

propagates forward and backward in the spatial direction. Similarly, one can show that the antiparticle propagator  $S_v(x, y; A)$  moves only in the time backward direction.

Although there is no pair creation or annihilation in VQCD, there are still quark loops in the spatial direction which could lead to non-trivial dynamical effect via the fermion determinant. Since we want to emulate the valence quark model, the sea quark degree of freedom needs to be removed also. Therefore, we will not include the fermion determinant in the calculation. In other words, VQCD is inherently “quenched”.

## 4.1 Pauli Spinor Representation

In the process of replacing the fermion field  $\Psi$  in QCD by two Dirac spinors  $u$  and  $v$  in valence QCD (VQCD), we seem to have doubled the degrees of freedom. It turns out that half of the degrees of freedom in  $u$  and  $v$  are not dynamical and thus can be integrated over. As a result, VQCD can be represented by Pauli spinor fields. To prove this, we first look at the particle part of the fermion action from the VQCD lagrangian in Eq. (21) and write it in terms of the upper and lower components

$$\begin{aligned} S_u &= - \int d^4x (\bar{u}_1 \bar{u}_2) \begin{pmatrix} D_4 + m & i\vec{\sigma} \cdot \vec{D} \\ -i\vec{\sigma} \cdot \vec{D} & m \end{pmatrix} \begin{pmatrix} u_1 \\ u_2 \end{pmatrix}, \\ &= - \int d^4x [\bar{u}_1 (D_4 + m - \frac{(\vec{\sigma} \cdot \vec{D})^2}{m}) u_1 \\ &\quad + (\bar{u}_2 + \bar{u}_1 \frac{i(\vec{\sigma} \cdot \vec{D})}{m}) m (u_2 + \frac{-i(\vec{\sigma} \cdot \vec{D})}{m} u_1)]. \end{aligned} \quad (27)$$

After changing the field variables  $u_1 \rightarrow \chi_1$ , and  $u_2 + \frac{-i(\vec{\sigma} \cdot \vec{D})}{m} u_1 \rightarrow \xi_1$ , the action becomes

$$S_u = \int d^4x [\bar{\chi}_1 (D_4 + m - \frac{(\vec{\sigma} \cdot \vec{D})^2}{m}) \chi_1 + \bar{\xi}_1 m \xi_1]. \quad (28)$$

Since the  $\bar{\xi}_1 m \xi_1$  part has no dynamics and is quadratic, it can be integrated over, leaving the particle action represented by the Pauli spinor  $\chi_1$

$$S_u = \int d^4x \bar{\chi}_1 (D_4 + m - \frac{\vec{D}^2 + \vec{\sigma} \cdot \vec{B}}{m}) \chi_1. \quad (29)$$

Similarly, the antiparticle action  $S_v$  can also be written in terms of the Pauli spinor

$$S_v = \int d^4x \bar{\chi}_2 (-D_4 + m - \frac{\vec{D}^2 + \vec{\sigma} \cdot \vec{B}}{m}) \chi_2. \quad (30)$$

We can redefine the Dirac spinor as  $\chi = \begin{pmatrix} \chi_1 \\ \chi_2 \end{pmatrix}$  and rewrite the VQCD lagrangian as

$$\begin{aligned} \mathcal{L}_{VQCD} &= -\frac{1}{4}F_{\mu\nu}F_{\mu\nu} - \chi(\gamma_4 D_4 + m - \frac{\vec{D}^2 + \vec{\sigma} \cdot \vec{B}}{m})\chi \\ &= -\frac{1}{4}F_{\mu\nu}F_{\mu\nu} - (\chi_1 \chi_2) \begin{pmatrix} D_4 + m - \frac{\vec{D}^2 + \vec{\sigma} \cdot \vec{B}}{m} & 0 \\ 0 & -D_4 + m - \frac{\vec{D}^2 + \vec{\sigma} \cdot \vec{B}}{m} \end{pmatrix} \begin{pmatrix} \chi_1 \\ \chi_2 \end{pmatrix} \end{aligned} \quad (31)$$

It is clear from Eq. (31) that particle field  $\chi_1$  and antiparticle field  $\chi_2$  decouple. This also proves that  $\mathcal{L}_{VQCD}$  in Eq. (21) does not double the fermion degrees of freedom. After integrating out the non-dynamical d.o.f. it has exactly 4 propagating spinors as shown in Eq. (31). It is worthwhile remarking that the Pauli form of  $\mathcal{L}_{VQCD}$  in Eq. (31) resembles that of the non-relativistic QCD lagrangian after Foldy-Wouthuysen transformation. It has the single time derivative like in the Schrödinger action and it contains the  $\frac{\vec{D}^2 + \vec{\sigma} \cdot \vec{B}}{m}$  term, much like the non-relativistic expansion. However, we should stress that the Pauli form of VQCD is *not* a non-relativistic or other expansion. Its form is exact. Furthermore, it does not have the spin-orbit, tensor, and Darwin terms as in non-relativistic QCD.

## 4.2 Discrete symmetry

Let's explore the symmetries of VQCD and see if there is any change from QCD. First we examine the discrete symmetries: the parity, charge, and time reversal.

The gluon part of the VQCD is the same as in QCD and there is no need to modify the transformation of the gluon field. For parity and time reversal, the  $u$  and  $v$  fields transform the same way as  $\Psi$  in QCD. Thus in VQCD

$$P \begin{pmatrix} u(x) \\ v(x) \end{pmatrix} P^{-1} = \gamma_4 \begin{pmatrix} u(x^P) \\ v(x^P) \end{pmatrix} \quad (32)$$

$$T \begin{pmatrix} u(x) \\ v(x) \end{pmatrix} T^{-1} = \sigma_2 \begin{pmatrix} u(x^T) \\ v(x^T) \end{pmatrix} \quad (33)$$

where  $x^P = (-\vec{x}, x_4)$ ,  $x^T = (\vec{x}, -x_4)$ . It is easy to show that the VQCD action  $S_{VQCD} = \int d^4x \mathcal{L}_{VQCD}$  is invariant under the above parity and time reversal transformations.

As for the charge transformation, we need to take into account the fact that  $u$  and  $v$  are particle and antiparticle fields which should be transformed into each other under charge transformation. We find that  $S_{VQCD}$  is invariant under the following charge transformation:

$$C \begin{pmatrix} u_\alpha \\ v_\alpha \end{pmatrix} C^{-1} = \begin{pmatrix} (\gamma_2)_{\alpha\beta} v_\beta^\dagger \\ (\gamma_2)_{\alpha\beta} u_\beta^\dagger \end{pmatrix} \quad (34)$$

Thus, with the appropriate definition, VQCD satisfies the C, P, and T invariance.

### 4.3 Continuous Symmetry — $U(2N_F)$

Next, we shall address the continuous symmetries. Since the Dirac structure of the time derivative is modified in VQCD, it is no longer Lorentz invariant, although it is still translational invariant. This should be acceptable for the purpose of our study, i.e. low energy hadron physics near the rest frame. After all, the quark model is supposed to be an effective theory of low energy and small momentum transfer, unlike the parton model which addresses different kinetic regimes.

Like in QCD, VQCD has the global vector and axial symmetries. It is invariant under the  $U(1)$  transformation

$$u \longrightarrow e^{i\alpha}u, v \longrightarrow e^{i\alpha'}v \quad (35)$$

This leads to conserved vector currents

$$\partial_\mu J_\mu^u = 0, \quad \partial_\mu J_\mu^v = 0, \quad (36)$$

where the Noether currents associated with these gauge transformations are

$$J_\mu^u = \bar{u} \begin{pmatrix} i\gamma_i \\ i\frac{\gamma_4+1}{2} \end{pmatrix} u, \quad J_\mu^v = \bar{v} \begin{pmatrix} i\gamma_i \\ i\frac{\gamma_4-1}{2} \end{pmatrix} v. \quad (37)$$

Therefore, the particle and antiparticle are separately conserved. This is in contrast to the conserved current  $J_\mu = \bar{\Psi}i\gamma_\mu\Psi$  in QCD where only the difference of the particle and the antiparticle numbers or the valence number is conserved, i.e.

$$N_v = \int d^3x \bar{\Psi}\gamma_4\Psi = \int \frac{d^3p}{(2\pi)^3} \sum_s [b_s^\dagger(\vec{p})b_s(\vec{p}) - d_s^\dagger(\vec{p})d_s(\vec{p})] \quad (38)$$

where  $b^\dagger/d^\dagger$  and  $b/d$  are the creation and annihilation operators of the particle/antiparticle in QCD.

The axial symmetry of VQCD is realized in the  $\gamma_5$  transformation

$$u \longrightarrow e^{i\theta\gamma_5}u, v \longrightarrow e^{i\theta'\gamma_5}v. \quad (39)$$

The lagrangian  $\mathcal{L}_{VQCD}$  with  $m = 0$  is invariant under this transformation which transposes the  $u$  and  $v$  terms in the lagrangian. As a result, one has the conserved axial currents

$$A_\mu = i\bar{u} \begin{pmatrix} \frac{\gamma_4+1}{2} \\ \gamma_i \end{pmatrix} \gamma_5 v, \quad (40)$$

$$A_\mu^\dagger = i\bar{v} \begin{pmatrix} \frac{\gamma_4-1}{2} \\ \gamma_i \end{pmatrix} \gamma_5 u. \quad (41)$$

We should point out that there is no Adler-Bell-Jackiw anomaly [70] in VQCD. This is so because in VQCD there is no quark loop involving the time direction, hence there is no triangle diagram to generate the axial anomaly. With  $m \neq 0$ , the axial Ward identities are

$$\partial_\mu A_\mu = 2m\bar{u}i\gamma_5 v, \quad (42)$$

$$\partial_\mu A_\mu^\dagger = 2m\bar{v}i\gamma_5 u. \quad (43)$$

It is useful to consider the particle field  $u$  and antiparticle field  $v$  like two flavors and define  $\zeta = \begin{pmatrix} u \\ v \end{pmatrix}$ , then the VQCD lagrangian in Eq. (21) can be written as

$$\mathcal{L}_{VQCD} = -\frac{1}{4}F_{\mu\nu}F_{\mu\nu} - \bar{\zeta}\left[\frac{\gamma_4 + \tau_3}{2}D_4 + \vec{\gamma} \cdot \vec{D} + m\right]\zeta. \quad (44)$$

At the massless limit, VQCD is invariant under the transformation

$$\zeta \longrightarrow e^{i\alpha I}\zeta, \zeta \longrightarrow e^{i\alpha'\tau_3}\zeta, \zeta \longrightarrow e^{i\theta\gamma_5\tau_1}\zeta, \zeta \longrightarrow e^{i\theta\gamma_5\tau_2}\zeta \quad (45)$$

where  $\tau$ 's are the Pauli spinor in the two-component  $u, v$  space. The 4 operators  $I, \tau_3, \gamma_5\tau_1$ , and  $\gamma_5\tau_2$  are the generators of the  $U(2)$  algebra. So, massless VQCD has the  $U(2)$  vector and axial symmetries in the particle-antiparticle space. For degenerate massless  $N_F$  flavors, it has the  $U(2N_F)$  symmetry. It is in contrast to the  $SU(N_F)_L \times SU(N_F)_R \times U_V(1)$  chiral and  $U_V(1)$  symmetry of QCD. In VQCD with  $N_F$  flavors, the charges  $Q_\pm^a = \int d^3x[\bar{u}\gamma_4(t^a/2)u \pm \bar{u}\gamma_4\gamma_5(t^a/2)v]$  do not form a complete  $SU(N_F) \times SU(N_F)$  algebra because the vector and axial current contain different fields. This can also be seen from the states. For massless particle,  $u$  satisfies the Dirac equation

$$\left[\frac{\gamma_4 + 1}{2}D_4 + \vec{\gamma} \cdot \vec{D}\right]u = 0. \quad (46)$$

$\gamma_5 v$  satisfies the same equation

$$\left[\frac{\gamma_4 + 1}{2}D_4 + \vec{\gamma} \cdot \vec{D}\right](\gamma_5 v) = 0. \quad (47)$$

Therefore,  $\chi_\pm = \frac{1}{2}(u \pm \gamma_5 v)$  is a solution of the Dirac equation in Eq. (46), but it has different particle content, i.e. it is a mixture of particle and antiparticle. As a result,  $\chi_\pm$  does not have a definite handedness, it contains both helicity states. From this we conclude that massless VQCD does not have  $SU(N_F)_L \times SU(N_F)_R$  chiral symmetry as in QCD. Instead, it has the vector-axial  $U(2N_F)$  in the flavor and particle-antiparticle space.



## 4.4 Zero Quark Mass Limit

Even though we have explored the axial symmetry of VQCD in Sec. (4.3) at the massless limit, there is a concern that the the zero quark mass limit may be singular. This can be seen from the Dirac equation in Eq. (46) for a free quark

$$\begin{pmatrix} \partial_4 & \vec{\sigma} \cdot \vec{\partial} \\ \vec{\sigma} \cdot \vec{\partial} & 0 \end{pmatrix} \begin{pmatrix} u_1 \\ u_2 \end{pmatrix}. \quad (48)$$

This leads to two Laplace equations for the upper and lower components of the particle field  $u$

$$\nabla^2 u_1 = 0, \nabla^2 u_2 = 0. \quad (49)$$

There are no time derivatives in these constraint equations and thus no dynamics [71]. Similarly, ones sees that the  $\xi$  field in Eq. (28) is ill-defined for the  $m = 0$  case.

To address this problem, we consider the following approach. Let's consider the fermion part of VQCD lagrangian with a small mixture of antiparticle part in the particle action and vice versa

$$\mathcal{L}_F = -\bar{u} \left[ \frac{\gamma_4 + 1}{2} D_4 + \epsilon \frac{\gamma_4 - 1}{2} D_4 + m + \vec{\gamma} \cdot \vec{D} \right] u - \bar{v} \left[ \frac{\gamma_4 - 1}{2} D_4 + \epsilon \frac{\gamma_4 + 1}{2} D_4 + m + \vec{\gamma} \cdot \vec{D} \right] v \quad (50)$$

We will then let both  $m$  and  $\epsilon$  go to zero.

Let's first consider the free quark case. In this case, the fermion lagrangian is

$$\mathcal{L}'_F = -\bar{u} \begin{pmatrix} \partial_4 + m & \vec{\sigma} \cdot \vec{\partial} \\ \vec{\sigma} \cdot \vec{\partial} & -\epsilon \partial_4 + m \end{pmatrix} u - \bar{v} \begin{pmatrix} \epsilon \partial_4 + m & \vec{\sigma} \cdot \vec{\partial} \\ \vec{\sigma} \cdot \vec{\partial} & -\partial_4 + m \end{pmatrix} v. \quad (51)$$

This involves two time derivatives. The eigenvalues for  $u$  are determined from

$$\det \begin{pmatrix} -E + m & i\vec{\sigma} \cdot \vec{p} \\ i\vec{\sigma} \cdot \vec{p} & \epsilon E + m \end{pmatrix} = 0, \quad (52)$$

which are, for small  $\epsilon$ ,

$$E = m + \frac{\vec{p}^2}{m}, \quad (53)$$

$$E = -\frac{m(1 - \epsilon)}{\epsilon} - \left( m + \frac{\vec{p}^2}{m} \right). \quad (54)$$

Note in Eq. (53), the kinetic energy term  $\vec{p}^2/m$  is different from  $\vec{p}^2/2m$  in the non-relativistic case. Now if we let  $\epsilon$  approaches zero faster than  $m$ , the second branch in Eq. (54) will be decoupled from the physical spectrum. At this limit, a gap between

$E = p = 0$  and  $E = \infty$  is created. This could pose a problem for perturbation treatment around this axial symmetry point.

However, the situation is modified when the quarks are interacting. In this case, the Dirac equation for  $u$  is,

$$\begin{pmatrix} D_4 + m & \vec{\sigma} \cdot \vec{D} \\ \vec{\sigma} \cdot \vec{D} & -\epsilon D_4 + m \end{pmatrix} \begin{pmatrix} u_1 \\ u_2 \end{pmatrix}. \quad (55)$$

One of the coupled equation from Eq. (55) is

$$\left(D_4^2 - \frac{m}{\epsilon}(1 - \epsilon)D_4 - \frac{m^2}{\epsilon}\right)u_2 = \frac{(\vec{D}^2 + \vec{\sigma} \cdot B)u_2 + ig\vec{\sigma} \cdot \vec{E}u_1}{\epsilon}. \quad (56)$$

If we let  $m$  and  $\epsilon$  approaches zero at the same rate such that  $m/\epsilon = \lambda \gg \lambda_{QCD}$ , the left-hand side of Eq. (56) leads to a constraint equation

$$(\vec{D}^2 + \vec{\sigma} \cdot B)u_2 + ig\vec{\sigma} \cdot \vec{E}u_1 = 0. \quad (57)$$

The right-hand side leads to two equations, both with linear time dependence

$$D_4 u_2 = 0, \quad (58)$$

$$(D_4 - \lambda)u_2 = 0. \quad (59)$$

Since  $\lambda \gg \lambda_{QCD}$ , the solution from Eq. (59) is decoupled from the physical system of the hadrons.

Therefore, the Dirac equation for the interacting massless quark with the  $\epsilon$  regulator leads to the following coupled equations,

$$D_4 u_1 + i\vec{\sigma} \cdot \vec{D} u_2 = 0, \quad (60)$$

$$D_4 u_2 = 0, \quad (61)$$

with Eq. (57) as a constraint. This should admit propagating solutions. Similar situation exists for  $v$ . Thus, we can approach the interacting massless quark case with the help of the infrared  $\epsilon$  regulator.

## 5 Lattice VQCD

In order to solve VQCD, we need a lattice version like in QCD. To this end, we shall devise a lattice VQCD action based on Wilson's action in QCD. We shall use the following lattice VQCD action

$$S_{VQCD}^L = S_G + S_F^u + S_F^v \quad (62)$$

where  $S_G$  is Wilson's gauge action which is preserved here and the quark action  $S_F^u$  and the antiquark action  $S_F^v$  are

$$S_F^u = \sum_x [\bar{u}(x)u(x) - \kappa(\bar{u}(x+a_4)(1+\gamma_4)U_4^\dagger(x)u(x) + u_0\bar{u}(x)(1-\gamma_4)u(x)) - \kappa \sum_i (\bar{u}(x+a_i)(1+\gamma_i)U_i^\dagger(x)u(x) + \bar{u}(x)(1-\gamma_i)u(x+a_i))] \quad (63)$$

$$S_F^v = \sum_x [\bar{v}(x)v(x) - \kappa(\bar{v}(x)(1-\gamma_4)U_4(x)u(x+a_4) + u_0\bar{v}(x)(1+\gamma_4)v(x)) - \kappa \sum_i (\bar{v}(x+a_i)(1+\gamma_i)U_i^\dagger(x)v(x) + \bar{v}(x)(1-\gamma_i)v(x+a_i))] \quad (64)$$

where  $u_0$  is the tadpole contribution of the gauge link  $U_\mu$  which we take to be  $(Tr\Box)^{1/4}$  [72]. This has the VQCD in Eq. (21) as the classical continuum limit.

## 5.1 Reflection Positivity and Hermiticity

Similar to the continuum case in Sec. (4.2), lattice VQCD action in Eq. (62) is invariant under the corresponding lattice C, P, and T transformations.

For Euclidean action, it is imperative that it satisfies Osterwalder-Schrader reflection positivity [73] in order to allow the Euclidean correlations to be continued back to the Minkowski space. We shall follow the derivation for the Wilson action [74]. To prove reflection positivity, one needs to show

$$\langle (\Theta F)F \rangle \geq 0 \quad (65)$$

where F is a function of the fields  $\bar{u}, u, \bar{v}, v$ , and  $U$  on the positive time part of the lattice and  $\Theta$  is the time reflection operator. We shall consider the 'link-reflection' case where the time reflection is with respect to the  $t = (0 \rightarrow 1)$  link. In this case,  $\Theta$  is defined by the transformation

$$\Theta u_{x,t} = \bar{u}_{x,1-t}\gamma_4, \Theta \bar{u}_{x,t} = \gamma_4 u_{x,1-t}, \quad (66)$$

$$\Theta v_{x,t} = \bar{v}_{x,1-t}\gamma_4, \Theta \bar{v}_{x,t} = \gamma_4 v_{x,1-t}, \quad (67)$$

$$\Theta U(x, t_x; y t_y) = U^\dagger(x, 1-t_x; y, 1-t_y). \quad (68)$$

Let's illustrate the proof with the u part of the action alone. The proof can be extended similarly to include the v field. Denoting the field variables in the half-space with positive time  $t \geq 1$  by  $u^+, \bar{u}^+, U^+$ , and in the other half-space with  $t \leq 0$  by  $u^-, \bar{u}^-, U^-$ , the VQCD action can be separated into three parts

$$S_{VQCD} = S_+[\bar{u}^+, u^+, U^+] + S_-[\bar{u}^-, u^-, U^-] + S_c[\bar{u}^+, u^-], \quad (69)$$

where

$$S_c[\bar{u}^+, u^-] = -\kappa \sum_{\vec{x}} [\bar{u}_{\vec{x},1}^+(1+\gamma_4)u_{\vec{x},0}^-], \quad (70)$$

is the action which connects  $S_+$  and  $S_-$  and involves links between  $t = 0$  and  $t = 1$ . Here we have used the temporal gauge. Now since

$$\Theta S_+[\bar{u}^+, u^+, U^+] = S_+^\dagger[\Theta\bar{u}^+, \Theta u^+, \Theta U^+] = S_-[\bar{u}^-, u^-, U^-], \quad (71)$$

the integral in Eq. (65) is then

$$\begin{aligned} \langle (\Theta F) F \rangle &= Z^{-1} \int dU d\bar{u}^+ du^+ e^{-S_+[\bar{u}^+, u^+, U^+]} F[\bar{u}^+, u^+, U^+] \\ &\cdot \int d(\Theta\bar{u}^+) d(\Theta u^+) e^{-S_+^\dagger[\Theta\bar{u}^+, \Theta u^+, \Theta U^+]} F^\dagger[\Theta\bar{u}^+, \Theta u^+, \Theta U^+] \\ &e^{-\kappa \sum_{\vec{x}} \bar{u}_{\vec{x},1}^+ (\gamma_4 + 1) (\Theta \bar{u}_{\vec{x},1}^+)}. \end{aligned} \quad (72)$$

Consider the Taylor expansion of the last exponential in Eq. (72)

$$1 - \kappa \sum_{\vec{x}} \bar{u}_{\vec{x},1}^+ (\gamma_4 + 1) (\Theta \bar{u}_{\vec{x},1}^+) + \dots \quad (73)$$

The only terms that survive the Grassmann integration are the first two terms and, with a diagonal representation of  $\gamma_4$ , they give semi-positive definite contributions to  $\langle (\Theta F) F \rangle$ . Extension to include the  $v$  field is straightforward and thus the reflection positivity for the VQCD action is proved.

In constructing meson propagators, the usual practice is to first invert the quark matrix to obtain the quark propagator from the source to all lattice points, i.e.  $M^{-1}(x, 0)$ . Then the anti-quark propagator which goes backward in time is obtained through the hermiticity relation

$$M^{-1\dagger}(0, x) = \gamma_5 M^{-1}(x, 0) \gamma_5, \quad (74)$$

where  $\dagger$  indicates the hermitian conjugation in the color and Dirac indices. In VQCD, a similar situation exists. In constructing a  $q\bar{q}$  meson, one needs the quark propagator  $M_u^{-1}(x, 0)$  and the anti-quark propagator  $M_v^{-1}(0, x)$ . It turns out that the hermiticity relation

$$M_v^{-1\dagger}(0, x) = \gamma_5 M_u^{-1}(x, 0) \gamma_5, \quad (75)$$

still exists so that one can obtain the anti-quark propagator from the quark to construct a meson propagator as before.

## 5.2 Free Quark Propagator

It is useful to understand the free quark spectrum and its residue at the pole for the lattice VQCD and see how different it is from the Wilson and the continuum ones. The inverse of the free quark propagator of VQCD in momentum space is

$$S_F^{u-1}(p) = 1 - \kappa(1 - \gamma_4) - \kappa(1 + \gamma_4)e^{-ip_4a} - \kappa \sum_i [(1 + \gamma_i)e^{-ip_i a} + (1 - \gamma_i)e^{ip_i a}], \quad (76)$$

where  $a$  is the lattice spacing. We can compute the propagator in discrete time  $t = n_t a$

$$S_F^u(t, \vec{p}) = \int_{-\pi}^{\pi} \frac{dp_4}{2\pi} S_F^u(p) e^{ip_4 t} \quad (77)$$

For  $n_t > 0$  and  $\vec{p}$  in the 3 direction,

$$S_F^u(t, p_3) = \frac{e^{-Et}}{B} [A - \kappa e^{Ea} + \kappa(e^{Ea} - 1)\gamma_4 - 2i\kappa\gamma_3 \sin(p_3 a)], \quad (78)$$

where

$$\begin{aligned} A &= 1 - 5\kappa - 2\kappa \cos(p_3 a), \\ B &= A^2 - \kappa^2 + 4\kappa^2 \sin^2(p_3 a), \\ Ea &= \ln\left(\frac{B}{2A\kappa - 2\kappa^2}\right). \end{aligned} \quad (79)$$

$E$  is the energy. For small  $p_3 a$ , i.e.  $p_3 a \ll 1$ ,

$$Ea = \bar{m}a + \frac{ma + 2}{2ma(ma + 1)} (p_3 a)^2, \quad (80)$$

where

$$\bar{m}a = \ln\left(\frac{1 - 6\kappa}{2\kappa}\right), \quad (81)$$

is the free quark mass which is the same as in the Wilson case and  $ma = \frac{1}{2\kappa} - 4$  is the small mass approximation for  $\bar{m}a$ .

We plot in Fig. 18, the dispersion relation of  $Ea$  vs.  $p_3 a$  for a range of  $ma$  ( $ma = 0.05, 0.1, 0.5, \text{ and } 1.0$ ) for both the Valence (dashed lines) and the Wilson case (solid lines). We see that for heavy quarks, i.e.  $ma = 0.5$  and  $1$ , the two curves at the top are close to each other and they differ at small mass and low momentum. At small  $p_3 a$ , the behavior of Eq. (80) holds for the valence case. At  $ma = \bar{m}a = 0$ , there is a singularity at  $Ea = p_3 a = 0$ . For any finite  $p_3 a$ ,  $Ea = \ln 3$  which resembles the infinite gap in the massless free quark situation in the continuum (see Eq. (53)).

Finally, we see at zero momentum, the static propagator is

$$S(t > 0, \vec{p} = 0) = \frac{1}{1 - 6\kappa} e^{-\bar{m}t} \frac{1 + \gamma_4}{2}. \quad (82)$$

This is the same as in the Wilson case and the wave function normalization factor  $\frac{1}{1 - 6\kappa}$  is also the same. To convert lattice matrix elements of local currents with bilinear quark fields, e.g.  $\bar{\Psi}(x)\Gamma\Psi(x)$  to the continuum ones, besides the finite lattice renormalization one needs to multiply the factor  $\frac{1 - 6\kappa u_0}{2\kappa} = u_0 e^{m_q a}$  to take into account the finite mass normalization due to the Wilson quark action with tadpole improvement [72, 44]. Here  $u_0 = \frac{1}{8\kappa_c}$  where  $\kappa_c$  is the critical  $\kappa$  at which point the pion mass is zero and  $m_q a = \ln\left(\frac{1}{2\kappa u_0} - 3\right)$  is the tadpole improved definition of the bare quark mass in Eq. (81).

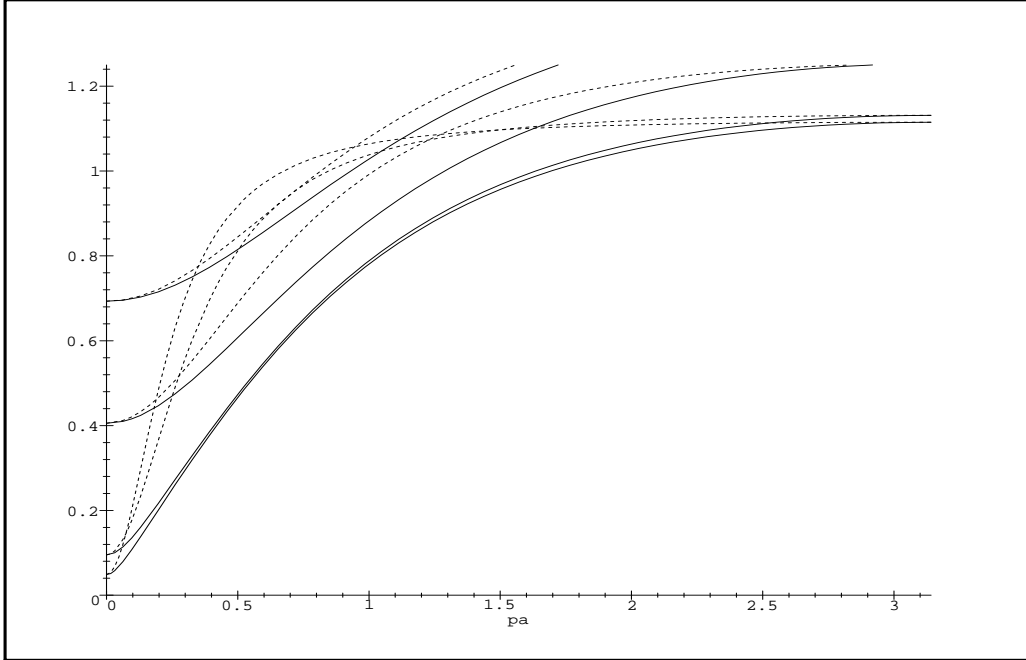


Figure 18: The dispersion relations between  $Ea$  and  $p_3a$  for a free quark are compared between the Wilson (solid lines) and the lattice VQCD (dashed lines) version for  $ma = 0.05, 0.1, 0.5,$  and  $1.0$ .

### 5.3 Lattice Details

Before we present our results on VQCD from the Monte Carlo calculation, we should mention the lattice specifics and the details of the calculation.

We use the same gauge configurations which have been used for the study of hadron masses, matrix elements and form factors [44, 65, 20, 21, 57] in the quenched approximation. This way we keep the scale of the lattice spacing unchanged. These quenched gauge configurations were generated on a  $16^3 \times 24$  lattice at  $\beta = 6.0$ . The gauge field was thermalized for 5000 pseudo-heatbath sweeps from a cold start and 100 configurations separated by at least 1000 sweeps were used. Periodic boundary conditions were imposed on the quark fields in the spatial directions. In the time direction, fixed boundary conditions were imposed on the quarks to provide larger time separations than available with periodic boundary conditions. As long as the time separations  $t_1$  and  $t - t_1$  in Fig. 5(a) are large enough, the form factors should not depend on the nucleon interpolation field. All quark propagators in the quenched approximation were chosen to originate from lattice time slice 5; the secondary nucleon source was fixed at time slice 20 (except for  $\kappa = 0.154$  where the quark propagators

from time slice 3 to 22 were used). In the case of VQCD, all quark propagators originate from time slice 2 and terminate at time slice 22 for the three-point function calculation. We also averaged over the directions of equivalent lattice momenta in each configuration; this reduces error bars.

We have verified that the time separation is sufficient so that there is a plateau for the quark bilinear current insertion at time slices  $t_1$  after the nucleon ground state is achieved. The quenched approximation part is done for the lightest quarks with  $\kappa = 0.154, 0.152, 0.148$ , and  $0.140$ , and  $\vec{q}^2 a^2$  up to  $4(2\pi/L)^2$ . The nucleon masses  $M_N a$  for  $\kappa = 0.154, 0.152$ , and  $0.148$  are  $0.731(11)$ ,  $0.883(9)$ , and  $1.153(7)$  respectively. The corresponding pion masses  $m_\pi a$  are  $0.375(4)$ ,  $0.487(3)$ , and  $0.679(3)$ . Extrapolating the nucleon and pion masses to the chiral limit where we determine  $\kappa_c = 0.15672(4)$  and the nucleon mass at the chiral limit to be  $0.536(13)$ . Using the nucleon mass to set the scale which we believe to be appropriate for studying nucleon properties [44, 65, 20], the lattice spacing  $a^{-1} = 1.75(2)$  GeV is determined. The three  $\kappa$ 's then correspond to quark masses of about 120, 205, and 370 MeV respectively.

Since we use the same gauge configurations for VQCD, the lattice spacing is the same as that in the quenched approximation. This is certainly obvious if we choose the string tension or the glueball mass to set the scale. Using the physical nucleon mass to set the scale in the quenched approximation opens up the question as to what extent the fermion determinant effects are implicitly included. It is shown [76] that the quenched approximation can be viewed as including the leading terms in the loop expansion of the fermion determinant which are commensurate with the size of loops in the gauge action. This leads to a shift in  $\beta$  or the coupling constant. However, when the infinite volume and continuum limits are taken [77], the scales due to hadron masses and the string tension are consistent. Since we are not at the infinite volume and continuum limits, the scale set by the nucleon mass differs from that by the string tension by  $\sim 20\%$ . This is the caveat that we should be aware of. Nevertheless, whatever scale we decide to choose, the lattice spacing is the same in the following VQCD calculation as that in our quenched approximation.

The determination of  $\kappa_c$  which corresponds to the zero quark mass will be discussed in the next section. To determine the finite quark mass, we shall use the tadpole improved form of the lattice free-quark mass in Eq. (81), i.e.

$$m_q a = \ln\left(\frac{1}{2\kappa u_0} - 3\right) = \ln\left(\frac{4\kappa_c}{\kappa} - 3\right), \quad (83)$$

where we have used  $u_0 = \frac{1}{8\kappa_c}$ .

## 5.4 Pion Decay Constant, Pion Mass and $\kappa_c$

Pion decay constant  $f_\pi$  plays an essential role in understanding low-energy chiral dynamics and chiral symmetry breaking in QCD. It sets the scale for chiral per-

turbation, and relates the Goldstone boson mass to the quark mass through the Gell-Mann-Oakes-Renner's relation [75]

$$f_\pi^2 m_\pi^2 = -(m_u + m_d) \langle \bar{q}q \rangle, \quad (84)$$

where  $\langle \bar{q}q \rangle$  is the quark condensate, which is the order parameter for chiral symmetry breaking. In VQCD, it is not clear if there is a corresponding relation, or more importantly, if the  $U(2N_f)$  symmetry is broken to generate Goldstone bosons. We can, however, look for clues from the pion decay matrix element with the axial current. In QCD, the pion decay constant is defined by

$$\langle 0 | A_\mu(x) | \pi(p) \rangle = i f_\pi p_\mu e^{ip \cdot x}. \quad (85)$$

Applying axial identity from Eq. (43) to the zero-momentum pion state, we obtain in VQCD

$$\begin{aligned} \langle 0 | \partial_4 A_4^\dagger(x) | \pi(0) \rangle &= -m_\pi^2 f_\pi(m_\pi) e^{-m_\pi t} \\ &= 2m \langle 0 | \bar{v} i \gamma_5 u | \pi(0) \rangle e^{-m_\pi t}, \end{aligned} \quad (86)$$

where  $m$  is the quark mass. From this, we find

$$-m_\pi^2 \frac{f_\pi(m_\pi)}{\langle 0 | \bar{v} i \gamma_5 u | \pi(0) \rangle} = 2m. \quad (87)$$

It is clear from Eq. (87) that as long as the ratio  $f_\pi(m_\pi) / \langle 0 | \bar{v} i \gamma_5 u | \pi(0) \rangle$  does not diverge as fast as  $1/m_\pi^2$  when the quark mass approaches zero, the pion mass will go to zero at massless quark limit. Furthermore, if the pion decay constant  $f_\pi$  is not zero at the massless limit, it would signal spontaneous axial symmetry breaking with the pion as the Goldstone boson.  $f_\pi$ ,  $m_\pi$  and the current quark mass  $m$  from lattice VQCD are calculated in the standard way by fitting the following two-point functions to

$$\langle \sum_{\vec{x}} [i \bar{v} \frac{\gamma_4 - 1}{2} \gamma_5 u(\vec{x}, t)] P(0, 0) \rangle \xrightarrow{t \gg a} \frac{f_\pi m_\pi Z_\pi}{2m_\pi} e^{-m_\pi t}, \quad (88)$$

$$\langle \sum_{\vec{x}} [i \partial_t \bar{v} \frac{\gamma_4 - 1}{2} \gamma_5 u(\vec{x}, t)] P(0, 0) \rangle \xrightarrow{t \gg a} \frac{2m Z_\pi^2}{2m_\pi} e^{-m_\pi t}, \quad (89)$$

$$\langle \sum_{\vec{x}} P(\vec{x}, t) P(0, 0) \rangle \xrightarrow{t \gg a} \frac{Z_\pi^2}{2m_\pi} e^{-m_\pi t}. \quad (90)$$

Here  $P$  is the pseudoscalar interpolation field  $\bar{u} i \gamma_5 v$  and  $Z_\pi = \langle \pi | P | 0 \rangle$  is the wave function overlap. We use the local current for the axial current in Eq. (88) for the lattice calculation. There are finite lattice renormalizations associated with the operators in these matrix elements. We have not calculated them, but we expect the multiplicative renormalization constants  $Z_A$  and  $Z_P$  for the axial and pseudoscalar



operators to be of order 1, as in the quenched approximation. Our results presented below are subject to this caveat.

With Wilson-type fermions, one needs to find out where the  $\kappa_c$  is for zero quark mass. To determine  $\kappa_c$ , we plot the dimensionless pion mass, the current quark mass, and the pion decay constant in Fig. 19 as a function of  $m_q a = \ln(4\kappa_c/\kappa - 3)$  where  $\kappa_c$  is to be determined from the extrapolation. We see that the pion mass is very linear in the range of the quark mass that we calculated. At the same time, the pion decay constant  $f_\pi$  behaves like  $1/m_\pi$  in this range. Since from Eq. (88) and Eq. (89) we have the relation

$$f_\pi(m_\pi)m_\pi^2 = 2mZ_\pi, \quad (91)$$

if the linear behavior between  $m_\pi$  and  $m$  persists all the way down to zero quark

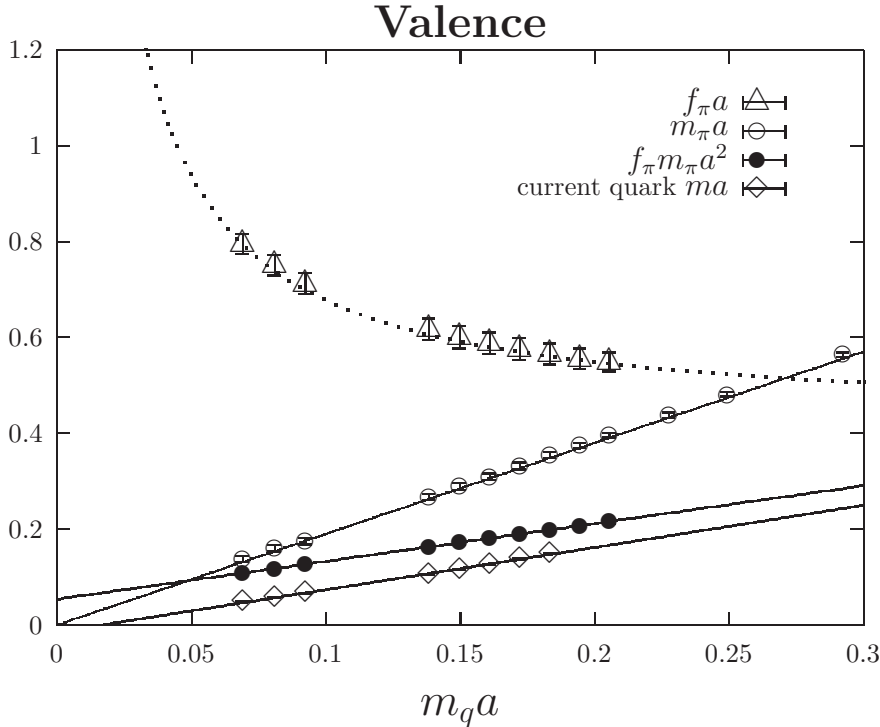


Figure 19: The dimensionless pion mass  $m_\pi a$ , the current quark mass  $ma$ , and the pion decay constant  $f_\pi a$  are shown as a function of  $m_q a = \ln(4\kappa_c/\kappa - 3)$ . The solid lines represent the linear extrapolation with respect to  $m_q a$ .

mass and  $Z_\pi$  remains constant, then  $f_\pi$  will diverge like  $1/m_\pi$  or  $1/m$ . Alternatively, at smaller quark mass than we calculated here,  $f_\pi$  could conceivably turn flat and in this case  $m_\pi$  will fall off like  $\sqrt{m}$  as in QCD with a constant  $Z_\pi$ . Unfortunately, using conjugate gradient to invert the quark matrix, we have encountered critical slowing down. The smallest quark mass we run at  $\kappa = 0.162$  already takes 5,000 iterations to converge. It is impractical for us to go down any further. Short of theoretical guidance and numerical evidence, we extrapolate the pion mass

to zero both linearly and quadratically with respect to  $m_q a = \ln(4\kappa_c/\kappa - 3)$  with  $\kappa = 0.162, 0.1615, 0.1610, 0.1590, 0.1585, 0.1580, 0.1575, 0.1570, 0.1565, 0.1560, 0.155, 0.154, 0.152, \text{ and } 0.148$ . We found that  $\kappa_c = 0.1649(10)$  ( $\chi^2 = 0.002$  with 14 data points) for the linear dependence and  $\kappa_c = 0.1636(19)$  ( $\chi^2 = 0.04$  from the three largest  $\kappa$ 's) for the quadratic dependence. We plot in Fig. 20 the quadratic fit of  $m_\pi$  as a function of  $m_q a$  with  $\kappa_c$  determined from the linear  $m_\pi$  fit. We see that the  $\kappa_c$  point from the quadratic fit crosses the abscissa at  $m_q a = 0.031$ , however, its error bar overlaps with that from the linear  $m_\pi$  fit. Also plotted in Figs. 19 and 20 is the current quark mass  $ma$  from Eq. (89) as a function of  $m_q a$ . Extrapolating the quark mass linearly with respect to  $m_q a$ , we obtain  $\kappa_c = 0.1642(9)$  ( $\chi^2 = 3.5$  from the first 8  $\kappa$ 's). We have not used covariance matrix in these extrapolations. We see that the current quark mass  $ma$  from Eqs. (87) and (89) crosses the abscissa at  $m_q a = 0.017$ . This is consistent with that extrapolated from the pion mass, either linearly or quadratically. The  $\kappa_c$  so obtained overlaps with both of the above two  $\kappa_c$ 's within errors. It is gratifying to know that different definitions of  $\kappa_c$  agree. On the other hand, it does not differentiate the two scenarios of the pion mass dependence on the quark mass. We shall use the linear extrapolation with  $\kappa_c = 0.1649(10)$  to define zero quark mass in this study. Also plotted in Fig. 20 is  $f_\pi m_\pi^2 a^3$ . We see that it is

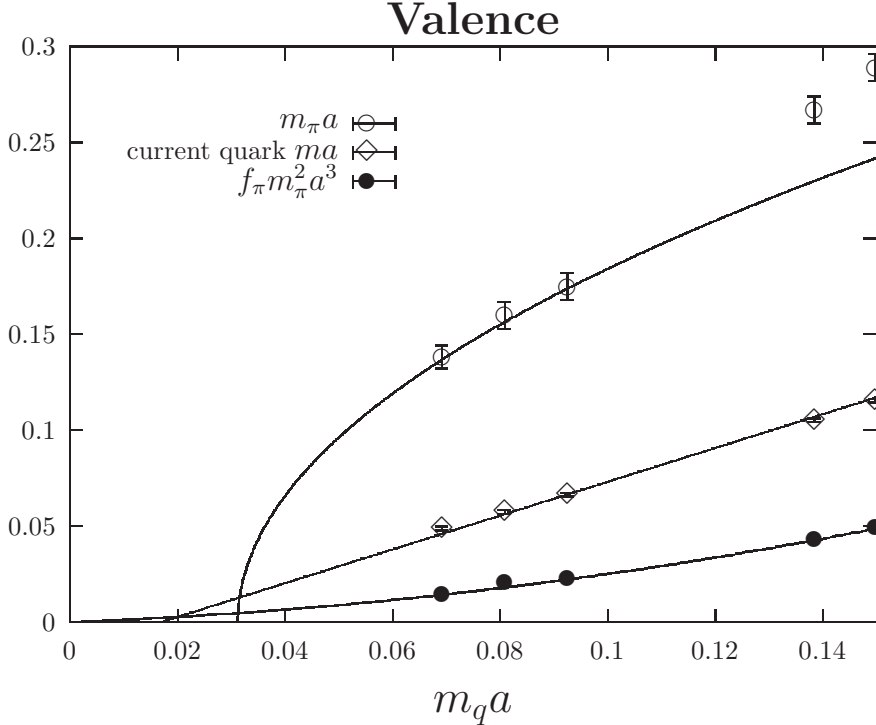


Figure 20: The dimensionless pion mass  $m_\pi a$ ,  $f_\pi m_\pi^2 a^3$ , and current quark mass  $ma$  are shown as a function of  $m_q a = \ln(4\kappa_c/\kappa - 3)$  with  $\kappa_c$  determined from the linear fit of  $m_\pi$  with respect to  $m_q a$ .

quite linear in the range of quark mass that we have considered. This confirms that  $f_\pi m_\pi^2 \propto m_q$  or equivalently Eq. (91), since we have just shown in Fig. 20 that  $m_q a$  and  $ma$  are linearly related. We should stress that we still do not know the behavior of the pion mass and pion decay constant when the quark mass is small. But, at least we can say that  $f_\pi$  is non-zero (divergent or not) and  $m_\pi$  approaches zero at the massless quark limit. This we take to be the evidence that there is a spontaneous axial symmetry breaking with the two pions  $\bar{u}i\gamma_5 v$  and  $\bar{v}i\gamma_5 u$  as the Goldstone bosons for each flavor.

## 6 $SU(6)$ Relations

We shall first examine the ratios  $R_A$  in Eq. (10),  $R_S$  in Eq. (15) and the neutron to proton magnetic moment ratio  $\mu^n/\mu^p$  to check their  $SU(6)$  relations as compared to those in full QCD, albeit with quenched approximation. In VQCD, the sea quark contributions (e.g. Fig. 5(b)) are scrapped. We will only consider the connected insertions (e.g. Fig. 4(a) and 5(a)).

### 6.1 $R_A$ and $F_A/D_A$

The same 100 gauge configurations used for the earlier  $R_A$  calculation in Sec. 3.1.1 are used for the VQCD case. Since in VQCD, there is only the C. I., the  $R_A$  ratio becomes

$$R_A = \frac{g_A^0}{g_A^3}(C.I.) = \frac{(\Delta u + \Delta d)(C.I.)}{(\Delta u - \Delta d)(C.I.)}. \quad (92)$$

We plot it in Fig. 21 as a function of the dimensionless quark mass  $m_q a$  (with  $\kappa = 0.162, 0.1615, 0.1610, 0.1590,$  and  $0.1585$ ) together with the corresponding results from the quenched calculation presented earlier in Fig. 6 in Sec. 3.1.1. We see that, even for light quarks in the strange region ( $m_q a \sim 0.07$ ), it is much closer to the valence prediction of  $3/5$ , in contrast to the QCD calculation with C. I. alone.

This shows that VQCD indeed seems to confirm our expectation of the valence quarks behavior, i.e. obeying the  $SU(6)$  relation. The deviation from the exact  $3/5$  prediction in Fig. 21 reflects the fact that there are still spin-spin interaction between the valence quarks as evidenced in the  $\vec{\sigma} \cdot \vec{B}$  term in the VQCD action with Pauli spinors in Eq. (29). Its effects, however, appear to be small. This also confirms our earlier assertion that the deviation of the C. I. of  $R_A$  in QCD ( $\circ$  in Fig. 21) is largely due to the the cloud quark-antiquark pairs.

With only the C. I., the  $F_A/D_A$  ratio is related to VQCD  $R_A$  in Eq. (92)

$$\frac{F_A}{D_A}(C.I.) = \frac{1 + R_A}{3 - R_A}, \quad (93)$$

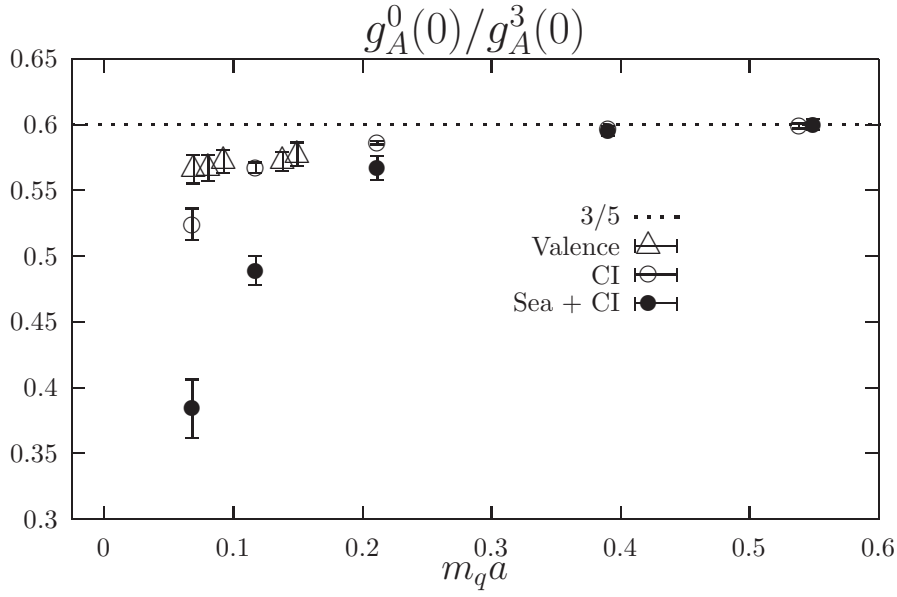


Figure 21: The ratio  $R_A$  between isoscalar and isovector  $g_A$  in VQCD and QCD are plotted against the dimensionless quark mass  $m_q a$  from the strange to the charm region.  $\triangle$  indicates the VQCD case,  $\circ/\bullet$  indicates the C. I./ Sea + C. I. in the QCD case. The dashed line is the  $SU(6)$  prediction of  $3/5$ .

From  $R_A = 0.566(11)$  for the smallest quark mass ( $\kappa = 0.162$ ), we obtain  $F_A/D_A = 0.643(4)$ . This is larger than the QCD prediction of  $0.60(2)$  for the C. I. (see Table 1) and closer to the valence quark prediction of  $2/3$ .

## 6.2 $R_S$ and $D_S/F_S$

Similar results are obtained for the  $R_S$  ratio in VQCD. In this case,

$$R_S = \frac{(\langle p|\bar{u}u + \bar{d}d|p\rangle)(C.I.)}{(\langle p|\bar{u}u - \bar{d}d|p\rangle)(C.I.)}. \quad (94)$$

Plotted in Fig. 22 are the VQCD results together with those from QCD in Fig. 7 as a function of the quark mass  $m_q a$ . Again, we find that the ratios for the light quarks are approaching the valence quark prediction of 3. This again confirms that the deviation of the C. I. result in QCD is primarily due to the Z-graphs with cloud quarks and antiquarks. When they are eliminated in VQCD,  $R_S$  becomes close to the  $SU(6)$  relation.

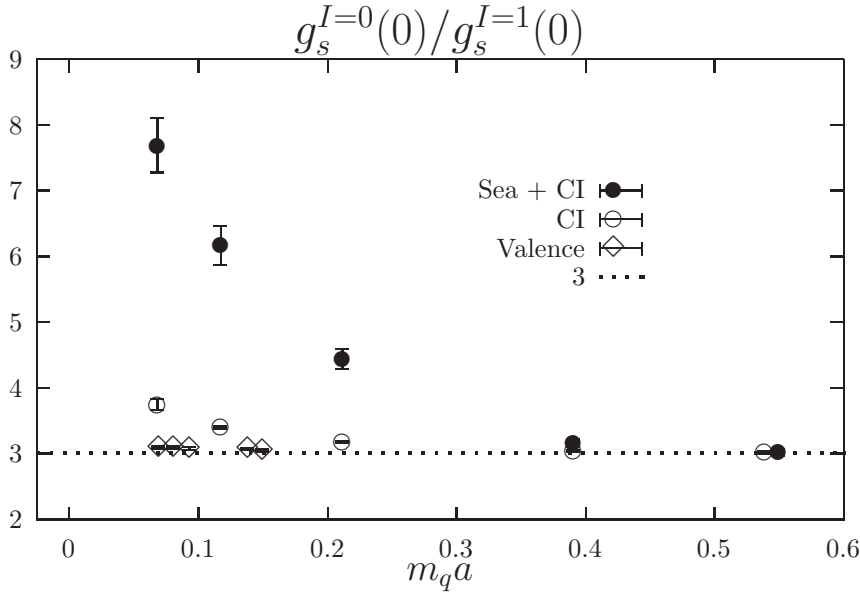


Figure 22: The ratio  $R_S$  between isoscalar and isovector scalar charge in VQCD and QCD are plotted against the dimensionless quark mass  $m_q a$  from the strange to the charm region.  $\triangle$  indicates the VQCD case and  $\circ/\bullet$  indicates the C. I./ Sea + C. I. in the QCD case. The dashed line is the valence quark prediction of 3.

The  $D_S/F_S$  ratio in VQCD is

$$D_S/F_S(C.I.) = \frac{3 - R_S}{1 + R_S}, \quad (95)$$

From  $R_S = 3.086(19)$  for the smallest quark mass ( $\kappa = 0.162$ ), we obtain  $D_S/F_S = -0.021(4)$  which is close to zero as in the valence quark picture (Table 2) and differs from the lattice QCD calculation of  $-0.58(18)$  (Sea + C. I.) and  $-0.31(11)$  (C. I.) (see Table 2) by a large margin.

### 6.3 Neutron to Proton Magnetic Moment Ratio

We next come to the neutron to proton magnetic moment ratio  $\mu^n/\mu^p$ . The results of VQCD (indicated as  $\triangle$  in Fig. 23) are very close to the well-known  $SU(6)$  value of  $-2/3$  (the result for the smallest quark mass case is  $-0.662(22)$ ), indirectly verifying the cloud effects of QCD ( $\circ$  for the C. I. in Fig. 23) which shows a  $2.5\sigma$  departure from  $-2/3$  at the chiral limit. If there is any deviation of the VQCD from  $-2/3$ , it should be due to the residual spin-spin interaction between the quarks in the baryon. Given the size of the error in our present results, we cannot make a definite conclusion on this aspect.

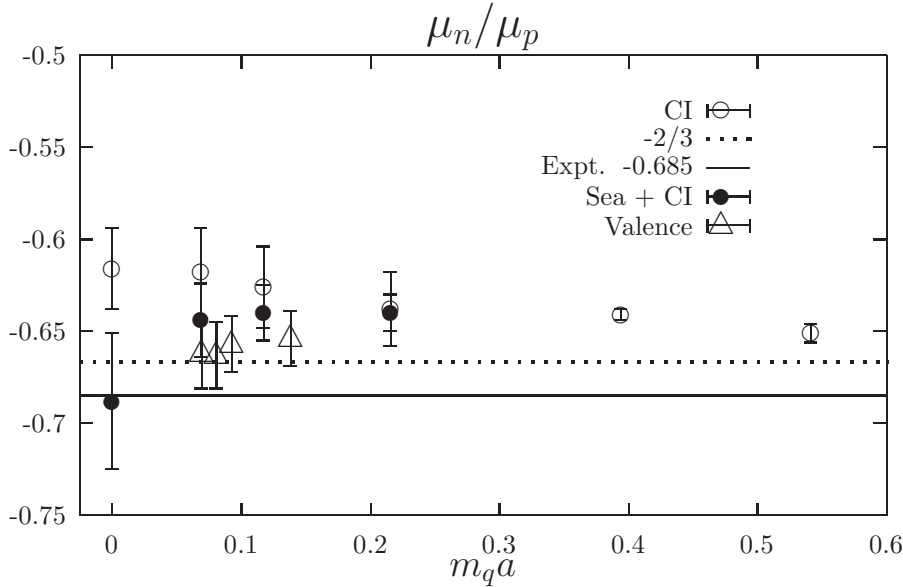


Figure 23: The magnetic moment ratio  $\mu^n/\mu^p$  between neutron and proton in VQCD and QCD are plotted against the dimensionless quark mass  $m_q a$  from the strange to the charm region.  $\triangle$  indicates the VQCD case and  $\circ/\bullet$  indicates the C. I./ Sea + C. I. in QCD case. The dashed line is the  $SU(6)$  prediction of  $-2/3$ .

## 7 Form Factors

Now, we revisit the form factors of the nucleon. We calculated the isovector-axial form factor  $g_A^3(q^2)$ , the isoscalar-scalar form factor  $g_S^0(q^2)$ , the proton electric form factor  $G_E^p(q^2)$  and the isovector pseudoscalar form factor  $g_P^3(q^2)$  in VQCD at  $\kappa = 0.162$ , which corresponds to the quark mass of  $\sim 120$  MeV. They are plotted in Fig. 24 as a function of  $-q^2$ . For comparison, we also plot in Fig. 25 the corresponding form factors from QCD at  $\kappa = 0.154$ , which is about the same quark mass as in the VQCD case.

We see that although these form factors in VQCD are still different among themselves, the differences are relatively smaller compared to those in QCD first of all, and secondly they are overall harder (except for  $g_S^0(q^2)$ ), i.e. they fall off slower than the corresponding ones in QCD. The most dramatic change is the pseudoscalar form factor where the size as determined by

$$\langle r^2 \rangle = -6 \frac{dF(q^2)}{d(-q^2)} \Big|_{q^2=0}, \quad (96)$$

is reduced by about a factor of two. This is consistent with the pseudoscalar meson-dominance picture in Fig. 11, where the pseudoscalar form factor in QCD is dominated by the pion which in turn couples to the baryon through the  $\pi NN$  vertex. Yet, this meson ‘cloud’ is removed in VQCD by prohibiting the pair creation. In this case, the current couples directly to the quarks and consequently the  $\langle r^2 \rangle$  of the hadron becomes smaller. To a lesser extent, similar situations happen in the vector and axial channels. This is again an indirect way of visualizing the effects of the meson clouds in the C. I. of QCD.

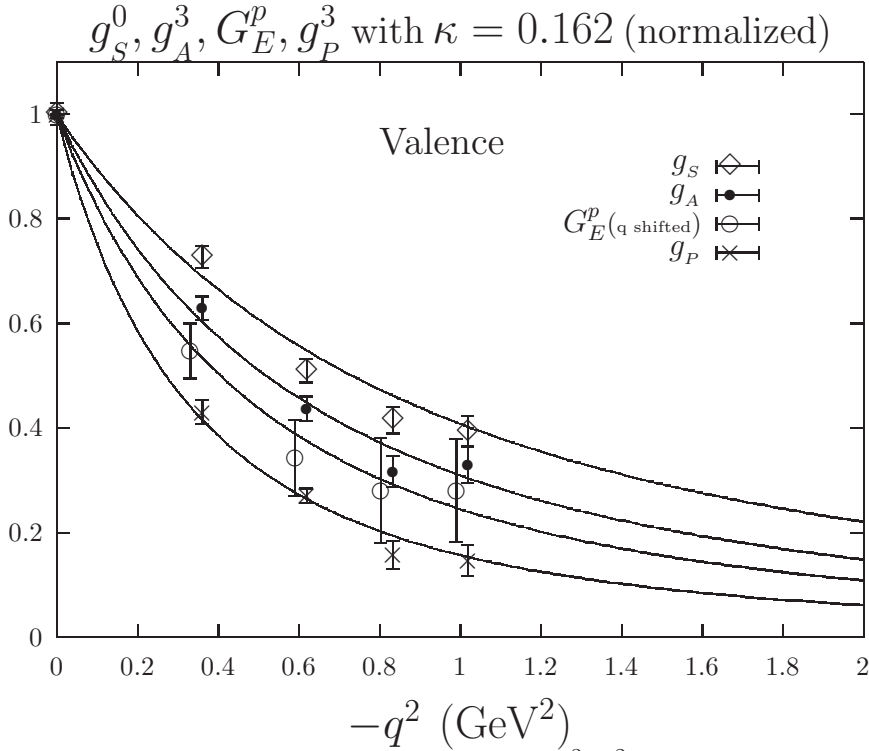


Figure 24: The isovector axial form factor  $g_A^3(q^2)$ , the isoscalar scalar form factor  $g_S^0(q^2)$ , the proton electric form factor  $G_E^p(q^2)$  and the isovector pseudoscalar form factor  $g_P^3(q^2)$  in VQCD at  $\kappa = 0.162$  which corresponds to the quark mass of  $\sim 120$  MeV are plotted in terms of  $-q^2$ . They are normalized at  $q^2 = 0$  to 1 in order to compare their  $q^2$  dependence.

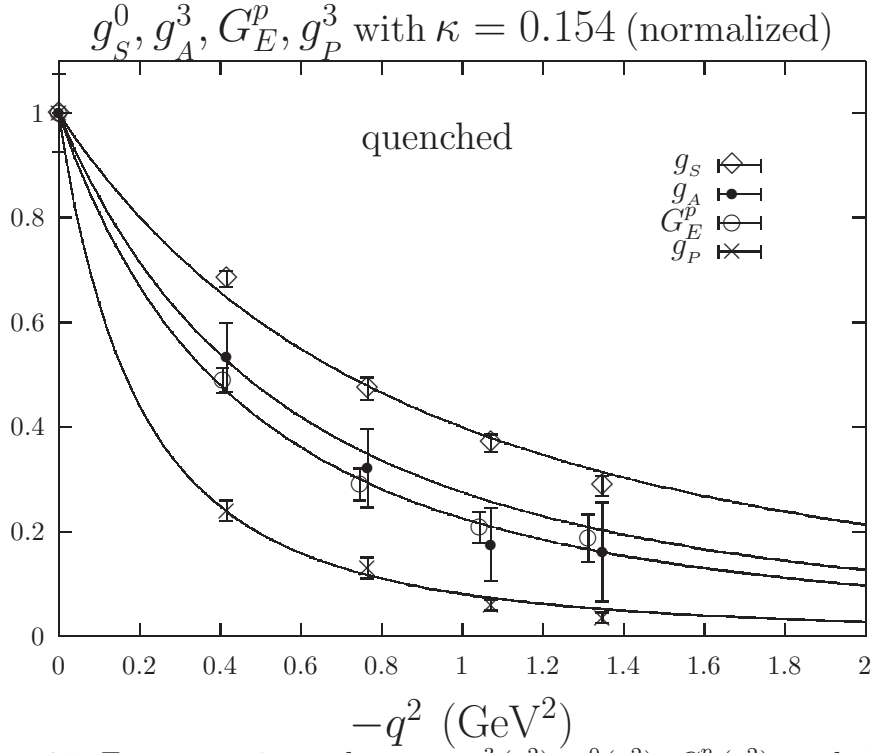


Figure 25: For comparison, the same  $g_A^3(q^2)$ ,  $g_S^0(q^2)$ ,  $G_E^p(q^2)$ , and  $g_P^3(q^2)$  in QCD at  $\kappa = 0.154$  which is at about the same quark mass, i.e.  $\sim 120$  MeV are plotted in terms of  $-q^2$ . They are also normalized to 1 at  $q^2 = 0$ .

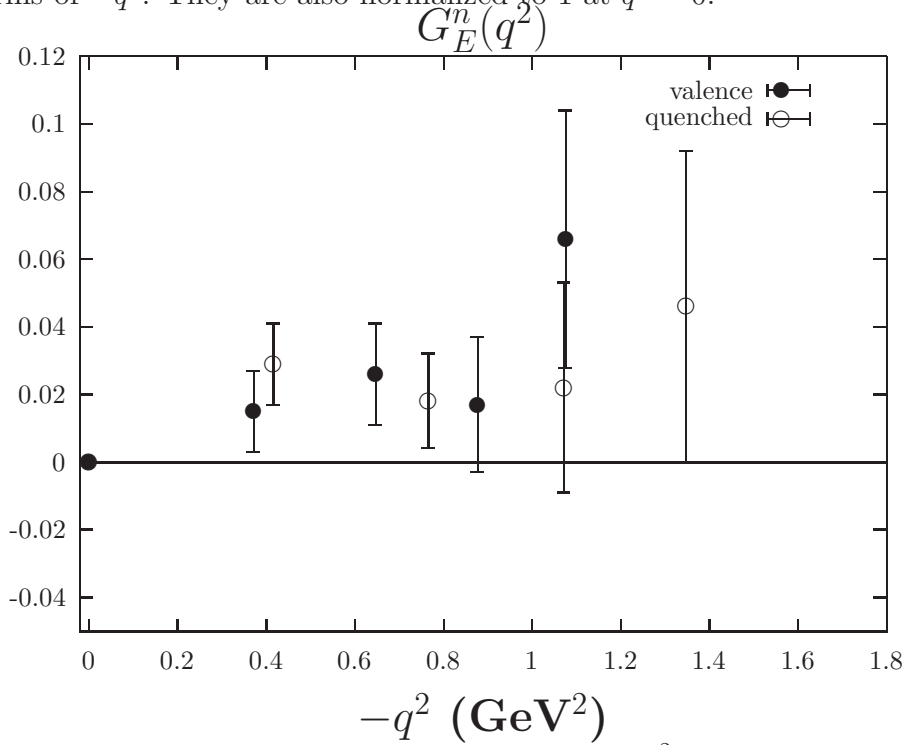


Figure 26: The neutron electric form factor  $G_E^n(q^2)$  for VQCD ( $\bullet$ ) at  $\kappa = 0.162$  is compared with the QCD result ( $\circ$ ) at  $\kappa = 0.154$ .



We also plot the neutron electric form factor  $G_E^n(q^2)$  for VQCD at  $\kappa = 0.162$  and its counter part (C. I. QCD at  $\kappa = 0.154$ ) in Fig. 26. We see that these two results are comparable in size and indicate that there are still some spin-spin correlation between the quarks in VQCD which breaks the  $SU(6)$  symmetry.

## 7.1 Goldberger-Treiman Relation and Vector Dominance

There are several interesting aspects to observe in VQCD. Since the axial Ward identities in Eqs. (42) and (43) are associated with the current involving both the  $u$  and  $v$  fields, they are applicable only to meson states with the creation and annihilation of quark-antiquark pairs. Thus, the identities are useful in addressing the relation of the ‘pion’ mass and decay constant with the quark mass as PCAC is in QCD. On the other hand, it does not apply to baryons where only the quarks are involved. For example, the pseudoscalar current matrix element between the nucleon states does not have the pion pole as evidenced in Fig. 24. Consequently, there is no Goldberger-Treiman relation in VQCD. Conversely, the conserved vector current in Eq. (36) between the baryons and meson states leads to separately conserved quark and antiquark numbers. This entails the three-point function calculation as illustrated in Fig. 5(a). Yet, it does not apply to situations involving quark-antiquark creations or annihilations. For example, the vector meson decay constant (in the continuum) is determined by the matrix element of the vector current between the vector meson state and the vacuum

$$\langle 0|V_\mu|v(k)\rangle = \frac{m_v^2 \epsilon_\mu e^{-ik \cdot x}}{f_v}, \quad (97)$$

where  $\epsilon_\mu$  is the polarization vector,  $m_v$  is the vector-meson mass, and  $f_v$  is the decay constant. Due to the vector current conservation  $\partial_\mu V_\mu = 0$ , the transversality condition  $k_\mu \cdot \epsilon_\mu = 0$  is derived in QCD. However in VQCD, the CVC relation in Eq. (36) does not apply to Eq. (97) because the conserved vector current in Eq. (37) does not have the pair annihilation term  $\bar{v}\gamma_\mu u$ . Similarly, there is no vector dominance in the pion and nucleon EM form factors. As discussed in the preceeding section, there should be no meson dominance in form factors in VQCD.

More generally, one can say that there is neither crossing relation, dispersion relation, nor unitarity in VQCD. But these features, or the lack of them, are shared by the valence quark model that we are trying to emulate.

## 7.2 Quark Condensate and Symmetry Breaking

The quark condensate  $\langle \bar{\Psi}\Psi \rangle$  in QCD is the order parameter of chiral symmetry breaking. In VQCD, there are two quark condensates  $\langle \bar{u}u \rangle$  and  $\langle \bar{v}v \rangle$ . Although VQCD eliminates the quark loops in the time direction, it still permits quark loops in the

spatial direction. One expects that

$$|\langle \bar{u}u \rangle| = |\langle \bar{v}v \rangle| < |\langle \bar{\Psi}\Psi \rangle| \quad (98)$$

due to the fact that  $\langle \bar{u}u \rangle$  and  $\langle \bar{v}v \rangle$  have null measure in the time direction. Unfortunately there is an subtraction in the lattice calculation of quark condensate due to a contact term for the Wilson action [78]. Short of a precise control of this subtraction, we are not able to have a fair comparison between  $\langle \bar{u}u \rangle$  and  $\langle \bar{\Psi}\Psi \rangle$ .

Nevertheless,  $\langle \bar{u}u \rangle$  and  $\langle \bar{v}v \rangle$  are nonzero which indicates that, to the extent that they serve as the order parameter of axial symmetry breaking as suggested by the existence of the Goldstone bosons and non-vanishing  $f_\pi$  in the last section, the symmetry breaking seems to be weaker than in QCD. It is shown in a Schwinger-Dyson equation study [79] recently that the pseudoscalar meson grows either linearly or as the square root of the quark mass depending on whether it is large or small compared to a scale set by the quark condensate  $\langle \bar{\Psi}\Psi \rangle$ . The linear dependence we see between the pion mass and the quark mass in Fig. 19 may mean that the quark masses we are calculating are still larger than the scale set by the quark condensate  $\langle \bar{u}u \rangle$  and  $\langle \bar{v}v \rangle$  and the quadratic pion mass dependence of the quark mass may yet to set in at smaller quark masses. Either way, the nonzero  $\langle \bar{u}u \rangle$  and  $\langle \bar{v}v \rangle$  supports the spontaneous axial symmetry breaking scenario with two Goldstone pions as alluded to in section 5.4.

## 8 Hadron Spectroscopy

To further explore the consequences of the valence approximation, we study the hadron masses. Since hadron masses entail calculations of two-point functions, the sea quarks do not appear explicitly as they do in three-point functions (see Fig. 5(b)). The only exception is the flavor-singlet meson where the D. I. (Fig. 4(b)) is part of the meson propagator. The implicit sea quark effects in the loops which manifest themselves through the fermion determinant are known to affect the scaling [76], the topological susceptibility, phase transition, the  $\eta'$  mass, and the slope of the hadron mass with respect to the quark mass [21, 80].

Here, we shall concentrate on the effects of the cloud quarks on hadron masses which are practically unknown. We first plot in Fig. 27 the masses of  $\Delta, N, \rho$ , and  $\pi$  as a function of the quark mass  $ma = \ln(4\kappa_c/\kappa - 3)$  on our lattice with quenched approximation. We see that the hyper-fine splittings between the  $\Delta$  and  $N$ , and the  $\rho$  and  $\pi$  grow when the quark mass approaches the chiral limit as expected.

In the infinite volume and continuum limits, it is found [77] that using  $m_\rho$  to set the scale, the  $K, \Phi$  mesons and the octet and decuplet baryon masses are all within about 6% of the experimental results.

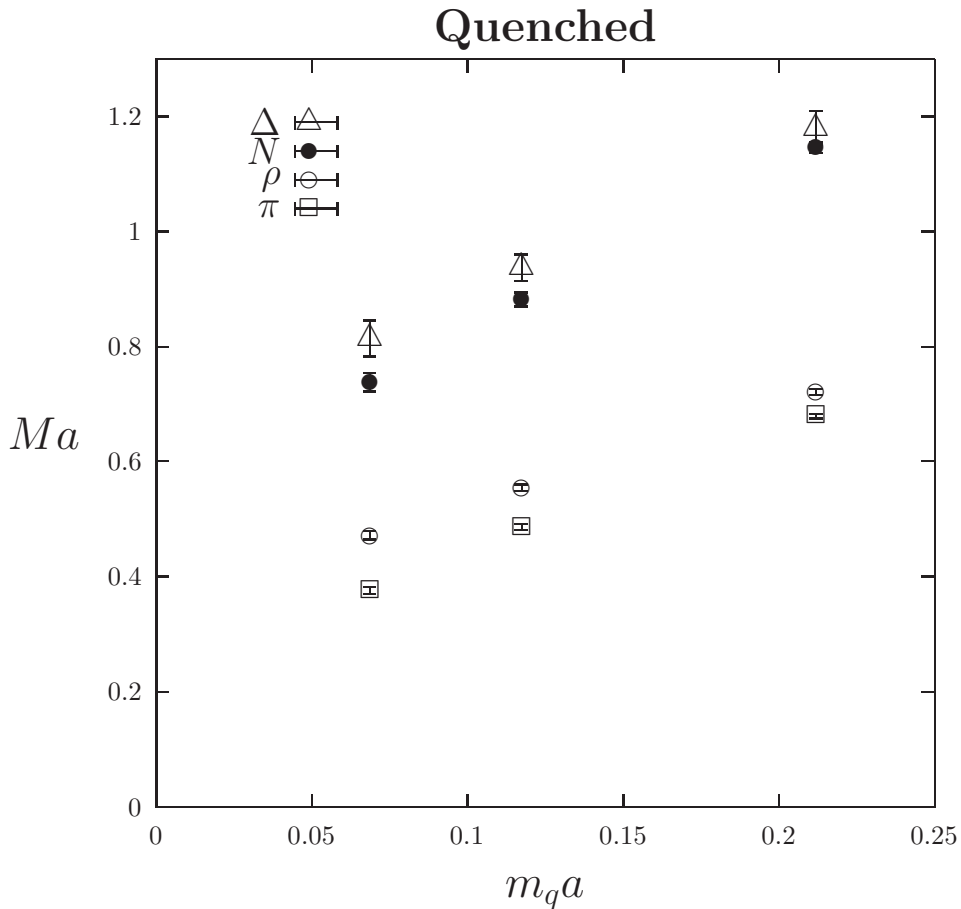


Figure 27: The dimensionless  $\Delta$ ,  $N$ ,  $\rho$ , and  $\pi$  masses in quenched QCD are plotted as a function of the quark mass  $m_q a = \ln(4\kappa_c/\kappa - 3)$ . The pion mass is proportional to  $\sqrt{m_q a}$ , while the others are extrapolated to the chiral limit with a linear  $m$  dependence.

Next we plot in Fig. 28 the masses of  $\Delta$ ,  $N$ ,  $\rho$ , and  $\pi$  as a function of the quark mass  $m_q a = \ln(4\kappa_c/\kappa - 3)$  ( $\kappa_c = 0.1649$  in this case) on the same quenched lattice. It is to our surprise that the truncation of the Z-graphs appears to have a dramatic effect on all these meson and baryon masses.

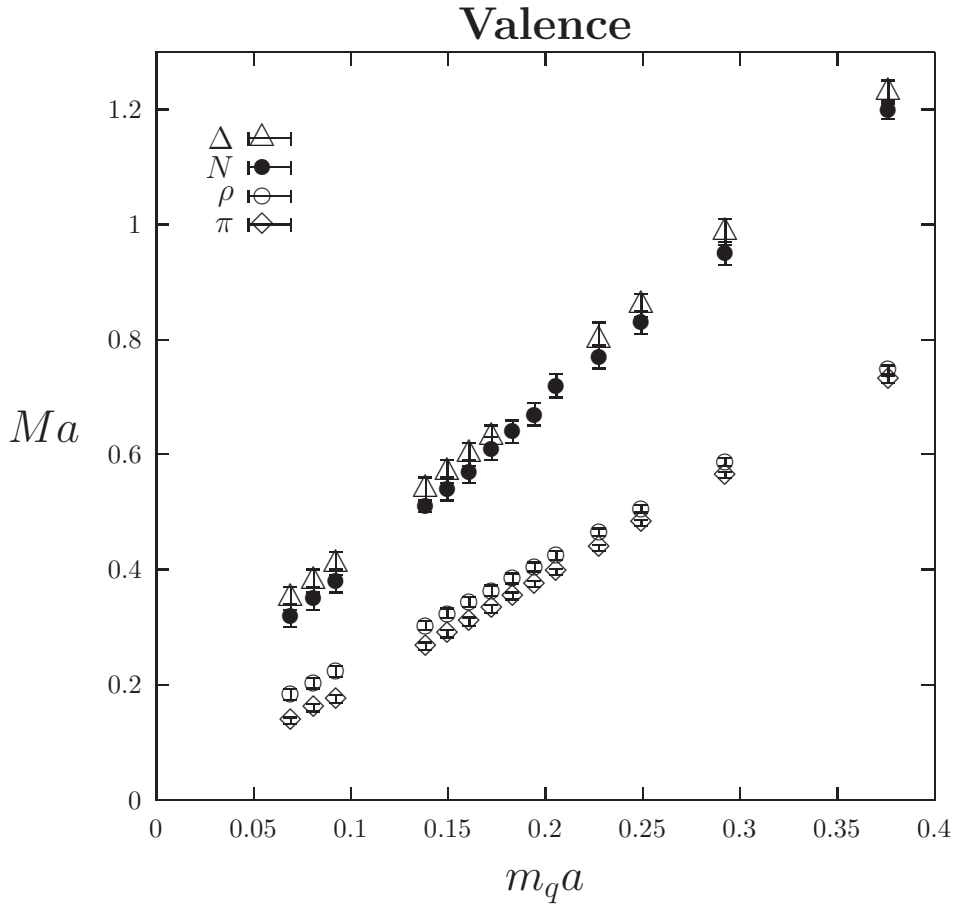


Figure 28: The dimensionless  $\Delta$ ,  $N$ ,  $\rho$ , and  $\pi$  masses in VQCD are plotted as a function of the quark mass  $m_q a = \ln(4\kappa_c/\kappa - 3)$ . All the masses are extrapolated to the zero quark mass limit with a linear  $m_q$  dependence.

First of all, we notice that the  $\Delta$  and the nucleon are on top of each other within errors all the way down to the smallest quark mass around the strange quark range. Thus, the hyper-fine splitting is largely gone in VQCD. This is true also between the  $\rho$  and  $\pi$ . Extrapolating to the zero quark mass limit, the  $\rho$  mass  $m_\rho a$  is 0.054(8). With  $a^{-1} = 1.75$  GeV,  $m_\rho = 95(14)$  MeV in VQCD. This is a factor of 6.4 smaller than that in the quenched approximation which gives  $m_\rho a = 0.343(6)$ . Secondly, we see that  $\Delta$ , N, and  $\rho$  all dropped their masses greatly compared to those in QCD (Fig. 27). The extrapolated  $m_\Delta a = 0.102(14)$ ,  $m_N a = 0.074(11)$  at the zero quark mass limit. They are much smaller than their corresponding values of 0.638(41) and 0.536(13) in the quenched QCD calculation in Fig 27. Furthermore, the hyper-fine splitting between  $\Delta$  and N is now 49(7) MeV which is  $\sim 3.7$  times smaller than our quenched result of 179(11) MeV <sup>†</sup>.

For a more direct comparison to see how the nucleon and  $\Delta$  masses drop, we plot the nucleon and  $\Delta$  masses in VQCD and quenched QCD on the same figure. We see in Fig. 29 that the nucleon moves down from VQCD to quenched QCD case by about a constant amount  $\sim 0.4$  which is about 700 MeV. Similarly, the  $\Delta$  mass drops by the same amount for heavier quarks. For quarks around the strange, it drops further to meet the nucleon. We also plot the  $\rho$  and  $\pi$  masses in VQCD and quenched QCD on Fig. 30. Analogous to the N -  $\Delta$  situation, the vector meson drops by about an equal amount  $\sim 0.31$  or 537 MeV; whereas, the pseudoscalar meson drops about 0.22 or 380 MeV in the strange region and approaches zero in both the quenched QCD and VQCD cases.

---

<sup>†</sup>Our quenched result is smaller than the experimental  $\Delta$ -N splitting of 298 MeV mainly due to the fact that our results are not in the infinite volume and continuum limits. It is shown that when these limits are taken, the octet and decuplet baryons are within 6% of the experimental values [77].

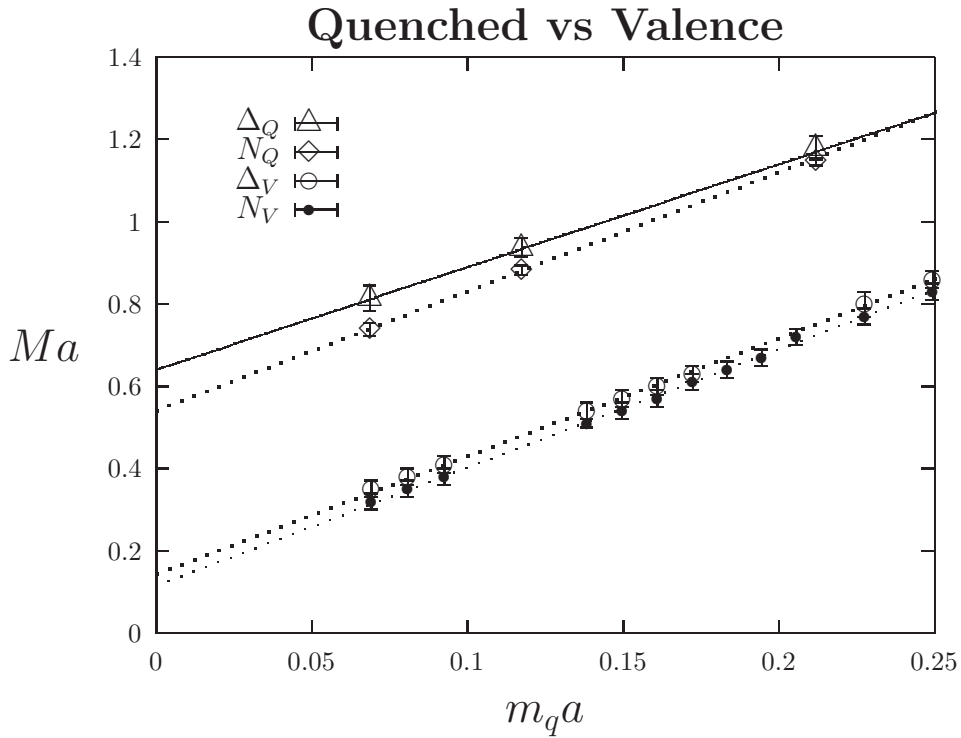


Figure 29: The dimensionless  $N$  and  $\Delta$  masses from QCD are compared with those in VQCD as a function of the quark mass.

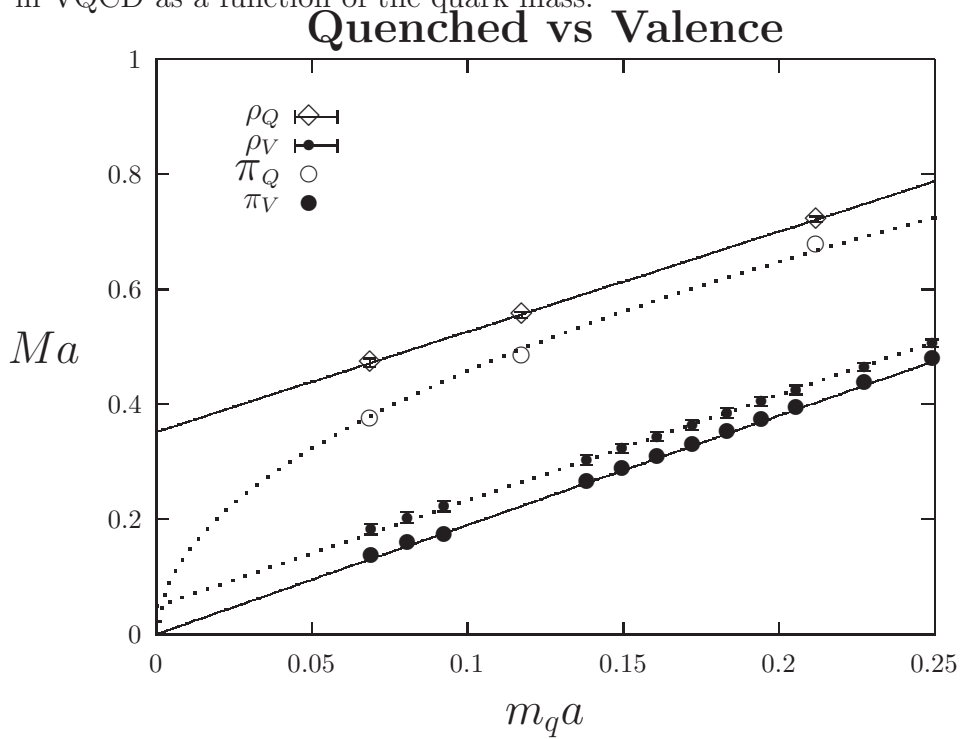


Figure 30: The dimensionless  $\pi$  and  $\rho$  masses from QCD are compared with those in VQCD as a function of the quark mass.

Shown in Fig. 31 are the  $a_1$  and  $a_0$  mesons calculated in quenched QCD and VQCD. We see that both mesons come down in mass from QCD to VQCD by a large amount.  $a_1$  appears to be degenerate with  $\pi$  and  $\rho$  in VQCD over the range of the quark mass in Fig. 31 and Fig. 28. However, we cannot be certain about this point, especially in view of the fact that the errors on  $a_1$  for the three lightest quarks are quite large.  $a_0$ , on the other hand, seems to be higher than the pion in this range of the quark mass.

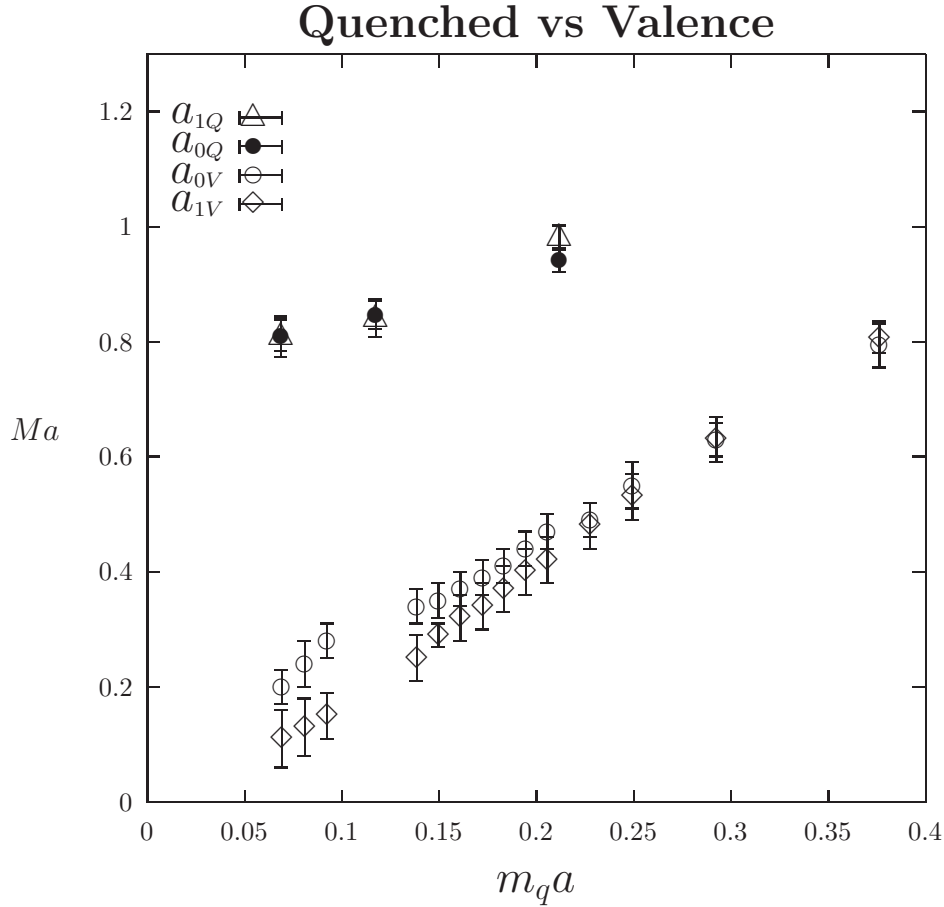


Figure 31: The dimensionless  $a_1$  and  $a_0$  masses from QCD are compared with those in VQCD as a function of the quark mass.

## 8.1 $\pi\rho$ correlation

There is a concern about the near degeneracy of  $N$  and  $\Delta$  and  $\rho$  and  $\pi$ . Since VQCD is not Lorentz invariant, is it possible that the interpolation field  $\bar{u}\gamma_i v$  intended for generating  $\rho$  may project onto a  $\pi$  state as well and causes the vector correlation function  $\langle \bar{v}\gamma_i^\dagger u(t)\bar{u}\gamma_i v(0) \rangle$  have the same asymptotic fall off as that of the pseudoscalar correlation function  $\langle \bar{v}\gamma_5^\dagger u(t)\bar{u}\gamma_5 v(0) \rangle$ ? To check this possibility, we calculate the cross correlation functions among the vector (V), pseudoscalar (P), axial (A), and scalar (S) interpolation fields. We see in Fig. 32 the cross correlation functions  $\langle V(t)P(0) \rangle$ ,  $\langle A(t)P(0) \rangle$ , and  $\langle S(t)P(0) \rangle$  have essentially zero overlap over the range of the Euclidean time  $t$ . Also shown in Fig. 33 are the cross correlation functions  $\langle A(t)V(0) \rangle$ ,  $\langle S(t)V(0) \rangle$ , and  $\langle P(t)V(0) \rangle$ . Again the overlaps are zero and the signals are cleaner.

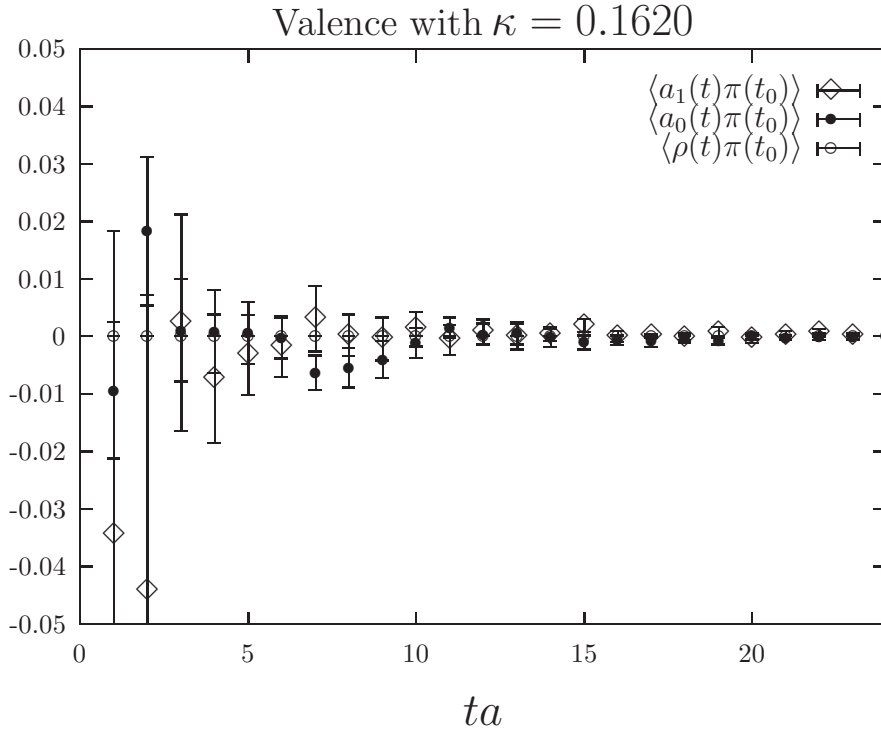


Figure 32: The cross correlation functions between the pseudoscalar (P) and the vector (V), the axial (A) and the scalar (S) channels are shown as a function of the time separation  $ta$ .

For comparison, we also plot the correlation function in the pseudoscalar and vector channels  $\langle P(t)P(0) \rangle$  and  $\langle V(t)V(0) \rangle$  for both the quenched and the VQCD cases in Fig. 34. We see that they are indeed much larger than the cross correlation functions in Figs. 32 and 33.



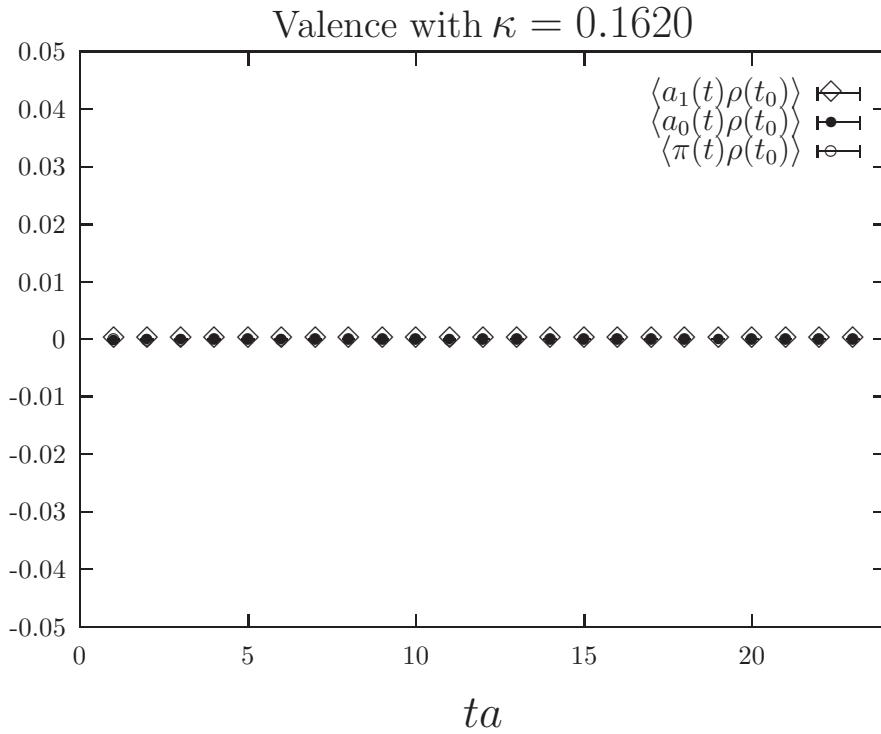


Figure 33: The cross correlation functions between the vector (V) and the axial (A), the scalar (S), and the pseudoscalar (P) channels are shown as a function of the time separation  $ta$ .

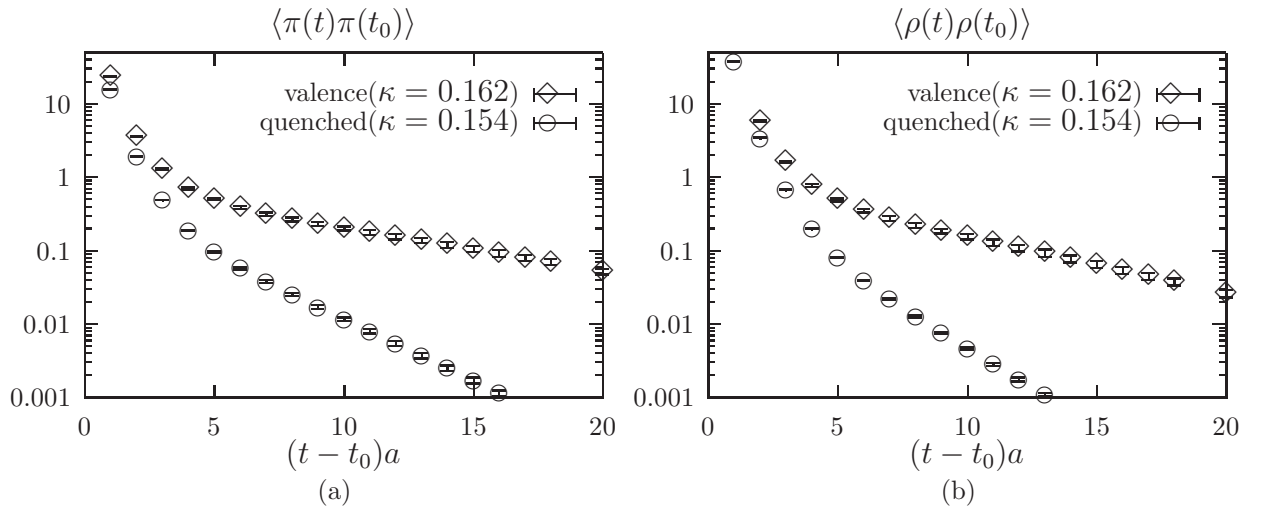


Figure 34: (a) The direct correlation functions  $\langle P(t)P(0) \rangle$  for both the quenched and VQCD as a function of the time separation  $ta$ . (b) The same as in (a) for  $\langle V(t)V(0) \rangle$ .

## 8.2 Origin of Hyper-fine Splitting

We see that the hyper-fine splitting between the  $\Delta$  and nucleon has largely disappeared in the light quark sector when we remove the cloud quark and antiquark in the form of the Z-graphs. This is rather mysterious in that according to the usual lore, the hyper-fine splitting is primarily due to the color-magnetic coupling induced spin-spin interaction between the quarks [6, 17]. This color-magnetic coupling is related to the spatial motion of the quarks which should not be affected by the truncation of the Z-graphs which only constraints the quark motion in the time direction. Indeed, this color-magnetic coupling is explicitly shown as  $\vec{\sigma} \cdot \vec{B}$  in the Pauli spinor representation of VQCD in Eqs. (29) and (31). Furthermore, it is this  $\vec{\sigma} \cdot \vec{B}$  term which is fully responsible for the hyperfine splitting between  $\Upsilon$  and  $\eta_b$  in the heavy quark system. The latter is proven by the lattice QCD calculation with the non-relativistic QCD action containing such a term in the form of  $\vec{\sigma} \cdot \vec{B}/2M_b$  [3, 4, 5].

This raises a question as to how effective the color spin interaction is as far as the hyper-fine splitting is concerned in the light hadron spectroscopy. The same question has been raised by Glozman and Riska [81, 82]. Upon studying the negative parity and positive parity excitations of the N,  $\Delta$  and  $\Lambda$  spectra, they found that the reverse ordering of the positive and negative parity resonances of N and particularly  $\Delta$  from those of the  $\Lambda$  cannot be accommodated with the color-spin structure of the pairwise interaction  $\lambda_i^c \cdot \lambda_j^c \vec{\sigma}_i \cdot \vec{\sigma}_j$ , rather it is consistent with the flavor-spin structure  $\lambda_i^F \cdot \lambda_j^F \vec{\sigma}_i \cdot \vec{\sigma}_j$ . This is so because flavor-spin structure of  $\Lambda$  is different from that of N and  $\Delta$ . Interpreting this as due to Goldstone boson exchange, they can fit the low-lying baryon spectrum with a confinement potential in addition and also the magnetic moments of the baryon octets by taking into account of the meson exchange currents [82, 83].

A similar problem was encountered in searching for scalar diquark clustering in lattice hadron form factors [84]. Significant scalar diquark clustering is predicted in quark models which rely on the hyperfine interaction of the OGEP to split the N and  $\Delta$ . While significant mass splitting is seen in the lattice simulations of Ref. [84, 85, 86] there is no evidence of scalar diquark clustering. This results leads one to look for other sources of hyperfine splitting that do not necessarily lead to clustering in the wave function, such as meson exchange [84].

Furthermore, it is well known from the light baryon spectrum that the spin-orbit interaction is much weaker [87, 88, 9, 10, 8] than that which accompanies the spin-spin interaction in the one-gluon-exchange picture [6]. This is problematic for the gluon-exchange picture if it is to explain both the heavy quarkonia which require the spin-orbit interaction and the light baryons which require a much weaker one. However, Goldstone boson exchange does not have the spin-orbit interaction between the light quarks and hence has no problem in this regard.

This Goldstone boson exchange picture appears to be quite consistent with what

we find in VQCD. The flavor-nonsinglet meson exchange between the quarks is represented by the Z-graph depicted in Fig. 32. Since all the Z-graphs are removed in VQCD, there will be no meson exchanges between the quarks as a result. This can explain why the hyper-fine splitting between  $\Delta$  and nucleon is greatly reduced in VQCD (Fig. 29). But this does not answer the question as to why the color-magnetic coupling induced spin-spin interaction is not as effective in light baryons as in heavy quarkonium. While we don't have a strong evidence for it, we note that one aspect of the light quark may contribute to the difference. Unlike the heavy quarks, the propagator of the light quarks in the background gauge field can fluctuate into color-singlet meson clouds leading to meson dominance in various form factors (see Fig. 11). The range of fluctuation depends on the Compton wavelength of the meson. The longest range is in the pseudoscalar channel with the pion cloud as evidenced in the softness of the pseudoscalar form factor of the nucleon (Figs. 10 and 15). By the same token, Goldstone boson exchange between the quarks in Fig. 35 can have a range commensurate with its Compton wavelength. On the other hand, the range of one gluon exchange is limited since the gluon is confined. If the range of Goldstone boson exchange is longer than the gluon confinement scale, the hyper-fine interaction from Goldstone boson exchange is likely to be more effective than that from the color-magnetic coupling. In other words, the light quarks in the baryon have larger separations than those between the quarks and antiquarks in heavy quarkonia and this could be the reason for the diminished color-magnetic coupling in light baryon due to the limited range of the confined gluons.

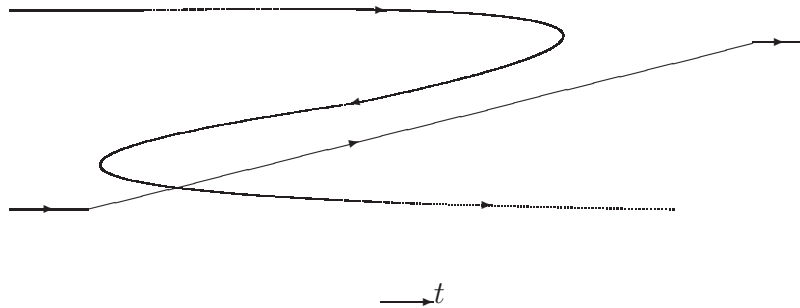


Figure 35: The meson exchange between quarks in the baryon is depicted as a Z-graph. The anti-quark produced in the Z-graph forms a meson with another quark in this case which is ‘exchanged’ between the two quarks.

### 8.3 Origin of Dynamical Quark Mass

Another significant feature of the VQCD spectroscopy in Figs. 28, 29, 30, and 31 is that all the hadron masses drop substantially from their counterparts in QCD (including pion at finite quark mass). For example, the nucleon moves down from 940 MeV in QCD (we used this to fix the scale) to 130(19) MeV in VQCD;  $\Delta$  drops from 1117(72) MeV to 179(25) MeV; and  $\rho$  drops from 600(11) MeV to 95 (14) MeV. It is well known that chiral symmetry breaking leads to a dynamical quark mass related to the quark condensate [89], in addition to the existence of Goldstone bosons. This can be seen from

$$\langle \bar{\Psi}\Psi \rangle = \langle \bar{\Psi}_L\Psi_R + \bar{\Psi}_R\Psi_L \rangle \quad (99)$$

which mixes the left- and right-handed quarks and has the effect of a dynamical mass as a result of the chiral symmetry breaking.

To the extent that we can interpret the VQCD result as due to the drop of dynamical or constituent quark mass, we can draw the following conclusions:

1. It is usually assumed in valence quark model that constituent quark mass arises from the dressing of the glue and the sea quark-antiquark pairs. Since the hard glue dressing in VQCD is expected to be the same as in QCD, it is not likely to be responsible for the dropping of hadron masses in VQCD. Furthermore, the quenched lattice calculations [77] can reproduce the  $\rho$ ,  $K$ ,  $\Phi$  mesons and the octet and decuplet baryon masses to within about 6% of the experimental results. This is an indication that the quark loops which generate sea quark-antiquark are not the primary source for hadron masses either. Here we see from our lattice calculation of VQCD that the dynamical quark mass actually arises from the ‘dressing’ of the cloud quarks — quark-antiquark pairs in the connected insertion.
2. Since we conclude that the hyper-fine splitting in the light baryons is largely due to the Goldstone boson exchanges, one would expect the dynamical mass generation of the chiral symmetry breaking to be prominently realized in the baryon spectroscopy also. In the chiral symmetry models, the dynamical mass is generally generated through the  $\sigma$  – the chiral partner of the pion. For example, in the linear sigma model, the dynamical mass is given [90, 91] as

$$m_{dyn} = \frac{g_{\sigma qq}^2}{-m_\sigma^2} \langle \bar{\Psi}\Psi \rangle_{m_\sigma} \quad (100)$$

where  $m_\sigma$  and  $g_{\sigma qq}$  and  $m_\sigma$  are the sigma mass and its coupling to the quark. This is represented as the sigma-quark tadpole diagram as illustrated in Fig. 33(a). Similar mechanism exists in the four-fermion Nambu-Jona-Lasinio model [92]. In QCD, the quark-line diagram which corresponds to the sigma-quark tadpole

in Fig. 36(a) would like something in Fig, 36(b) which inevitably involves cloud quarks and anti-quarks in the Z-graph.

- Interpreting the tadpole Z-graphs involving mesons in the scalar channel as the ones responsible for the dynamical quark mass generation, it is consistent with what we observe in VQCD. Dropping Z-graphs in VQCD which include these tadpoles diminishes the coupling to the quark condensate  $\langle \bar{\Psi}\Psi \rangle$  and leads to the downturn of all the hadron masses from QCD. However, there is still a class of tadpole diagrams which survive. These are the spatial moving quark loops restricted within time slices. They may still couple to  $\langle \bar{u}u \rangle$  and  $\langle \bar{v}v \rangle$ . But since these condensates in VQCD are much smaller than that in QCD (see Fig. 26), the dynamical mass is much smaller. This can explain why the masses of  $\Delta$ , N, and  $\rho$  are small but non-zero in VQCD (Figs. 28, 29, and 30).

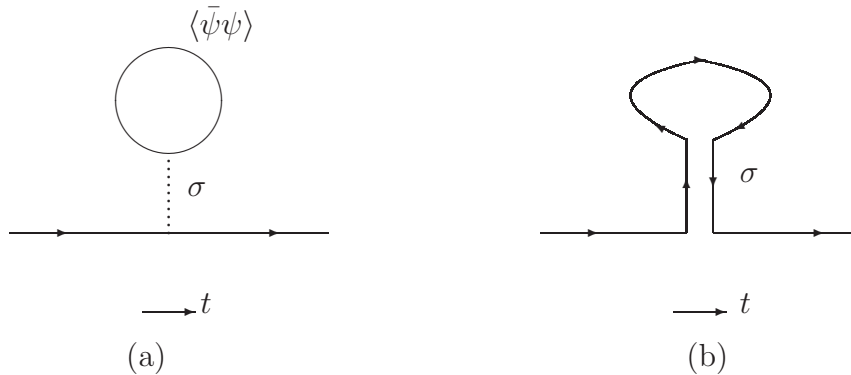


Figure 36: (a) Sigma-quark tadpole diagram in the linear sigma model which is the mechanism for dynamical mass generation in this model. (b) The quark line diagram of the Z-graph which corresponds to the sigma-quark tadpole in (a).

The interpretation we offer for the hyper-fine splitting and the dynamical quark mass is reminiscent of the chiral quark model of Manohar and Georgi [93] on which the phenomenological studies of baryon masses [81, 82, 83] and baryon structure [94] are based. Arguing that the chiral symmetry breaking scale  $\Lambda_{\chi SB}$  is higher than the confinement scale  $\Lambda_{QCD}$ , they propose the relevant dynamical degrees of freedom to be the fundamental quarks, gluons and the Goldstone bosons in an effective theory at intermediate scales between  $\Lambda_{\chi SB}$  and  $\Lambda_{QCD}$ . What we observe in VQCD seems to suggest that the scale for the structure of baryons falls just in this range so that

the coupling to Goldstone bosons and dynamical mass generation are evident when QCD and VQCD are compared.

There are other suggestions for the flavor-spin structure of the quark-quark interaction. These are induced by instantons [95, 96]. It is known that the instantons give rise to chiral symmetry breaking and generate dynamical quark mass associated with  $\langle \bar{\Psi}\Psi \rangle$  [97, 98]. The point-to-point hadronic correlation functions in the instanton liquid model [99] have been verified by lattice QCD calculation [100] and the role of instantons is revealed through cooling [101]. Although its direct connection to the cloud degree of freedom vis-a-vis VQCD is less transparent, the instanton picture, being the root of chiral symmetry breaking, is expected to reproduce the consequences of the chiral quark model.

## 9 Symmetry Breaking

It is well known that the chiral symmetry  $SU(N_F)_L \times SU(N_F)_R \times U_V(1)$  of QCD is spontaneously broken to the diagonal  $SU_V(N_F) \times U_V(1)$ . VQCD, as we have learned in this study, has a different symmetry breaking pattern. It starts out with the  $U(2N_F)$  symmetry (see Sec. 4.3) with vector and axial symmetries in the particle-antiparticle space. Given our lattice simulation, which shows that the pseudoscalar mesons corresponding to the interpolation fields  $\bar{u}\gamma_5 v$  and  $\bar{v}\gamma_5 u$  become massless at the zero quark mass limit, the pion decay constant  $f_\pi$  is non-zero (it may actually diverge as  $1/m_\pi$ ), and the condensate  $\langle \bar{u}u \rangle$  and  $\langle \bar{v}v \rangle$  do not vanish. We take this as the evidence for spontaneous breaking of the axial symmetry in Eqs. (42) and (43). This then leads to a  $U_q(N_F) \times U_{\bar{q}}(N_F)$  symmetry, which is the vector symmetry for the quarks and antiquarks separately. Again by virtue of the lattice simulation, we find that  $SU(6)$  relation holds quite well for the  $g_A^0/g_A^3$  (or  $F_A/D_A$ ),  $g_S^3/g_S^0$  (or  $D_S/F_S$ ), and  $\mu_n/\mu_p$  ratios. Furthermore, the nucleon and  $\Delta$ , and  $\rho$  and  $\pi$  are nearly degenerate. All these indicate that, although the  $SU(6)$  breaking color-magnetic coupling is present in the VQCD action (Eqs. (29), (30), and (31)), its effects are small. As a result, VQCD has an approximate higher symmetry, i.e.  $U_q(2N_F) \times U_{\bar{q}}(2N_F)$  where the 2 represents the spin subgroup  $SU(2)$ . This  $U_q(2N_F) \times U_{\bar{q}}(2N_F)$  is just the non-chiral  $U(6) \times U(6)$  symmetry of Dashen and Gell-Mann [102] for  $N_F = 3$  with quarks and antiquarks in the  $(\mathbf{6}, \mathbf{1})$  and  $(\mathbf{1}, \bar{\mathbf{6}})$  representation respectively. It was proposed as a ‘good’ symmetry for “stationary (i.e. bound) and quasi-stationary (i.e. resonant) states of hadrons at rest”. It is interesting to note that after stripping off the sea and cloud quarks, we find VQCD possesses the same symmetry as in the valence quark model with spin degeneracy.

## 10 Conclusion, Analogy to Shell Model and Many Body Theory

Instead of simulating QCD, we have mutilated it. The valence QCD theory we have constructed does not honor Lorentz invariance. It also violates unitarity, dispersion relation, and cross symmetry. But these are the attributes shared by the valence quark model which we set out to understand and our purpose of this study is to sort out the roles the various dynamical quark degrees of freedom play in different observables. This is much like the study of the brain <sup>‡</sup>. One tries to correlate the dysfunction of certain part of the body with the damage of a specific part of the brain to infer its controlling mechanism.

After defining the valence, the cloud, and the sea quarks from the hadronic tensor in deep inelastic scattering, we have been able to follow these degrees of freedom to three-point and two-point functions which are relevant to the quark model at low energies. Upon eliminating the cloud quarks in the connected insertion with the help of the VQCD action and the sea quarks in the disconnected insertion with the quenched VQCD calculation, we find from the ratios of  $g_A^0/g_A^3, g_S^3/g_S^0, \mu_n/\mu_p$  and the masses of N,  $\Delta, \rho$ , and  $\pi$  that there is an approximate  $SU(6)$  symmetry in VQCD which emerges from shaking off the “dressing” cloud and sea quark-antiquark pairs. Its symmetry breaking pattern is distinct from that of QCD. We summarize the symmetry breaking pattern of QCD and VQCD in the following chart:

$$\begin{aligned} \text{QCD} : & \quad \text{SU}(\mathbf{N}_F)_L \times \text{SU}(\mathbf{N}_F)_R \times \text{U}_V(\mathbf{1}) \Rightarrow \text{SU}_V(\mathbf{N}_F) \times \text{U}_V(\mathbf{1}) \\ \text{VQCD} : & \quad \text{U}(2\mathbf{N}_F) \Rightarrow \text{U}_q(\mathbf{N}_F) \times \text{U}_{\bar{q}}(\mathbf{N}_F) \Rightarrow \approx \text{U}_q(2\mathbf{N}_F) \times \text{U}_{\bar{q}}(2\mathbf{N}_F) \end{aligned}$$

We should point out that the  $U_q(2N_F) \times U_{\bar{q}}(2N_F)$  symmetry due to the spin degeneracy is only approximately true. We see that the ratio  $g_A^0/g_A^3$  in Fig. 21 is not exactly 3/5 and the neutron electric form factor  $G_E^n(q^2)$  in Fig. 26 is not exactly zero. The degeneracies between  $\Delta$  and N and between  $\rho$  and  $\pi$  are not perfect either. These indicate that there are still some color-magnetic coupling induced spin effects. Nevertheless, it is a fairly good approximate symmetry. What we have demonstrated in this study is that QCD has this approximate symmetry in its valence approximation à la VQCD action. To our best knowledge, this is the connection between QCD and the valence quark model.

The relation of the valence quark model and QCD actually is analogous to that between the shell model of nuclei and the many body theory. It is perhaps instructive to point out the parallel developments in the history of nuclear physics and hadron physics as far as the fermion dynamical degrees of freedom are concerned. We recall that the *raison d’être* of the shell model consists of the pattern of energy levels, the spin and parity quantum numbers of nuclei, and the Schmidt lines for the magnetic

---

<sup>‡</sup>We thank T. Cohen for this analogy.

moments of nuclei. Similar reasons, e.g. the mass pattern of baryons and mesons, SU(3) flavor symmetry, and the magnetic moments of proton and neutron lent their support for the existence of the quark model. Later experiments and theoretical developments in many body theory pointed out the inadequacies of the shell model and ideas like collectivity of the giant resonances [103], pairing through the induced phonon-exchange interaction [104], and core polarization for the magnetic moments or the Arima-Horie effect [105] are introduced. These involve the particle-hole degrees of freedom in the disconnected insertion which are the core polarization effects beyond the shell model. With the advent of QCD as the fundamental theory of quarks and gluons, similar ideas are introduced. For example, the resolution of the U(1) anomaly in terms of the topological susceptibility in the large  $N_c$  analysis by Witten and Veneziano [19] is the schematic model [103] approach to generating the  $\eta'$  mass by the collective coupling between quark loops. The concept of quark and gluon condensates are certainly related to pairing in the many body theory. Lack of appreciation for vacuum polarization due to the sea quarks for flavor-singlet observables in the quark model has led to the “proton spin crisis” [20, 42] and the  $\pi N\sigma$  term puzzle [47, 48, 21]. The importance of Z-graphs for density dependence was pointed out for the effective nucleon-nucleon interaction [106], and the higher density effects in the relativistic mean-field theory are shown largely to be due to the Z-graph with sigma meson exchanges [107]. The importance of the cloud quarks in hadrons through the Z-graphs are just beginning to be unraveled. The violation of the Gottfried sum rule leading to  $\bar{u}(x) \neq \bar{v}(x)$  is shown to be due to the cloud antiquarks [35]. Furthermore, we have learned in the present study that the hyper-fine splitting in baryons and the dynamical quark mass are related to the cloud degree of freedom, which are probably the most surprising results of VQCD.

The valence quark model, as we come to realize it today, is just like the shell model in nuclear physics. The  $U(6) \times U(6)$  symmetry which comes with the valence quark model as the defining characteristic is not as good a symmetry as one tends to believe. Even with the supplement of  $SU(6)$  breaking one-gluon exchange, it does not capture the richness of the cloud degree of freedom in various form factors and matrix elements in the connected insertions. Moreover, the lack of sea degrees of freedom in the disconnected insertions is responsible for its overestimate of the flavor-singlet  $g_A^0$  by a factor of  $\sim 3$  as well as its underestimate of the  $\pi N\sigma$  term by a factor  $\sim 3 - 4$ . What it lacks appears to be the spontaneous breaking chiral symmetry of QCD. This is exemplified in hadron spectroscopy where we find that the hyper-fine splitting between N and  $\Delta$  and the dynamical quark mass are related to the cloud quark in the Z-graphs.

One lesson we learned in this study is that the valence quark model is not necessarily a bad place to start building an effective theory of hadrons, provided one knows how to incorporate chiral symmetry and restores the cloud and sea degrees of freedom. Working in the intermediate scale between chiral symmetry breaking and



confinement which is appropriate for studying hadron structure and spectroscopy, one may start with the chiral quark model [93]. Integrating out the short-range part of the quark field is shown to lead to a very successful effective chiral theory of mesons [108]. One may extend this to the baryon sector with the quark coupling to the gluons and mesons [93]. In this way, the cloud degrees of freedom will show up in the form factors and matrix elements via meson dominance and meson exchange currents. It can also give rise to the hyper-fine splitting and the dynamical quark mass. The meson loops on the quark lines, on the other hand, are responsible for the sea degrees of freedom. We will study this in the future.

This work is partially supported by U.S. DOE grant No. DE-FG05-84ER40154. The authors would like to thank T. Barnes, C. Bernard, S. Brodsky, G. E. Brown, T. P. Cheng, T. Cohen, M. Golterman, L. Ya. Glozman, X. Ji, J.-F. Lagaë, C. S. Lam, B. A. Li, R. McKeown, J. Negele, M. Rho, D. O. Riska, C. Roberts, J. Rosner, E. Shuryak, A. Thomas, W. Weise, U.-J. Wiese, and A. Williams for very useful discussions.

## References

- [1] See for example, F. E. Close, An Introduction to Quarks and Partons, Academic Press, 1979.
- [2] J. Sloan, Nucl. Phys. B(Proc. Suppl.) **42**, 171 (1995).
- [3] J. Shigemitsu, Nucl. Phys. B (Proc. Suppl.) **53**, 16 (1997).
- [4] SESAM collaboration, N. Eicker et al., Nucl. Phys. B (Proc. Suppl.) **63**, 317 (1998).
- [5] NRQCD collaboration, C. T. H. Davies et al., Nucl. Phys. B (Proc. Suppl.) **63**, 320 (1998); hep-lat/9802024.
- [6] A. De Rújula, H. Georgi, and S. L. Glashow, Phys. Rev. **D12**, 147, 1975.
- [7] K. F. Liu, and C. W. Wong, Phys. Rev. **D17**, 2350 (1978); Phys. Rev. **D21**, 1350 (1980).
- [8] K. F. Liu and C. W. Wong, Phys. Rev. **D28**, 170 (1983).
- [9] N. Isgur and G. Karl, Phys. Rev. **D18**, 4187 (1978);
- [10] N. Isgur and G. Karl, Phys. Rev. **D19**, 2653 (1979).
- [11] L. Brekke and J. Rosner, Comments Nucl. Part. Phys. **A 18**, 83 (1988)

- [12] L. G. Pondrom, Phys. Rev. **D53**, 5322 (1996).
- [13] S. Ono, Nucl. Phys. **B107**, 522 (1976).
- [14] R. Koniuk and N. Isgur, Phys. Rev. **D21**, 1868 (1980).
- [15] J. F. Donoghue, E. Golowich, and B. R. Holstein, Dynamics of the Standard Model, Cambridge University Press, 1992.
- [16] S. Okubo, Phys. Lett. **5**, 165 (1963).
- [17] A. Chodos, R. L. Jaffe, K. Johnson, C. B. Thron, and V. F. Weisskopf, Phys. Rev. **D9**, 3471 (1974); A. Chodos, R. L. Jaffe, K. Johnson, and C. B. Thron, Phys. Rev. **D10**, 2599 (1974).
- [18] J. Donoghue and B. Holstein, Phys. Rev. **D29**, 489 (1984).
- [19] E. Witten, Nucl. Phys. **B149**, 285 (1979); G. Veneziano, Nucl. Phys. **B159**, 213 (1979).
- [20] S.J. Dong, J.-F. Lagaë, and K.F. Liu, Phys. Rev. Lett. **75**, 2096 (1995).
- [21] S.J. Dong, J.-F. Lagaë, and K.F. Liu, Phys. Rev. **D54**, 5496 (1996).
- [22] S. Weinberg, Phys. Rev. Lett. **17**, 616 (1966).
- [23] J. Gasser and H. Leutwyler, Nucl. Phys. **B250**, 465, 517, 539 (1985).
- [24] J. J. Sakurai, Phys. Rev. Lett. **17**, 1021 (1966); Currents and Meson, 1969 (The University of Chicago Press).
- [25] K. Kawarabayashi and M. Suzuki, Phys. Rev. Lett. **16**, 255 (1966); Fayyazuddin and Riazuddin, Phys. Rev. **147**, 1071 (1966).
- [26] Y. Tomozawa, Nuovo Cim. **46A**, 707 (1966).
- [27] G. Adkins, C. R. Nappi, and E. Witten, Nucl. Phys. **228**, 552 (1983).
- [28] M. Mattis, Chiral Solitons, ed. K. F. Liu (World Publishing Co., 1987), p. 171.
- [29] B. A. Li and K. F. Liu, Chiral Solitons, ed. K. F. Liu (World Publishing Co., 1987), p. 421.
- [30] M. Goldberger and S.B. Treiman, Phys. Rev. **110**, 1178 (1958).
- [31] G. 't Hooft, Nucl. Phys. **B72**, 461 (1974).
- [32] E. Witten, Nucl. Phys. **B160**, 57 (1979).

- [33] For a review, see for example Chiral Solitons, ed. K. F. Liu (World Publishing Co., 1987).
- [34] R. Dashen, E. Jenkins, and A. Manohar, Phys. Rev. **D49**, 4713 (1994).
- [35] K.F. Liu and S.J. Dong, Phys. Rev. Lett., **72**, 1790 (1994).
- [36] W. Wilcox, Nucl. Phys. (Proc. Suppl.), **B30**, 491 (1993).
- [37] K. F. Liu, under preparation.
- [38] J. Ashman et al. (EMC), Phys. Lett. **B206**, 364 (1988).
- [39] K. Abe et al. (E143), Phys. Rev. Lett. **74**, 346 (1995).
- [40] D. Adams et al. (SMC), Phys. Rev. **D 56**, 5330 (1997).
- [41] J. Kodaira, Nucl. Phys. **B165**, 129 (1980).
- [42] For a review, see H. Y. Cheng, Int. J. Mod. Phys. **A 11**, 5109 (1996).
- [43] M. Fukugita, Y. Kuramashi, M. Okawa, and A. Ukawa, Phys. Rev. Lett. **75**, 2092 (1995).
- [44] K.F. Liu, S.J. Dong, T. Draper, J.M. Wu, and W. Wilcox, Phys. Rev. **D 49**, 4755 (1994).
- [45] F.E. Close and R.G. Roberts, Phys. Lett. **B316**, 165 (1993).
- [46] T. P. Cheng and R. Dashen, Phys. Rev. Lett. **26**, 594 (1971).
- [47] T.P. Cheng, Phys. Rev. **D13**, 2161 (1976); *ibid* **D38**, 2869 (1988).
- [48] J. Gasser, H. Leutwyler, and M.E. Sanio, Phys. Lett. **B253**, 252, 260 (1991).
- [49] J. Gasser and H. Leutwyler, Phys. Rep. **87**, 77 (1982); J. F. Donoghue and C. R. Nappi, Phys. Lett. **B168**, 105 (1986).
- [50] M. Fukugita, Y. Kuramashi, M. Okawa, and A. Ukawa, Phys. Rev. **D51**, 5319 (1995).
- [51] L. Maiani et al., Nucl. Phys. **293**, 420 (1987).
- [52] M. Okawa, Nucl. Phys. B (Proc. Suppl.) **47**, 160 (1996).
- [53] J. Gasser, Ann. Phys. (NY) **136**, 62 (1981).
- [54] D.B. Leinweber, Phys. Rev. **D45**, 252 (1992).

- [55] D.B. Leinweber, Nucl. Phys. **A585**, 341 (1995).
- [56] D.B. Leinweber, Phys. Rev. **D53**, 5115 (1996).
- [57] S. J. Dong, K. F. Liu, and A. G. Williams, hep-ph/9712483, to appear in Phys. Rev. **D**.
- [58] B. Mueller *et al.*, SAMPLE Collaboration, Phys. Rev. Lett. **78**, 3824 (1997).
- [59] J. Gasser, M. E. Sainio, and A. Švarc, Nucl. Phys. **B 307**, 779 (1988).
- [60] W. Wilcox and R. M. Woloshyn, Phys. Rev. Lett. **54**, 2653 (1985); R. M. Woloshyn, Phys. Rev. **D34**, 605 (1986); W. Wilcox and K. F. Liu, Phys. Lett. **B172**, 62 (1986).
- [61] T. Draper, R. M. Woloshyn, W. Wilcox and K. F. Liu, Nucl. Phys. **B318**, 319 (1989).
- [62] W. Anderson and W. Wilcox, Annals of Phys. **255**, 34 (1997).
- [63] G. E. Brown, M. Rho, and W. Weise, Nucl. Phys. **A454**, 669 (1986).
- [64] M. Gari and U. Kaulfuss, Phys. Lett. **138B**, 29 (1984).
- [65] K. F. Liu, S. J. Dong, T. Draper, and W. Wilcox, Phys. Rev. Lett. **74**, 2172 (1995).
- [66] S. Collins, R.G. Edwards, U.M. Heller and J. Sloan, Nucl. Phys. **B (Proc. Suppl.) 47**, 378 (1996).
- [67] G. E. Brown, M. Rho, and W. Weise, Nucl. Phys. **A 454**, 669 (1986).
- [68] U. G. Meissner, N. Kaiser, and W. Weise, Nucl. Phys. **A 466**, 685 (1987).
- [69] E. Eichten and F. Feinberg, Phys. Rev. **D 23**, 2724 (1981).
- [70] S. Adler, Phys. Rev. **177**, 2426 (1969); J. Bell and R. Jackiw, Nuovo Cim. **60A**, 47 (1969).
- [71] We thank M. Golterman for pointing this out to us.
- [72] G. P. Lepage and P. B. Mackenzie, Phys. Rev. **D 48**, 2250 (1993).
- [73] K. Osterwalder and R. Schrader, Comm. Math. Phys. **31**, 83 (1973); *ibid* **42**, 281 (1975); K. Osterwalder and E. Seiler, Ann. Phys. **110**, 440 (1978).
- [74] I. Montvay and G. Münster, Quantum Fields on a Lattice, p. 182, Cambridge University Press (1994).

- [75] M. Gell-Mann, R. Oakes, and B. Renner, Phys. Rev. **175**, 2195 (1968).
- [76] J. Sexton and D. Weingarten, Phys. Rev. **D 55**, 4025 (1997).
- [77] F. Butler, H. Chen, J. Sexton, A. Vaccarino, and D. Weingarten, Phys. Rev. Lett. **70**, 2849 (1993); Nucl. Phys. **B430**, 179 (1994).
- [78] M. Bochicchio, L. Maiani, G. Martinelli, G. Rossi, and M. Testa, Nucl. Phys. **B262**, 331 (1985).
- [79] P. Maris and C. D. Roberts, nucl-th/9710062, Contribution to the IVth Int. Workshop on Progress in Heavy Quark Physics, Sept. 20-22, 1997, Rostock.
- [80] S. Collins, R. G. Edwards, U. M. Heller, and J. Sloan, Nucl. Phys. B (Proc. Suppl.) **47**, 378 (1996).
- [81] L. Ya. Glozman and D. O. Riska,  $\pi$  N Newslett. **10**, 115 (1995).
- [82] L. Ya. Glozman and D. O. Riska, Phys. Rep. **268**, 263 (1996).
- [83] L. Ya. Glozman, Z. Papp, and W. Plessas, Phys. Lett. **B381**, 311 (1996).
- [84] D.B. Leinweber, Phys. Rev. **D47**, 5096 (1993).
- [85] D.B. Leinweber, T. Draper, R.M. Woloshyn, Phys. Rev. **D46**, 3067 (1992).
- [86] D.B. Leinweber, R.M. Woloshyn, T. Draper, Phys. Rev. **D43**, 1659 (1991).
- [87] H. Dalitz, Prog. Part. Nucl. Phys., **8**, 7 (1982).
- [88] D. Gromes and I. O. Stamatescu, Nucl. Phys. **B112**, 213 (1976).
- [89] Y. Nambu and G. Jona-Lasinio, Phys. Rev. **122**, 345 (1961).
- [90] V. Elias and M. D. Scadron, Phys. Rev. Lett. **17**, 1129 (1984).
- [91] L. R. Baboukhadia, V. Elias, and M. D. Scadron, J. Phys. **G23**, 1065 (1997).
- [92] C. V. Christov et al., Prog. Part. Nucl. Phys. **37**, 1 (1996).
- [93] A. Manohar and H. Georgi, Nucl. Phys. **B234**, 189 (1984).
- [94] T. P. Cheng and L. F. Li, Phys.Rev.Lett. **80**, 2789 (1998); *ibid.* **74**, 2872 (1995).
- [95] E. V. Shuryak and J. L. Rosner, Phys. Lett. **218B**, 72 (1989).
- [96] G. 't Hooft, Phys. Rev. **D14**, 3432 (1976).
- [97] T. Schäfer and E. V. Shuryak, Rev. Mod. Phys. **70**, 323 (1998).

- [98] D. I. Dyakonov and V. Yu. Petrov, Phys. Lett. **147B**, 351 (1984).
- [99] E. V. Shuryak, Rev. Mod. Phys. **65**, 1 (1993).
- [100] M. C. Chu, J. M. Grandy, S. Huang, and J. W. Negele, Phys. Rev. Lett. **70**, 225 (1993); Phys. Rev. **D48**, 3340 (1993).
- [101] M. C. Chu, J. M. Grandy, S. Huang, and J. W. Negele, Phys. Rev. **D49**, 6039 (1994).
- [102] R. F. Dashen and M. Gell-Mann, Phys. Lett. **17**, 142 (1965).
- [103] G. E. Brown and M. Bolsterli, Phys. Rev. Lett. **3**, 472 (1959).
- [104] T.T.S. Kuo and G.E. Brown, Nucl. Phys. **85** (1966) 40.
- [105] A. Arima and H. Horie, Prog. Theor. Physics **11** (1954) 509.
- [106] G. Bertsch and T. T. S. Kuo, Nucl. Phys. **112**, 204 (1968).
- [107] G. E. Brown, W. Weise, G. Baym, and J. Speth, Comments Nucl. Pat. Phys. **17**, 39 (1987).
- [108] B. A. Li, Phys.Rev. **D52**, 5165, 5184 (1995).